Modification of graphene for applications in optoelectronic devices

Submitted by Gareth Francis Jones to the University of Exeter as a thesis for the degree of Doctor of Philosophy in Physics

September, 2017

I certify that all material in this thesis which is not my own work has been identified and that no material has previously been submitted and approved for the award of a degree by this or any other University.

Gareth Francis Jones

September, 2017

Abstract

In this thesis, we investigate how the optical and electronic properties of graphene may be modified in proximity to various other materials. We present several examples of how modification in this way can help make graphene better suited for specific device applications.

We develop a method of up-scaling the fabrication of $FeCl_3$-intercalated few-layer graphene from micron-sized flakes to macroscopic films so that it may be used as a transparent electrode in flexible light-emitting devices. We also find that photo-responsive junctions can be arbitrarily written into $FeCl_3$-intercalated few-layer graphene by means of optical lithography. These junctions produce photocurrent signals that are directly proportional to incident optical power over an extended range compared to other graphene photodetectors. Through theoretical analysis of these junctions, we conclude that the enhanced cooling of hot carriers with lattice phonons is responsible for this behaviour.

Finally, we trial rubrene single crystals as the light-absorbing layer in a graphene phototransistor. We find that rubrene single crystal-graphene interfaces exhibit enhanced charge transfer efficiencies under illumination with extremely weak light signals. Through a comparative study with similar devices, we conclude that the wide variation in sensitivity amongst graphene phototransistors is largely due to extraneous factors relating to device geometry and measurement conditions.

Acknowledgements

The work in this thesis would not have been possible without the assistance, support and friendship of many people along the way. Firstly, I would to thank my supervisors, Prof. Saverio Russo and Prof. Monica Craciun. I am grateful that you gave me the opportunity to pursue research topics with a considerable degree of independence, but that you were also always available when I required direction or support. I hope that the work of the group continues to go from strength to strength.

Thank you to all of my colleagues and friends in Russo/Craciun lab for providing such a friendly atmosphere in which to work. With respect to the work enclosed in this thesis, I must make a more detailed mention of a few people: Thank you to Elías Torres-Alonso, who worked on fabrication and measurement of the alternating current electroluminescent devices presented in Chapter 4. Thank you to Liping Lu for your work done fabricating and measuring the PLED devices in Chapter 4. Thank you Adolfo. De Sanctis for your work regarding device fabrication, photocurrent measurements and Raman spectroscopy measurements discussed in Chapter 5. Thank you to Rui Pinto for your assistance with the growth of rubrene single crystals which are used in Chapter 6. Thank you to Jake Mehew and Karthik Nagareddy for operating the microscopy system used in parts of Chapter 6. Thanks to Mark Heath for your hard work in keeping the cleanroom facilities running. Also a massive thanks to Paul Wilkins and the rest of the workshop crew for your help and expertise regarding designing and building much of the apparatus used in this thesis and for putting up with many mad requests for various contraptions.

A special thanks to a special group of people, who have made my prolonged experience in Exeter an unforgettable one: Matt Barnes, Dominique Wehenkel, Elías Torres-Alonso, Mukond Khetani, Adolfo de Sanctis, Lauren Barr, Jake Mehew and Freddie Withers.

A final and emphatic thank you to my friends and family away from Exeter for your support and patience whilst I have been stressing and striving over this thesis.

Contents

List of Figures

List of Publications

10. *Highly efficient rubrene-graphene charge transfer interfaces as phototransistors in the visible regime*, **G. F. Jones**, R. M. Pinto , A. de Sanctis, V. K. Nagareddy, C. D. Wright, H. Alves, M. F. Craciun and S. Russo, *Advanced Materials*, **29**, 1702993 (2017).

9. *Water-assisted synthesis of high-mobility and high-optical quality monolayer and bilayer WS_2*, F. Reale, P. Palczynski, I. Amit, **G. F. Jones**, J. D. Mehew, A. Bacon, N. Ni, P. C. Sherrell, S. Agnoli, M. F. Craciun, S. Russo and C. Mattevi, *Scientific Reports*, **7**, 14911 (2017).

8. *Extraordinary linear dynamic range in laser-defined functionalized graphene photodetectors*, A. de Sanctis, **G. F. Jones**, D. J. Wehenkel, F. Bezares, F. H. L. Koppens, M. F. Craciun and S. Russo, *Science Advances*, **3**, e1602617 (2017).

7. *Fast and Highly Sensitive Ionic Polymer Gated WS2-Graphene Photodetectors*, J. D. Mehew, S. Unal, E. Torres Alonso, **G. F. Jones**, S. F. Ramadhan, M. F. Craciun and S. Russo, *Advanced Materials*, **29**, 1700222 (2017).

6. *An integrated and multi-purpose microscope for the characterization of atomically thin optoelectronic devices*, A. de Sanctis, **G. F. Jones**, N. Townsend, M. F. Craciun and S. Russo, submitted to *Review of Scientific Instruments*, **88**, 055102 (2017).

5. *Homogeneously Bright, Flexible, and Foldable Lighting Devices with Functionalized Graphene Electrodes*, E. Torres Alonso, G. Karkera, **G. F. Jones**, M. F. Craciun, and S. Russo, *ACS Applied Materials & Interfaces*, **8**, 16541-16545 (2016).

4. *Critical Current Scaling in Long Diffusive Graphene-Based Josephson Junctions*, C. T. Ke, I. V. Borzenets, A. W. Draelo, F. Amet, Y. Bomze, **G. F. Jones**, M. F. Craciun, S. Russo, M. Yamamoto, S. Tarucha, and G. Finkelstein, *Nano Letters* **16**, 4788-4791 (2016).

3. *High Efficiency CVD Graphene-lead (Pb) Cooper Pair Splitter*, I. V. Borznets, Y. Shimazaki, **G. F. Jones**, M. F. Craciun, S. Russo, Y. Yamamoto and S. Tarucha *Scientific Reports* **6**, 23051 (2016).

2. *Large-area functionalized CVD graphene for work function matched transparent electrodes*, T. H. Bointon, **G. F. Jones**, A. de Sanctis, R. Hill-Pearce, M. F. Craciun and S. Russo, *Scientific Reports* **5**, 16464 (2015).

1. *Functional modulation and directed assembly of an enzyme through designed non-natural post-translation modification*, A. M. Hartley, A. Zaki, A. R. McGarrity, C. Roberts-Ansart, A. V. Moskalenko, **G. F. Jones**, M. F. Craciun, S. Russo, M. Elliott, E. Macdonald and D. D. Jones, *Chemical Science* **6**, 3712-3717 (2015).

Glossary

List of Symbols

Greek symbols

α	:	power exponent of photocurrent
α_{xx}	:	polarisability
α_λ	:	fraction of an absorbed photon's energy transferred to hot electrons
β	:	bolometric coefficient
γ	:	responsivity
γ_0	:	nearest neighbour hopping integral
γ_h	:	scattering rate of hot electrons
Δf	:	noise bandwidth
ΔT	:	temperature difference between hot electrons and lattice ions
$\Delta\omega$	:	Raman shift (change in wavenumber of a scattered photon)
Δn	:	change in charge carrier concentration
ε_0	:	permittivity of free space
ε_r	:	relative permittivity of a dielectric
ξ	:	hot electron cooling length
η_{CT}	:	quantum efficiency of charge transfer across a material interface
η_{diss}	:	quantum efficiency of exciton dissociation into free charge carriers
η_{EQE}	:	external quantum efficiency
η^*_{EQE}	:	specific external quantum efficiency
η_{gen}	:	quantum efficiency of generating photo-excited electron-hole pairs under illumination
η_{iPG}	:	internal photo-gating quantum efficiency
η_{IQE}	:	internal quantum efficiency
η_L	:	luminance efficiency
η_{PG}	:	photo-gating quantum efficiency
κ	:	thermal conductivity
Λ	:	empirical energy broadening of the density of states
λ	:	photon wavelength
λ_{ex}	:	wavelength of a monochromatic excitation light source

μ	:	charge carrier mobility
v	:	photon frequency
ρ_m	:	mass density
σ	:	conductivity
σ_{min}	:	minimum conductivity
τ_L	:	photo-excited charge carrier lifetime
τ_{tr}	:	charge carrier transit time
ϕ_c	:	chemical potential/quasi-Fermi level

Latin symbols

A	:	device active area/constant of proportionality
A'	:	constant of proportionality
A''	:	constant of proportionality
A_λ	:	absorbance
$A(G)$	:	area of the Raman peak labelled G
a	:	inter-atomic displacement in graphene
$\mathbf{a}$	:	primitive lattice vector
$\mathbf{b}$	:	reciprocal lattice vector
C_{el}	:	specific heat capacity of hot electrons
c	:	speed of light in vacuum
D	:	screened deformation potential/detectivity
D^*	:	specific detectivity
$D(E)$	:	density of states
d	:	film thickness
d_{SiO_2}	:	thickness of an SiO_2 dielectric
E_F	:	Fermi energy
e	:	absolute charge of an electron/proton
$FWHM(G)$	:	full width half maximum of the Raman peak labelled G
f_{BW}	:	operational bandwidth
G	:	photoconductive gain
g	:	electron-phonon coupling frequency
H_{SC}	:	power transferred to lattice ions through supercollisions of hot electrons per unit area

H_{AP}	:	power transferred to lattice ions through single phonon scattering events between hot electrons and acoustic phonons per unit area
I_{diff}	:	photocurrent due to anisotropic thermal diffusion of charge carriers
I_{drift}	:	photocurrent due to the drift of charge carriers in the presence of an electrochemical potential gradient
l	:	mean free path of charge carriers
h	:	Planck constant
I_{DS}	:	source-drain current
I_n	:	electrical noise current
I_{ph}	:	photocurrent
I_{PV}	:	photocurrent produced by the photovoltaic effect
I_{PTE}	:	photocurrent produced by the photo-thermoelectric effect
$I(G)$	:	intensity of the Raman peak labelled G
$\mathbf{J}_{ph}$	:	photocurrent density
k	:	wavevector
k_F	:	wavevector of an electron occupying a state at the Fermi level
k_B	:	Boltzmann constant
L	:	length
LDR	:	linear dynamic range
l_0	:	laser spot diameter
NA	:	numerical aperture
NEP	:	noise equivalent power
N_{ph}	:	absorbed photon flux
n	:	charge carrier concentration/dimensionless power exponent
n_{ph}	:	photo-excited charge carrier density
P	:	optical power density
P_{sat}	:	optical power density at photocurrent saturation
$Pos(G)$	:	position of the Raman peak labelled G
$\langle Pos(G) \rangle$	:	area-weighted average position of all degenerate Raman peaks labelled G
q	:	phonon wavevector
q_D	:	wavevector of the highest energy lattice phonon
R	:	resistance
R_B	:	ballast resistance

R_C : contact resistance

R_{sq} : sheet resistance

R_{2P} : two probe resistance

R_{4P} : four probe resistance

$R(\lambda)$: reflectance

S : Seebeck coefficient

S_n : noise spectral density

T : temperature

T_{BG} : Bloch-Grüneisen temperature

T_D : Debye temperature

T_G : graphene-zone furnace temperature

T_h : hot electron temperature

T_i : intercalant-zone furnace temperature

T_L : lattice ion temperature

Tr : transmittance

V : voltage

V_{AC} : peak applied voltage of a sinusoidal signal

V_{CNP} : applied gate voltage at charge neutrality

V_{ch} : potential difference across a transistor channel

V_G : gate voltage

V_{osc} : output root mean square oscillator voltage of a lock-in amplifier

V_{ph} : photovoltage

v_F : Fermi velocity

v_S : speed of sound in a medium

W : width

Latin-like symbols

$\mathcal{E}$: electric field

$\hbar$: reduced Planck constant

$\mathcal{P}$: polarisation

List of Abbreviations

ACEL	:	alternating current electroluminescent
AFM	:	atomic force microscope
C8-BTBT	:	2,7-Dioctyl[1]benzothieno[3,2-b][1]benzothiophene
CVD	:	chemical vapour deposition
CW	:	continuous wave (i.e. constant illumination)
EQE	:	external quantum efficiency
F8BT	:	poly(9,9-dioctylfluorene-alt-benzothiadiazole)
FET	:	field effect transistor
$FeCl_3$-FLG	:	few layer graphene intercalated with $FeCl_3$
FRET	:	Förster resonance energy transfer
HOMO	:	highest occupied molecular orbital
ITO	:	indium tin oxide
LUMO	:	lowest unoccupied molecular orbital
P3HT	:	Poly(3-hexylthiophene-2,5-diyl)
PET	:	polyethylene terephthalate
PGQE	:	photo-gating quantum efficiency
PL	:	photoluminescence
PLED	:	polymer-based light-emitting diode
PMMA	:	poly(methyl methacryalate)
PTE	:	photo-thermoelectric
PV	:	photovoltaic
Stage - 1/2/3	:	one/two/three layers of graphene between two intercalant layers

Author's Declaration

The research presented in this thesis relates to several of the manuscripts included in the preceding list of publications, for which there are multiple co-authors in each study. The content enclosed in this thesis focuses on my individual contribution towards a number of these collaborative research projects and has not previously been submitted and/or approved for the award of a degree by this or any other university. Footnotes are provided to acknowledge any contributions made by colleagues towards the data presented in each chapter. Anything excluded from these footnotes represents my personal contribution.

Gareth. F. Jones, September 2017.

1

Introduction

1.1 Optoelectronic devices

Optoelectronic devices are systems which convert between optical and electrical signals. In the form of photodetectors and emissive displays, they act as communication ports which link the natural and digital world. In the form of solar photovoltaic cells, they are increasingly helping to meet our demands for sustainable sources of energy. The importance of optoelectronic devices is demonstrated by their increasing prevalence in our day-to-day lives. Approximately two billion adults world-wide now own smart phones with emissive displays,[1] whilst the emerging industries of smart textiles and the 'internet of things' are requiring light sensors to be embedded in a vast array of items ranging from household appliances to medical diagnostic patches. This ever-increasing range of applications places additional requirements on the properties of constituent materials within optoelectronic devices. Commonly-used inorganic semiconductors such as silicon and gallium phosphide are too bulky and brittle to be utilised in flexible and lightweight electronics. Instead, new materials are required which are able to function in extreme environments.

1.2 Graphene

Graphene is a single atomic sheet of graphite. Although its electronic structure was theoretically described as early as 1947,[2] it was thought to be structurally unstable until its isolation in the laboratory in 2004.[3] This subsequently lead to the awarding of a Nobel prize in 2010. Since then, there has been an exponential growth in research activity concerning this material, with at least 13,000 graphene-related scientific papers published in 2016 alone.[4] Graphene has been found to exhibit a remarkable collection of physical properties in terms of mechanical strength, efficient electronic transport and broadband interaction with light. As a result, there is now much interest in utilising graphene as a constituent material in novel optoelectronic devices which exceed the capabilities of those

based purely on silicon, $III-V$ semiconductors and doped metal oxides.

One promising application of graphene is as a transparent electrode. Efficient transmittance ($Tr \sim 97.7\%$[5]) of white light,[5] high charge carrier mobility,[6] superior flexibility,[7,8] an appropriate work function[9] and the potential for comparatively low embedded energy costs[10] make graphene well-suited as a candidate material to replace indium tin oxide (ITO) electrodes in organic light-emitting diodes (LEDs) and organic solar cells. Substantial progress has already been made to this end: graphene electrodes have now been successfully incorporated into prototypes of both LEDs[11] and solar cells,[12] whilst the demonstration of compatible roll-to-roll printing processes[13] has addressed questions regarding the practical feasibility of mass-producing large-scale, atomically-thin electrodes.

The primary remaining challenge relating to graphene-based transparent electrodes is the high sheet resistance (R_{sq}) of monolayer graphene ($R_{sq} \sim (1-10)\, k\Omega/sq$, in un-doped samples) in comparison to ITO ($R_{sq} \sim (5-100)\, \Omega/sq$ and $Tr \sim (75-85)\,\%$ depending upon film thickness[14,15]). Because of an increase in series resistance, charge transport is impeded in optoelectronic device heterostructures where monolayer graphene replaces ITO electrodes and the efficiency of operation is often impaired.[16] Successive stacking of monolayer graphene to form few-layer (< 10 layer) films reduces the sheet resistance approximately to that of ITO but also produces an unsatisfactory degradation in optical transmittance.[17] To overcome this, strategies have been developed to lower the sheet resistance of each constituent atomic sheet within few-layer graphene through chemical doping, thereby reducing the total number of light-absorbing layers required in a suitably conductive film. The most prevalent method of doping involves exposing each graphene monolayer to aqueous HNO_3 before the next graphene sheet is stacked on top.[13] Typical sheet resistance/transmittance values in the range of $30\Omega sq^{-1}$/ 90% can be achieved, but this process is highly cumbersome and is associated with low throughput yields. Simpler single-step methods which expose a complete few-layer graphene film to dopant molecules will only alter the charge carrier concentration of the exposed surface layer and reductions in sheet resistance are less pronounced. Intercalation of graphene with acceptor or donor molecules can increase the charge carrier concentration throughout a few-layer graphene film to unprecedented levels ($\leq 10^{14} cm^{-2}$ per layer[18]) by means of a single-step process and is therefore a very appealing method of chemically doping electrodes. Li-intercalated few-layer graphene was found to produce ideal sheet resistance and transparency metrics ($R_{sq} \approx 3\Omega sq^{-1}$, $Tr \approx 92\%$[19]), but is highly unstable in ambient conditions. Similarly optimal sheet resistance and transmittance has been reported for $FeCl_3$-intercalated few-layer graphene ($FeCl_3$-FLG) ($R_{sq} \approx 9\Omega sq^{-1}$, $Tr \approx 84\%$[18]) but, crucially, this material remains stable in conditions of extreme humidity, high temperature and even when exposed

to organic solvents of $FeCl_3$.[20] As a result, $FeCl_3$-FLG currently presents one of the most viable graphene-based compounds for use as a transparent electrode in optoelectronic devices. Several challenges must now be addressed in order to further assess the viability of these electrodes: up-scaled fabrication methods for producing continuous, macroscopic films of $FeCl_3$ need to be developed; fast, non-invasive methods of characterising the quality of large-area $FeCl_3$ are required; and $FeCl_3$-FLG electrodes should be incorporated into proof-of-concept optoelectronic devices.

Another popular field of research is the use of lateral junctions in graphene, defined by local gradients in charge carrier concentration, for the electrical detection of incident light. This application might initially sound counter-intuitive, since we have just described graphene as a nearly transparent material. However, the absorbance of graphene is, in fact, remarkably strong for a single atomic layer and its linear, gapless low-energy bandstructure produces uniform optical absorbance over a wide spectral range.[5] Because of these factors, graphene is commonly utilised as a light-absorbing layer in novel ultra-thin photodetectors.[21] A critical parameter of photodetectors, especially in radiometric applications, is the linear dynamic range (LDR). This defines the range of optical power across which the magnitude of photocurrent is directly proportional to the intensity of incident light. Photodetectors with a large LDR are therefore well-suited to measure the optical power of variable light sources accurately. Extensive studies of illuminated lateral junctions in graphene have revealed that photocurrent signals arise from a combination of 'photothermoelectric' and 'photovoltaic' effects.[22,23] The magnitude and power dependence of each effect varies considerably with respect to the charge carrier concentration, temperature and the degree of disorder in each sample.[22–25] As a result, photodetectors reported thus far that are formed from electrostatically-gated[23,26] and chemically doped[27,28] junctions in graphene have shown unpredictable variations in power dependence and a small LDR ($\leq 15dB$) at room temperature. If graphene-based photodetectors are to be used in radiometric applications, methods of engineering stable photo-responsive junctions in graphene that consistently display a large LDR are required.

An alternative use of graphene in light-sensing applications comes in amplified phototransistors. In these devices, graphene is paired with a semiconductor layer, such as colloidal PbS quantum dots, to form charge transfer interfaces.[29] An internal photoconductive gain mechanism within these phototransistors enables far weaker incident light signals, equivalent to that of diffuse daylight and even moonlight, to be resolved than is possible with lateral graphene junctions. Because of their excellent sensitivity, graphene-based phototransistors are now being considered for use as pixels in next-generation imaging arrays.[30] Organic semiconductors would be an ideal class of light-absorbing materials

to use in graphene-based phototransistors because they offer an extremely wide range of absorption spectra and can be solution processed at low cost. However, reports so far have shown graphene-organic semiconductor phototransistors[31–34] to exhibit inferior responsivity and quantum efficiencies in comparison to graphene phototransistors that use inorganic semiconductors as the light-absorbing layer.[29,35–44] Research efforts are now required to investigate the fundamental limitations of organic semiconductors as light-absorbing layers in graphene phototransistors. Also, a consensus needs to be established in this field as to how the performance metrics of graphene-based phototransistors should be reported. This would eliminate many ambiguities which are currently encountered when comparing different studies and would enable researchers to assess the merits of each variant of phototransistor accurately.

This thesis addresses all of the challenges outlined in this section. The common strategy which unites all of these research initiatives is the aim to understand how interactions between graphene and light may be tailored through partnership with complimentary materials, such as $FeCl_3$ and organic semiconductors, in order to suit the intended functions of various optoelectronic devices. In doing so, the work in this thesis aims to further our of graphene's utility in several of the most popular classes of optoelectronic device and provides one of the many steps required to bring this novel material out of the laboratory and into real-world applications.

1.3 This thesis

In Chapter 2 we will introduce background concepts which are essential to our experimental findings. We will review the electronic and optical properties of monolayer graphene before paying particular attention to the variety of photocurrent generation mechanisms in this material. Some essential working principles of photodetectors and polymer light-emitting diodes will be introduced and, finally, we will review the electrical properties of rubrene single crystals.

In Chapter 3, we will outline the most important experimental methods which have been used in our work. These include the synthesis of large-area graphene and single crystals of rubrene. We will then introduce the concept of intercalation of few-layer graphene. Finally, we will review the technique of Raman spectroscopy and its use as a non-invasive tool for characterising graphene's structural and electronic properties.

In Chapter 4 we present the first of three experimental investigations. Here we develop a method of producing large-area electrodes of $FeCl_3$-intercalated few layer graphene and implement them into proof-of-concept light-emitting devices. Through careful examination

of the impact of graphene grain density on intercalation staging and sheet resistance, we gain valuable information as to how these macroscopic transparent conductive films may be further engineered so that they may emulate the optimum properties displayed in microscopic intercalated flakes. This presents the first reported up-scaling of this material and the first case of its incorporation into practical optoelectronic devices.

In Chapter 5 we demonstrate that $FeCl_3$-intercalated few-layer graphene is not only a good transparent electrode, but that its local charge carrier density can be modified via optical lithography to engineer photo-responsive junctions. We study the photocurrent signals generated at these junctions and find a linear dynamic range of $44dB$. This extends at least two orders of magnitude beyond the range of conventional graphene photodetectors. By adapting existing theory concerning drift and diffusion-assisted mechanisms of photocurrent in graphene, we conclude that the cooling of hot charge carriers is accelerated by the high levels of p-doping induced upon intercalation with $FeCl_3$. This marks the first reported method of reliably tuning the electron-phonon interactions in graphene to produce a consistently linear proportionality between photocurrent and incident optical power.

In Chapter 6 we address the final experimental study of this thesis, where we incorporate rubrene single crystals as the light-absorbing layer in a graphene phototransistor. Through carefully characterising this device's amplified electrical response to light, we conclude that organic semiconductors can indeed be employed as effective light-absorbing layers in graphene phototransistors. We also undertake a comparative study of all reported graphene phototransistors to draw conclusions as to how the relative performance of these devices might be better assessed. This serves as the first reported incorporation of a single crystal organic semiconductor into an amplified graphene photodetector.

2

Theoretical Concepts

2.1 Electronic properties of graphene

2.1.1 Lattice structure and energy bands

Graphene consists of a planar sheet of carbon atoms arranged in a hexagonal structure that is reminiscent of honeycomb or chicken wire. The $2s$, $2p_x$ and $2p_y$ orbitals of each carbon atom hybridise to form three strong σ-bonds with neighbouring atoms in the xy plane. The remaining $2p_z$ orbital of each atom projects out perpendicularly from the lattice plane. Strong overlap between neighbouring p_z orbitals creates π^* and π-bands of delocalised electrons above and below the lattice respectively. It is these π and π^* bands which govern the charge transport properties of graphene.[45]

The lattice structure of monolayer graphene is shown in Figure 2.1a. It is comprised of two inter-weaved triangular sub-lattices which together form a hexagonal structure. The unit cell contains one atom from each sub-lattice, denoted A and B respectively. The lattice vectors can be expressed in terms of the length of the σ-bond between carbon atoms ($a = 1.42\mathring{A}$).

$$\mathbf{a}_1 = \frac{a}{2}\left(3, \sqrt{3}\right) \tag{2.1}$$

$$\mathbf{a}_2 = \frac{a}{2}\left(3, -\sqrt{3}\right) \tag{2.2}$$

The first Brillouin zone also has a hexagonal structure, as illustrated in Figure 2.1b, with reciprocal lattice vectors denoted $\mathbf{b}_1$ and $\mathbf{b}_2$.

$$\mathbf{b}_1 = \frac{2\pi}{3a}\left(1, \sqrt{3}\right) \tag{2.3}$$

$$\mathbf{b}_2 = \frac{2\pi}{3a}\left(1, -\sqrt{3}\right) \tag{2.4}$$

The first Brillouin zone encloses several high symmetry points which are labelled in Figure 2.1b. Of particular interest are the K/K' points with wavevectors $\mathbf{K} = \left(\frac{2\pi}{3a}, \frac{2\pi}{3\sqrt{3}a}\right)$

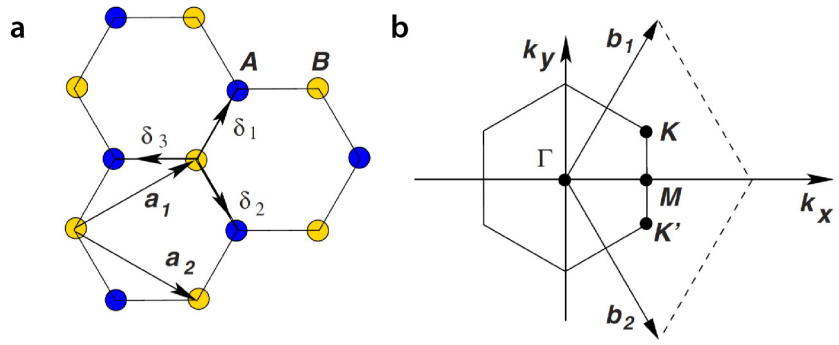

Figure 2.1: The lattice structure of monolayer graphene. a) The A (blue) and B (yellow) sublattices of monolayer graphene. Nearest neighbour distances (δ_1,δ_2,δ_3) and lattice vectors ($\mathbf{a}_1$, $\mathbf{a}_2$) are labelled. **b)** The first Brillouin zone of the reciprocal lattice, enclosed by lattice vectors $\mathbf{b}_1$ and $\mathbf{b}_2$, contain high symmetry points K, K', Γ and M. Reproduced with permission.[45]

and $\mathbf{K}' = \left(\frac{2\pi}{3a}, -\frac{2\pi}{3\sqrt{3}a}\right)$ respectively. A satisfactory calculation of the energy band structure of graphene can be achieved by solving the Schrödinger using the tight binding Hamiltonian and limiting considerations of interactions between atomic orbitals to just the three nearest neighbours of each atom (vectors δ_1, δ_2 and δ_3).[2] The resultant energy dispersion of this calculation is

$$E\left(k_x, k_y\right) = \pm\gamma_0\sqrt{1 + 4\cos\left(\frac{3ak_x}{2}\right)\cos\left(\frac{\sqrt{3}ak_y}{2}\right) + 4\cos^2\left(\frac{\sqrt{3}ak_y}{2}\right)} \tag{2.5}$$

where $\gamma_0 \approx 2.8eV$ is the hopping integral between nearest neighbour atomic orbitals.[45] Equation (2.5) is plotted in Figure 2.2 with k_x and k_y extending just beyond the first Brillouin zone. From this, we can see that valence ($E < 0$, π) and conduction ($E > 0$, π^*) bands are formed, which intersect at the K and K' points of the reciprocal lattice for $E = 0$. The two free p_z electrons per unit cell completely fill the π-band and leave the π^*-band unoccupied. As a result, the Fermi energy, E_F, of intrinsic graphene is located at these points of intersection. Graphene is therefore a zero-gap semiconductor, otherwise known as a 'semi-metal'.

Because $E_F = 0$ in pristine samples, the transport properties of graphene at experimentally attainable levels of doping ($-1eV \leq E_F \leq 1eV$) can be described by evaluating Equation (2.5) for small changes in wavevector, κ, about the K and K' points. The resulting low-energy dispersion relation is expressed in Equation (2.6) and shown graphically in Figure 2.5b.

$$\varepsilon_\kappa = \pm\left(\frac{3\gamma_0 a}{2}\right)|\kappa| = \pm\hbar v_F\,|\kappa| \tag{2.6}$$

Where $v_F \approx 10^6 ms^{-1}$ is the Fermi velocity.[46] Within this low-energy regime, the energy dispersion describes conical conduction and valence bands where the size of the

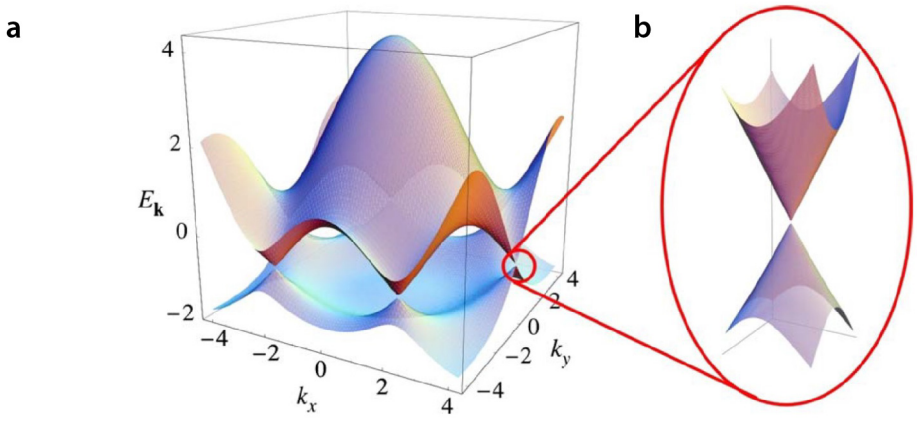

Figure 2.2: The bandstructure of monolayer graphene. a). The energy dispersion of monolayer graphene (Equation (2.5), calculated using the tight binding model) throughout the first Brillouin zone. The π^* conduction band and π valence band touch at the K and K' points of the reciprocal lattice. **b)** Magnified image of the linear band structure at the K and K' points for low energies. Reproduced with permission.[45]

Fermi surface varies linearly with energy. The density of states, $D(E)$, in this range is

$$D(E) = \frac{2}{\pi} \cdot \frac{|E|}{\hbar^2 v_F^2}. \tag{2.7}$$

2.1.2 Graphene transistors

In a field effect transistor (FET) structure, the electronic properties of graphene can be experimentally probed. A schematic of a graphene FET is provided in Figure 2.3a, it consists of a film of monolayer graphene laminated to a highly p-doped silicon substrate with a thermally-grown surface oxide of SiO_2 which acts as a dielectric. SiO_2 layers are approximately $d_{SiO_2} \approx 280nm$ thick in most devices. In this configuration, the dielectric is thick enough to not breakdown under small applied voltages and thin-film interference effects enhance the optical contrast of monolayer graphene on the substrate such that it can be readily identified under examination with an optical microscope.[47] Metal electrodes are thermally evaporated onto select regions of the graphene film so that it can be electrically contacted. This is achieved by use of a shadow mask or optical/electron beam lithography procedures. If the measurement circuit sketched in Figure 2.3a is established and a positive gate voltage (V_G) is applied to the silicon substrate, a compensating negative charge density (Δn) will accumulate in graphene according to the capacitance per unit area of the SiO_2 dielectric.

$$\Delta n = \frac{\epsilon_0 \epsilon_r \left(\Delta V_G\right)}{|q|\, d_{SiO_2}} \approx 7.2 \times 10^{10} \Delta V_G \quad \left[cm^{-2}\right] \tag{2.8}$$

Here, ϵ_0 is the permittivity of free space and $\epsilon_r \approx 3.9$ is the relative permittivity of the SiO_2 dielectric. From Equation (2.8), we find that for a practical gate voltage range of $-80V < V_G < 80V$, charge carrier densities as large as $n = 6 \times 10^{12} cm^{-2}$ can be induced in graphene. Assuming that graphene is initially intrinsic at $V_G = 0V$ ($\Delta n = n$), we can equate the applied gate voltage to a change in Fermi level by integrating Equation (2.7) with respect to energy and substituting into Equation (2.8).

$$E_F = \hbar v_F \sqrt{\pi n} \tag{2.9}$$

$$E_F \approx 3.0 \times 10^{-2} \sqrt{\Delta V_G} \quad [eV] \tag{2.10}$$

For the aforementioned range of gate voltages, the Fermi level of graphene can be modulated such that $-270meV < E_F < 270meV$. Hence, the Fermi level of graphene can be swept across a significant portion of the linear band regime via electrostatic gating. Figure 2.3b shows a plot of conductivity as a function of gate voltage for a graphene FET measured at low temperature ($T = 10K$) in order to suppress electrical noise. Because of the absence of an energy band gap, a continuous transition between p-type ($V_G < 0$, $E_F < 0$) and n-type ($V_G > 0$, $E_F > 0$) doping is observed. If the graphene sample is already extrinsically doped, a gate voltage V_{CNP} will be required to reach charge neutrality. This 'charge neutrality voltage' can be used as a reference potential to calculate the absolute charge carrier concentration in graphene using Equation (2.8). For sufficiently high charge carrier densities, graphene can be considered a two-dimensional electron gas and a classical model of conductivity is valid.

$$\sigma = ne\mu \tag{2.11}$$

The charge carrier mobility, μ, can therefore be experimentally measured via the electric field effect described in Equation 2.8. At low charge carrier densities ($n < 1 \times 10^{11} cm^{-2}$), a quantum mechanical interpretation of electrons in graphene must be considered which uses the Dirac equation. In this case, a minimum conductivity of $\sigma_{min} \sim 4e^2/h$ arises from inter-band 'zitterbewegung' transitions of charge carriers.[48] This value of σ_{min} corresponds to the conductance quantum, e^2/h, multiplied by the two-fold spin degeneracy and two-fold valley degeneracy (K, K') of charge carriers in the first Brillouin zone. In practice, all but the smallest, cleanest graphene devices will deviate from this minimum conductance due to lattice disorder and inhomogeneous doping across large samples. Because of this, σ_{min} is often evaluated empirically from gated

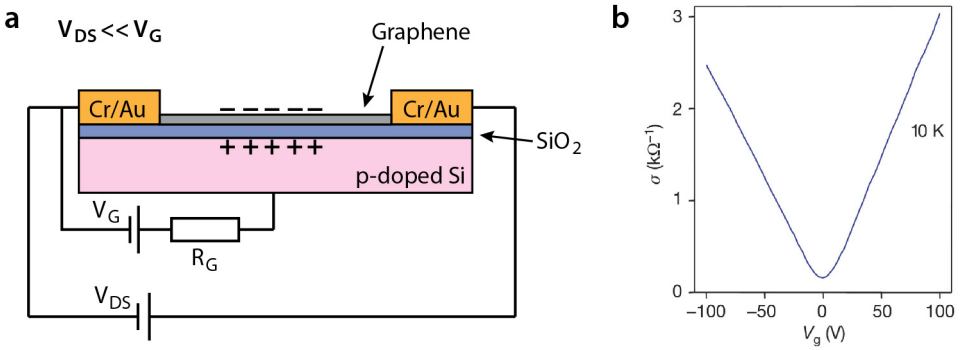

Figure 2.3: Electric field effect in graphene transistors a). Schematic of a graphene field effect transistor (FET) and an associated measurement circuit, where a gate votlage V_G is applied to the Si/SiO_2 substrate and a comparatively small voltage, V_{DS}, is applied between source and drain electrodes. **b)** Conductance as a function of gate voltage in a graphene FET measured at $T = 10K$. b) is reproduced with permission.[46]

measurements akin to Figure 2.3b. Equations (2.9) and (2.11) can be combined to form a phenomenological description of the conductivity of monolayer graphene.

$$\sigma(E) = \frac{e\mu E^2}{\pi\hbar^2 v_F^2} + \sigma_{min} \tag{2.12}$$

Equation (2.12) may also be written in the form

$$\sigma(E) = \sigma_{min}\left(1 + \frac{E^2}{\Lambda^2}\right) \tag{2.13}$$

where $\Lambda = \sqrt{hv_F^2 e/4\pi\mu}$, assuming $\sigma_{min} = 4e^2/h$. Alternatively, Λ can be assessed empirically from in a gate sweep measurements of a graphene FET. Disorder and inhomogeneous doping creates a Gaussian distribution of E_F across the channel and σ_{min} will span a wider range of V_g. Lastly, the electrical conductivity and thermal conductivity, κ, can be related to one another using the Wiedemann Franz Law[49] when the energy-dependent term dominates Equation (2.12).

$$\frac{\kappa}{\sigma} = \frac{3}{2}\left(\frac{k_B}{e}\right)^2 T \tag{2.14}$$

2.1.3 Phonons in graphene

Lattice vibrations within a crystal will distort the local band structure, resulting in electron-phonon coupling. These processes are relevant for understanding the origin of hot carriers in graphene, so we will review some essential concepts here. For the simplest case of scattering in a conductor, an electron of energy E_k and wavevector $\mathbf{k}$ emits or

absorbs a single phonon and then occupies a final energy state $E_{k'}$ with wavevector $\mathbf{k'}$. Conservation of energy and momentum dictate that Equations (2.15) and (2.16) must be satisfied.[49]

$$\hbar\omega\left(\mathbf{q}\right) = \pm\left(E_{k'} - E_k\right) \tag{2.15}$$

$$\mathbf{q} = \mathbf{k'} - \mathbf{k} \tag{2.16}$$

Here, $\hbar\omega\left(\mathbf{q}\right)$ and $\mathbf{q}$ are the energy and wavevector of the phonon respectively. The highest-energy phonon mode in a crystal is still considerably lower than that of conduction electrons ($\hbar\omega\left(\mathbf{q}_D\right) << E_F$). As a result, we may visualise the maximum allowed transfer of energy between a scattered electron and the crystal lattice by extrapolating between two allowed states on the Fermi surface with a phonon wavevector of magnitude $|\mathbf{q}_{max}|$.[49,50] Examples of these electron-phonon scattering events are shown in Figures 2.4a-c for the case of a typical metal. The Debye temperature, T_D, sets the temperature above which all phonon modes in the crystal can scatter with electrons (see Figure 2.4a). If the temperature falls below T_D (see Figures 2.4b and 2.4c), thermal energy is no longer sufficient to excite the highest frequency phonon modes and they are 'frozen out' of scattering processes. The maximum possible energy transfer between an electron and the lattice is then successively reduced with temperature, this is known as the Bloch-Grüneisen regime.[51] An elegant feature of graphene is that the same effect can be achieved by simply tuning the Fermi level at room temperature. Figures 2.4d-e illustrate the phase space restrictions imposed on electron-phonon scattering events as the p-doping in a sheet of graphene is gradually reduced. This can be achieved by electrostatic gating[51] or, as Chapter 5 will show, by chemical modification. Stiff C-C bonds in the graphene lattice produce extremely high energy optical phonon modes with a Debye temperature of $T_D \sim 2800K$. The Bloch-Grüneisen temperature, $T_{BG} < T_D$, effectively acts as a 'variable Debye temperature' and imposes the limit $|\mathbf{q}_{max}| < 2k_F$ on electron-phonon scattering.

$$T_{BG} = 2\hbar v_s k_F / k_B \tag{2.17}$$

In Equation (2.17), $v_s \sim 2 \times 10^4 ms^{-1}$ is the speed of sound (i.e. acoustic phonons).[52] An important implication of this effect is that heat transfer from excited electrons and holes to the lattice is very inefficient in graphene at low levels of charge carrier concentration. We will return to this concept in Section 2.4.2.

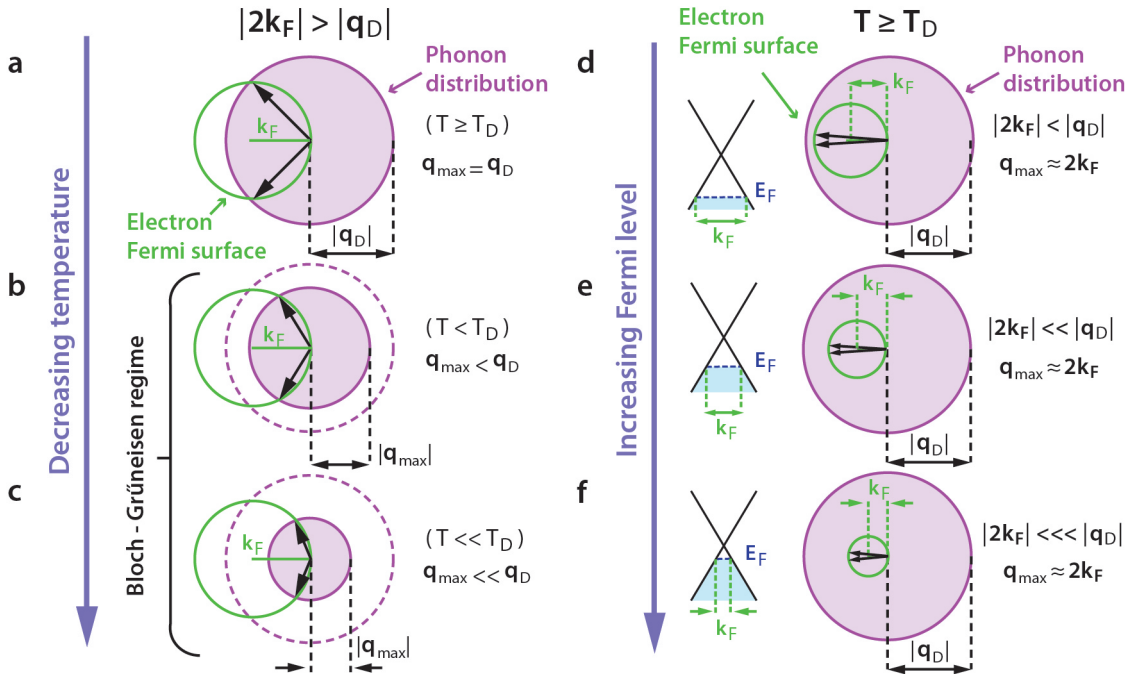

Figure 2.4: Freezing out phonons at room temperature. Illustrations in reciprocal space of the Fermi surface (green circle) and phonon modes (purple circle) **Left:** A 2D conductor with a Fermi surface comparable to the Brillouin zone ($|2\mathbf{k}_F| > |\mathbf{q}_D|$). **a)** At temperatures greater than the Debye temperature, T_D, all phonon modes are active and $\rho \propto T$.[49] **b)** At $k_BT < k_BT_D$, we enter the Bloch-Grüneisen regime, where $\rho \propto T^4$.[51] High energy phonons are frozen out and $q_{max} = k_BT/\hbar v_s$. **c)** At even lower temperature, many more phonons are frozen out and electron scattering angles become shallow. **Right:** Monolayer graphene, where the Fermi surface is smaller than the wavevector of optical phonons. $T_{BG} = 2\hbar v_s k_F/k_B < T_D$ now sets the threshold temperature of the Bloch-Grüneisen regime. **d-f** By tuning the Fermi level in graphene progressively closer towards the charge neutrality point at constant temperature, T_{BG} is reduced and more phonon modes are frozen out from charge scattering processes.

2.2 Optical properties of graphene

2.2.1 Light absorption

The absorption of light can occur via direct ($\Delta k = 0$) and indirect ($\Delta k \neq 0$, i.e. phonon-assisted) excitation of an electron by an incident photon of appropriate energy. The band structure of graphene, detailed in Figure 2.2, enables direct excitation of electrons between the π and π^* bands for photon energies up to approximately $3.96eV$.[53] The transmittance spectrum of monolayer graphene is shown in Figure 2.5.[5] Transmittance remains remarkably consistent, even for transitions outside of the linear band regime, with the inset plot showing each graphene sheet in a few-layer stack to absorb approximately 2.3% of white light.

In the case of doped graphene, the Pauli exclusion principle prevents excitation of electrons from the valence band to the conduction band by incident photons of energy $hv < 2\,|E_F|$. The same restrictions are imposed in p-doped graphene due to the absence of available ground state electrons. Illustrations of these forbidden transitions are shown in Figures 2.5b and 2.5c. A result of this effect is that graphene has a gate-tunable transmittance spectrum. However, the limitations of standard electrostatic gating methods (see Equation (2.10)) mean this effect only becomes practically relevant at mid-infrared wavelengths in graphene FETs.

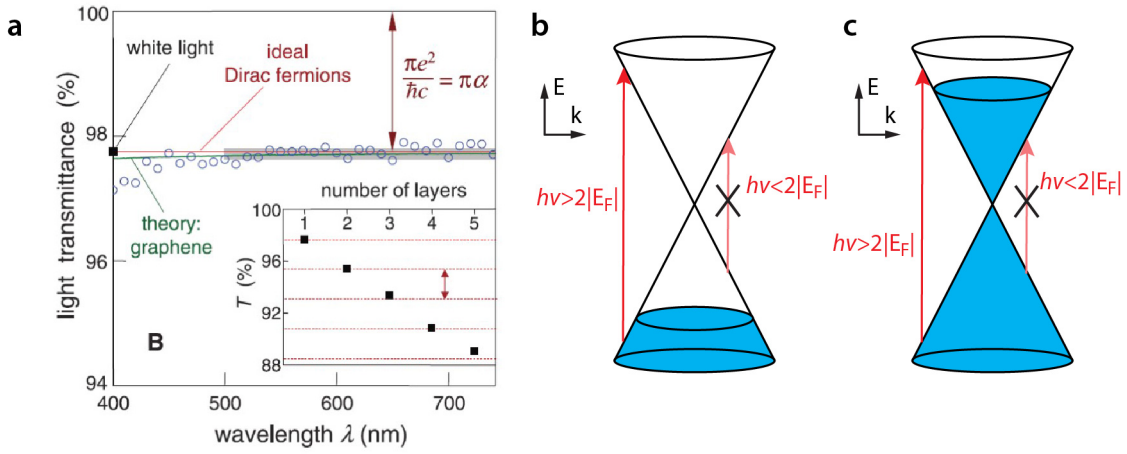

Figure 2.5: Light absorption in graphene. **a)** The transmittance of suspended monolayer graphene across visible wavelengths. **Inset:** Transmittance of white light as a function of layer number for few-layer graphene. Reproduced with permission.[5] Allowed and forbidden transitions for direct excitation of electrons by a photon of energy hv in **b)** p-doped and **c)** n-doped monolayer graphene.

2.3 Optoelectronic devices

2.3.1 Photodetectors

A photodetector is an electronic device which produces a measurable change in current (Iph) and/or voltage (V_{ph}) under illumination with light of an appropriate wavelength. I_{ph} and V_{ph} are referred to as photocurrent and photovoltage respectively. The active materials in photodetectors typically consist of semiconductors. In this thesis, we will also use a semi-metal, graphene. Also, we will only consider photodetectors which produce photocurrent rather than photovoltage signals. Before discussing specific devices which are relevant to this thesis, we will first introduce some general figures of merit.

Responsivity

$$\gamma(\lambda) = \frac{I_{ph}(\lambda)}{P(\lambda)A} \quad [A/W] \tag{2.18}$$

The responsivity (γ) of a photodetector describes its sensitivity to light. It is the photocurrent measured per incident Watt of light. A is the area of the 'photo-active' light-absorbing region of the photodetector and $P(\lambda)$ is the power density of incident light.

External quantum efficiency

$$\eta_{EQE}(\lambda) = \gamma(\lambda) \cdot \frac{hv}{q} \tag{2.19}$$

The external quantum efficiency, or EQE, is the responsivity of a device in terms of fundamental particles. It defines the number of electrons or holes, with charge q, extracted as photocurrent per incident photon of energy hv. $|\eta_{EQE}| \leq 1$ unless the photodetector has an internal amplification mechanism, such as photo-conductive gain.

Internal quantum efficiency

$$\eta_{IQE}(\lambda) = \eta_{EQE}(\lambda)/A_{\lambda}(\lambda) \tag{2.20}$$

The internal quantum efficiency, or IQE, describes the number of charge carriers extracted as photocurrent per absorbed photon. A_{λ} is the absorbance of the photo-active layer.

Noise spectral density

$$Sn = \sqrt{\frac{\int_{f_{lo}}^{f_{hi}} {I_n}^2 \, df}{(f_{hi} - f_{lo})}} \quad \left[AHz^{-1/2}\right] \tag{2.21}$$

The noise spectral density is the electrical noise, I_n^2, of a photodetector integrated over a bandpass frequency range $\Delta f = f_{hi} - f_{lo}$ and normalised to the square root of that bandwidth.

Noise-equivalent power

$$NEP(\lambda) = \frac{S_n\sqrt{\Delta f}}{\gamma(\lambda)} \qquad [W] \tag{2.22}$$

The noise equivalent power, or NEP, is the incident optical power at which $I_{ph}/I_n = 1$ for a noise bandwidth of $\Delta f = 1Hz$. This defines the weakest incident optical power which can produce a measurable photocurrent signal.

Specific Detectivity

$$D^*(\lambda) = \frac{\sqrt{A\Delta f}}{NEP(\lambda)} = \frac{\gamma(\lambda)\sqrt{A}}{S_n} \quad \left[cmW^{-1}Hz^{1/2}\ (Jones)\right] \tag{2.23}$$

Detectivity, $D(\lambda) = 1/NEP(\lambda)$, was originally considered to be the accepted figure of merit by which to compare the sensitivity of different photodetector devices. However, D is affected by extraneous parameters, such as Δf and A, which determine the noise current within a photodetector. Instead, the specific detectivity, D^*, is now widely used to account for these variations. There are several presumed postulates associated with Equation (2.23),[54] which include an assumption that the noise spectral density is governed by 'white noise' ($S_n \propto (f_{BW})^0$) and that $S_n \propto A^{-1/2}$ is true. Both of these conditions

fail in the case of graphene, where $1/f$-type 'flicker noise' is dominant at low operating frequencies ($f_{BW} < 10kHz$).[55] Nevertheless, D^* is still commonly used as a figure of merit for graphene photodetectors.

Linear dynamic range

$$LDR = 10 \times \log_{10}\left(\frac{P_{sat}}{NEP}\right) \quad [dB] \tag{2.24}$$

The linear dynamic range, LDR, defines the range of incident optical power over which responsivity is invariant. The lower limit of this range is set by the noise-equivalent power and the upper limit is set by the saturation power, P_{sat}, at which point the responsivity of a detector begins to change.

2.3.2 Polymer light-emitting diodes

Light emitting diodes are electrically rectifying junctions which emit light under an applied forward bias voltage. Polymer LEDs, or PLEDs, are a sub-set of these devices in which the active light-emitting layers consist of conjugated organic macromolecules. We will only encounter these devices briefly in Chapter 4. The following section is therefore a simplistic overview of a few essential concepts.

PLEDs are operated in forward bias configuration, such that electrons are injected through the cathode and holes are injected through the anode. The work function of each of these electrodes is carefully selected so as to facilitate efficient transport of holes/electrons into the HOMO/LUMO of the active layer respectively. If the alignment between an electrode's work function and an energy band of the active layer is non-ideal, or if an asymmetry in carrier mobility limits the efficiency of recombination, then intermediary electron/hole transport layers and electron/hole blocking layers are employed respectively. A rudimentary energy band diagram of a PLED in forward bias is illustrated in Figure 2.6a. The anode and/or the cathode must be transparent in order to allow light to escape the PLED. The conventional layer structure is to use a transparent anode, wheras inverted structures use transparent cathodes. Examples of these structures are illustrated in Figure 2.6b. In Chapter 4 we will present a novel transparent conductor based upon few-layer graphene and show that it can function as a cathode in inverted PLEDs.

Luminance efficiency

$$\eta_L = \frac{AL}{I_{DS}} \quad [cd/A] \tag{2.25}$$

The luminance efficiency, η_L, describes the luminance (L) of a PLED per unit of current density.[56] Luminance is a photometric unit of light intensity per solid angle which

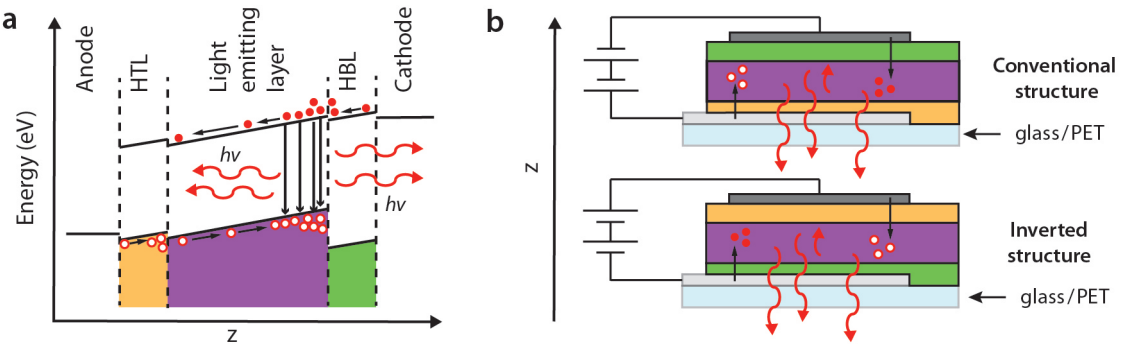

Figure 2.6: Basic working principles of a PLED. a) Energy band diagram of a PLED in forward bias configuration. A hole transport layer (HTL) and hole blocking layer (HBL) are included either side of the light-emitting polymer layer. **b)** Schematics of the conventional and inverted layer structures of PLEDs.

accounts for the responsivity spectrum of the human eye.

2.4 Optoelectronic properties of graphene

2.4.1 Hot electron cooling

A common assumption in semiconductor physics is that photo-excited charge carriers will rapidly transfer their kinetic energy to the lattice as heat and reach thermal equilibrium within sub-picosecond time-scales. This is not necessarily the case in graphene. As we outlined in Section 2.1.3, the small Fermi surface of graphene imposes tight phase-space restrictions on the number of phonon modes available for scattering processes and the maximum energy which may be transferred per collision. These constraints are most extreme at low levels of charge carrier concentration. If an electron is promoted to the conduction band by the absorption of a photon with energy $E_0 < 2eV$, it will initially occupy a state in the linear region of the conduction band with wavenumber $k_h = E_0/2\hbar v_F$. As the excited electron loses energy through electron-electron and electron-phonon scattering, k_h decreases and will rapidly freeze out phonon modes in the same manner as k_F in Figures 2.4d-f. Hence, a bottleneck in electron cooling is reached, where even low-energy collisions with acoustic phonons are infrequent. Excited charge carriers therefore remain 'hot', with their temperature T_h above that of the lattice T_L for as long as 10-100 picoseconds[57,58] depending on the environmental temperature and height of the Fermi level. Figure 2.7a illustrates a population of hot electrons, with chemical potential ϕ_c, located marginally above the Fermi energy in n-doped graphene under conituous wave (CW) illumination. An expression for the rate of scattering events between a conduction electron and a single acoustic phonon in graphene for temperatures outside of the Bloch-Grüneisen regime

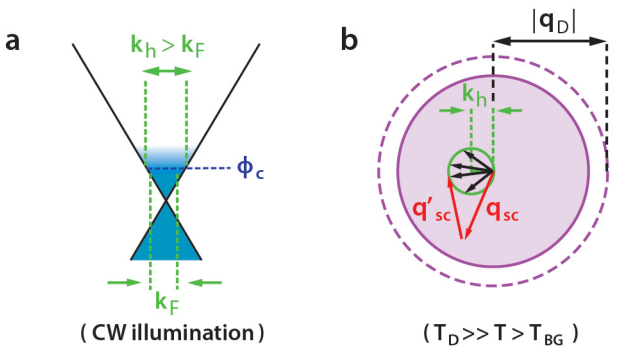

Figure 2.7: Acoustic phonon bottleneck and supercollisions in graphene. a). Band diagram sketch showing a distribution of hot electrons in the conduction band of marginally n-doped graphene. **b)** Phase space scattering diagram which shows momentum-conserving interactions between hot electrons and acoustic phonons (black arrows) and a two-phonon 'supercollision' event, where the hot electron scatters with wavevector $\mathbf{q}_{sc}$ to a site of disorder and recoils with wavevector $\mathbf{q}'_{sc}$.

$(T > T_{BG})$ has been calculated by Hwang et. al.[59] using Boltzmann transport theory.

$$\gamma_h = \frac{3D^2\phi_c^3}{4\pi^2\hbar^3\rho_m {v_F}^4 k_B T_h} \tag{2.26}$$

In Equation (2.26), $D \sim 20eV$ is the typical screened deformation potential on SiO_2/Si substrates[51] and $\rho_m = 7.6{\times}10^{-}7kgm^{-2}$ is the mass density of monolayer graphene.

Under phase space restrictions where conventional electron-phonon scattering mechanisms are suppressed, processes which usually make a negligible contribution towards electron cooling become relevant. The 'supercollision' model[24,25] recognises that short-range scattering at sites of disorder allow a far larger transfer of energy and can be the dominant mechanism of cooling hot carriers. Figure 2.7b sketches an example of such an event. The rate of heat loss (H) when supercollisions are dominant is given by Equation (2.27)

$$H_{SC} = C\left({T_h}^3 - {T_l}^3\right), \quad C = \frac{9.62g^2 D(\phi_c)^2 {k_B}^2}{\hbar k_F l} \tag{2.27}$$

Here, g is the electron-phonon coupling frequency, $D(\phi_c)$ is the density of states and l is the mean free path of hot carriers. The relative contributions of acoustic phonon scattering (H_{AP}) and supercollisions (H_{SC}) to the rate of heat loss from photo-excited charge carriers is determined by the degree of disorder in the sample, the environmental temperature and the size of the Fermi surface.[24]

$$\frac{H_{SC}}{H_{AP}} = \frac{0.77}{k_F l} \cdot \frac{\left({T_h}^2 + T_h T_L + {T_L}^2\right)}{{T_{BG}}^2} \tag{2.28}$$

2.4.2 Photocurrent mechanisms

A wide range of physical mechanisms can produce current in graphene under illumination.[21] As a starting point, we will consider short circuit ($V_{DS} = 0V$) photocurrent signals that are relevant to asymmetrically-doped lateral graphene junctions, such as the example illustrated in Figures 2.8a and 2.8b. In these devices, two discrete regions of the channel are doped such that a local gradient in the chemical potential of charge carriers, $\nabla\phi_c$, is present at the interface. Here, the chemical potential defines the 'quasi-Fermi level' of excited charge carriers. Under dark conditions, if $k_BT << E_F$. Possible methods of creating this arrangement include local electrostatic gating[23,26,60,61] or selective chemical doping.[27,62–64] We will present one such method in Chapter 5. We can express the short circuit current density, $\mathbf{J}_{ph}$, as a summation of the photovoltaic and photothermoelectric mechanisms affecting charge transport within these devices.[22]

$$\mathbf{J}_{ph} = -\mu n_{ph}(\mathbf{r})\nabla\phi_c(\mathbf{r}) + \sigma S\nabla T_h \tag{2.29}$$

Here, the chemical potential is evaluated from a reference potential energy, E_{CNP}, at charge neutrality in graphene ($E_{CNP} - E_{vac} \approx 4.55eV$ with respect to the vacuum level[65]). An example of this convention is illustrated in Figure 2.8a. For the sake of visualising band bending across the interface, we will plot spatial variations in $-\phi_c(\mathbf{r})$. The first term on the right hand side of Equation (2.29) describes the movement of a photo-excited charge carrier density, n_{ph}, under the built-in chemical potential gradient at the interface. The second term accounts for the diffusion of hot charge carriers along a temperature gradient ∇T_h, which is created by illuminating the interface with a focused light source. T_h refers to the temperature of hot charge carriers which, from our discussion in Section 2.4.1, cannot always be assumed to equilibrate with the lattice. S is the Seebeck coefficient, also known as the absolute thermoelectric power.[66] These two terms are commonly referred to as the 'photovoltaic effect' and the 'photothermoelectric effect' in literature relating to graphene and two-dimensional materials.[21] This nomenclature does not correlate with the general definition of the photovoltaic effect as any combination of physical processes which produce both a measurable voltage and current when a material is illuminated (assuming an appropriate load resistance is connected in series). The general definition would encompass both terms in Equation (2.29). Having addressed this disparity, in this thesis we will maintain the nomenclature established by the graphene research community by referring to 'photovoltaic' and 'photothermoelectric' components of photocurrent. Rearranging Equation (2.29), we can define the net short circuit photocurrent, I_{ph},flowing across the graphene interface.

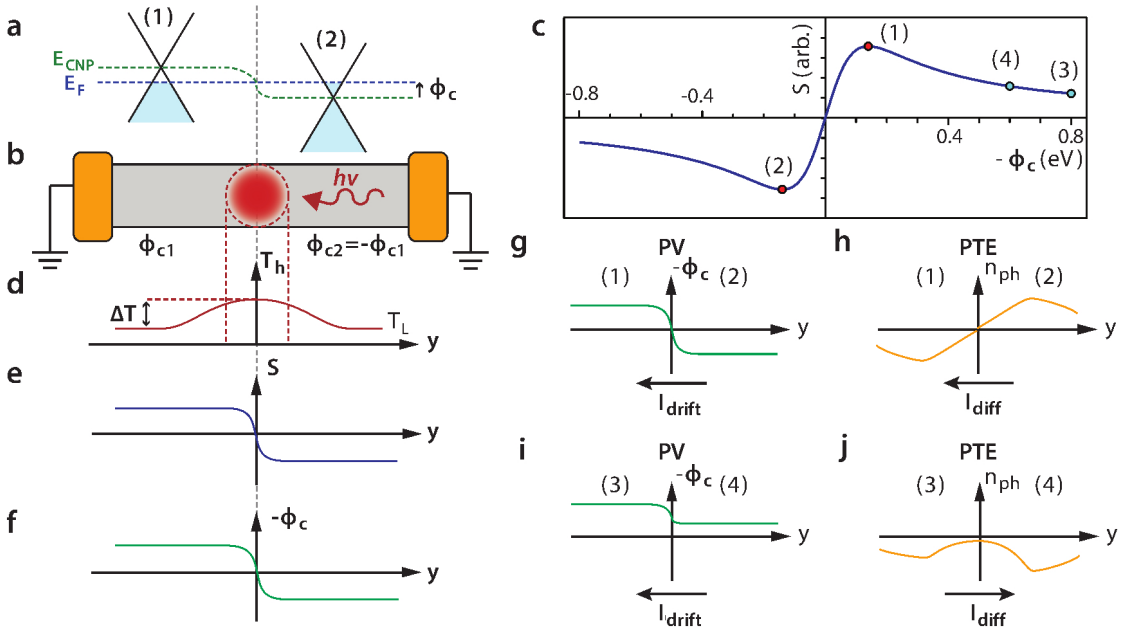

Figure 2.8: Photo-thermoelectric and photovoltaic contributions to photocurrent in graphene at short circuit. **a)** Energy band diagrams illustrating the asymmetric doping in regions (1) and (2) either side of a p-n junction in graphene. **b)** Sketch of a graphene p-n junction illuminated locally at the interface with a focussed laser. The chemical potential of regions (1) and (2) are equal and opposite with respect to the charge neutrality point. **c)** The Seebeck coefficient of graphene as a function of chemical potential according to the Mott relation in Equation (2.33). **d)** Sketched temperature of excited charge carriers as a function of displacement from the illuminated p-n junction in b). Note that $\Delta T > 0$ is sustained outside of the laser spot profile. Changes in **e)** the Seebeck coefficient and **f)** chemical potential are sketched across the same junction. The direction of conventional current (positive charge carriers) is shown for photovoltaic (PV) and photo-thermoelectric (PTE) mechanisms across **g)**, **h)** a p-n junction and **i)**, **j)** a p-p' junction in graphene according to sketched gradients in chemical potential and photo-excited charge carrier density. $n_{ph} < 0$ corresponds to holes as free charge carriers. The chemical potential across each junction is labelled in c).

$$I_{ph} = \frac{1}{RW} \int_{-W/2}^{W/2} \int_{-L/2}^{L/2} \left[S\left(x,y\right) \nabla T_h\left(x,y\right) - \sigma^{-1}\left(x,y\right) \mu n_{ph}\left(x,y\right) \nabla \phi_c\left(x,y\right) \right] dydx \tag{2.30}$$

Here, L, W and R are the length, width and total resistance of the graphene channel respectively.

Photo-thermoelectric effects in graphene

The Seebeck coefficient describes the extent to which charge carriers in a metal or semiconductor will re-distribute via diffusion under a temperature gradient.[49]

$$S = -\Delta V / \Delta T \tag{2.31}$$

Equation 2.31 describes the polarity convention of the Seebeck coefficient, whereby a positive/negative coefficient corresponds to positive/negative charge accumulating at the cold side of a temperature gradient. Unless minority charge carriers have a significantly higher diffusion coefficient than majority charge carriers, this usually results in p-type/n-type metals and semiconductors displaying a positive/negative Seebeck coefficient. The Mott relation,[49,67] shown in Equation (2.32) can be used to calculate the Seebeck coefficient of graphene.[68]

$$S = -\frac{\pi^2 {k_B}^2 T_h}{3e} \cdot \frac{1}{\sigma\left(\phi_c\right)} \cdot \frac{\partial \sigma\left(E\right)}{\partial E}\Big|_{E=\phi_c} \tag{2.32}$$

This model is based upon the Sommerfeld expansion so is only valid for degenerate semiconductors and metals at temperatures where $k_B T << \phi_c$. Using equation (2.13), we can express the Seebeck coefficient in terms of the chemical potential of graphene.

$$S = -\frac{\pi^2 k_B T_h}{3e} \cdot \frac{2\phi_c}{\left(\Lambda^2 + \phi_c^2\right)} \tag{2.33}$$

We plot the function $S(\phi_c)$ in Figure 2.8b with T_h assumed to be constant. This approximation breaks down at extremely high levels of doping (T_h will approach the lattice temperature) but our estimate of the Seebeck coefficient is not radically affected because $\left(\partial\sigma/\partial E\right)/\sigma$ tends towards zero in this regime anyway. The gradient of $S(\phi_c)$ changes sign twice throughout the energy range plotted in Figure 2.8b, resulting in a 'sixfold pattern' of photocurrent polarity in devices with split electrostatic gates.[23,60] This is considered to be a hallmark signature of thermoelectric effects in graphene.

The temperature of photo-excited charge carriers across the a p-n junction in graphene is sketched in Figure 2.8d. Hot carriers are created at the locally illuminated junction and diffuse outwards, maintaining an elevated temperature over the cooling length, ξ.[22]

$$\xi = \sqrt{\frac{\kappa}{\gamma_h C_{el}}} \tag{2.34}$$

Here, κ is the thermal conductivity of graphene, γ_h is the electron phonon scattering rate and C_{el} is the specific heat capacity of charge carriers. The elevated temperature of hot carriers at the interface relative to the lattice, $\Delta T = T_h - T_L$, is a difficult term to measure experimentally. In Chapter 5, we use a solution offered by Song et. al,[22] who have developed a general expression for ΔT using Green's function. They assume a Guassiam laser beam profile and all parameters except T_h to be invariant along the channel's width.

$$\Delta T = \frac{\alpha_\lambda \epsilon_0 l_0 N_{ph}}{\frac{\kappa_1}{\xi_1} coth\left(\frac{L}{2\xi_1}\right) + \frac{\kappa_2}{\xi_2} coth\left(\frac{L}{2\xi_2}\right) + \frac{T_0}{RW}\left(S_2 - S_1\right)^2} \tag{2.35}$$

In Equation (2.35), α_λ is the fraction of an absorbed photon's energy which is retained by the hot electron system at quasi-equilibrium. l_0 is the laser spot diameter and N_{ph} represents the flux of photons absorbed at the junction averaged over the channel's width.

If the p-n interface is sharp and doping in each region is uniform, the change in Seebeck coefficient sketched in Figure 2.8e can be approximated as a step function and Equation (2.30) becomes

$$I_{PTE} = \frac{1}{R}\left(S_1 - S_2\right)\Delta T. \tag{2.36}$$

ΔT is often mistaken as the temperature difference either side of the junction due to unclear definitions of Equation (2.36) in two highly-cited review articles.[21,69] Substituting into Equation (2.36), we arrive at an expression in terms of the chemical potential (see Figure 2.8f) and conductivity either side of the channel.

$$I_{PTE} = \frac{2\pi^2 k_B^2 T_h}{3eR} \cdot \frac{\Delta T}{\phi_{c1}\phi_{c2}} \cdot \left[\phi_{c2}\left(1 - \frac{\sigma_{min}}{\sigma_1}\right) - \phi_{c1}\left(1 - \frac{\sigma_{min}}{\sigma_2}\right)\right] \tag{2.37}$$

As a last point, we can use Equation 2.37 to examine the power dependence of photo-thermoelectric current in graphene.[25] The hot carrier cooling rates, H, predicted for the electron-phonon scattering models of supercollisions[24,25] and acoustic phonon scattering[24,70] are listed in the second column of Figure 2.9. Under continuous-wave illumination, a steady-state is reached when the optical power imparted to hot carriers equals the rate of heat transfer to the lattice ($P = H$). The proportionality $H \propto T_h$ of each cooling rate can be substituted into Equation (2.37)) to find the power law $I_{diff} \propto P^\alpha$.[25] Resultant values of α for the regimes of high and low incident optical powers ($T_h >> T_L$ and $T_h << T_L$ respectively) are listed in the last two columns of Figure 2.9. Upon comparison, it becomes clear that the responsivity of graphene photodetectors which exhibit photo-thermoelectric

Electron - phonon scattering model	$\mathbf{P(T_h)} = H(T_h)$	$\boldsymbol{\alpha}$ $(T_h \gg T_l)$	$\boldsymbol{\alpha}$ $(T_h - T_l \ll T_l)$
Supercollision (disorder)	$A\left({T_h}^3 - {T_l}^3\right)$	2/3	≈ 1
Acoustic phonons $(k_B T >> E_F)$	$A' {T_h}^4 (T_h - T_l)$	2/5	≈ 1
Acoustic phonons $(k_B T << E_F)$	$A''(T_h - T_l)$	n/a	≈ 1

Figure 2.9: Power dependence of photo-thermoelectric current in graphene. Compiled power exponents, α, of photo-thermoelectric current models where $I_{diff} \propto P^{\alpha}$. α is calculated for both the high optical power/low temperature ($T_h >> T_L$) and low temperature/high optical power ($T_h << T_L$) regimes based on the electron cooling rate, H. In total, α is predicted for three different hot-carrier phonon scattering regimes: supercollisions,[24,25] acoustic phonon scattering at low doping[24] and acoustic phonon scattering at high doping.[70] A, A' and A'' are separate coefficients.

current signals are unstable to variations in temperature, ambient doping, disorder and optical power. This is not ideal for applications such as radiometry, where a consistent and simple power law is essential over a wide dynamic range. In Chapter 5, we will address this issue using $FeCl_3$-intercalated few-layer graphene.

Photovoltaic effects in graphene

The photovoltaic term in equation (2.30) can be simplified if we make the assumption that parameters are invariant across the channel width and substitute conductivity terms with Equation (2.13).

$$I_{PV} = -\frac{\mu\, n_{ph\,(y=0)}}{\sigma_{min} R} \int_{-L/2}^{L/2} \nabla\phi_c\,(y) \cdot \left(1 + \frac{\phi_c(y)^2}{\Lambda^2}\right)^{-1} dy \tag{2.38}$$

By changing variables, we find a complete expression for the photovoltaic contribution to short circuit photocurrent:

$$I_{PV} = \frac{\mu n_{ph} \Lambda}{\sigma_{min} R} \cdot \left[tan^{-1}\left(\frac{\phi_{c1}}{\Lambda}\right) - tan^{-1}\left(\frac{\phi_{c2}}{\Lambda}\right)\right] \tag{2.39}$$

Equations (2.37) and (2.39), which are based upon the work of Song et. al.,[22] will be applied to the case of $FeCl_3$-intercalated few-layer graphene in Chapter 5.

Photoconductivity of graphene

If a voltage is applied between the source and drain electrodes of a graphene transistor, incident light will modulate the channel's conductivity via temperature-induced changes

to the charge carrier mobility and/or an increasing the number of free charge carriers. A local change in the density of states (e.g. a p-n junction) is therefore no longer required to observe a photocurrent signal.

The temperature-dependent component of photoconductivity, known as the 'bolometric effect', is governed by the same electron-phonon scattering processes which we have already applied to hot carrier diffusion in short-circuit photocurrent signals.[71] For the case of graphene, $\sigma \propto T^{-4}$ in the Bloch-Grüneisen regime ($T < T_{BG}$) and $\sigma \propto T^{-1}$ in the 'equipartition regime' ($T > T_{BG}$).[59] Over a small range of temperatures, an empirical bolometric coefficient, β, can be measured to describe this effect.[71]

$$\beta(V_G) = \Delta I(V_G)/\Delta T \tag{2.40}$$

The bolometric coefficient will vary according to the heat-sinking characteristics of each device's substrate.

The second component of photoconductivity is simply a change in conductivity when a density of free charge carriers, n_{ph}, is excited under illumination.[72]

$$\Delta\sigma = q n_{ph} \mu \tag{2.41}$$

Photo-excited charge carriers will recombine after an average lifetime τ_L. This lifetime is a weighted average of several time constants if a variety of charge trap states are present. The generation rate of charge carriers in steady state is therefore given by Equation (2.42).

$$\frac{n_{ph}}{\tau_L} = A_\lambda \cdot \frac{P}{hv} \tag{2.42}$$

Here, A_λ is the absorbance of graphene. Substituting Equation (2.41) into Ohms law, we find an expression for the photocurrent density.

$$J_{ph} = \frac{e\mu n_{ph} V_{DS}}{L} \tag{2.43}$$

If we then substitute Equation 2.42 into Equation (2.43), we can re-arrange for an expression of the external quantum efficiency, $\eta_{EQE} = (hv/e)(J_{ph}/PL)$, of drift-assisted photoconductivity in graphene.

$$\eta_{EQE} = (A_\lambda) \cdot \left(\frac{\tau_L \mu V_{DS}}{L^2} \right) \tag{2.44}$$

The left set of brackets enclose a quantum efficiency term which describes the number of free charge carriers created per incident photon. We have equated this to absorbance because electron-hole pairs do not form tightly-bound excitonic states in graphene, so an

absorbed photon should almost certainly produce free charge carriers. The right term in brackets describes the photo-conductive gain, G, under an applied source-drain bias voltage. This can be expressed purely in terms of timescales

$$G = \frac{\tau_L}{\tau_{tr}} \tag{2.45}$$

where $\tau_{tr} = L^2/\mu V_{DS}$ is the transit time for a photo-excited charge carrier to drift between source and drain electrodes. It follows that if long-lived charge carriers drift across a suitably small channel length. then $\tau_L/\tau_{tr} >> 1$ and we have a mechanism of amplifying photocurrent signals. However, photo-excited charge carriers in monolayer graphene typically only last 1-100 picoseconds before recombining to their ground state.[57,58] This makes graphene photodetectors extremely fast, with intrinsic operational bandwidths approaching $500GHz$,[73] but it also means that photo-conductive gain cannot be realised in practical device geometries. Furthermore, as was discussed in Section 2.2.1, monolayer graphene exhibits weak, broadband absorbance of $A_\lambda \approx 0.023$.[5] A combination of low absorbance and short carrier lifetime results in very weak response to light ($\eta_{EQE} \sim (0.01 - 1)\%$ and $\gamma \sim (10^{-4} - 10^{-2})AW^{-1}$) in graphene photodetectors without the use of plasmonic arrays or wave-guides to enhance absorption.[21] A commonly employed method to overcome these challenges is to combine graphene with a semiconductor material which enhances light absorption and τ_L such that a net gain ($\eta_{EQE} > 100\%$) can be achieved.

Photo-gating effects

The 'photo-gating effect' occurs in photodetectors where a semiconductor layer is placed in direct contact with the channel of a graphene transistor, as is illustrated in Figure 2.10a. These device structures are referred to as phototransistors.[29] Similar to photo-conductive devices, phototransistors are operated with a non-zero bias voltage (V_{DS}) applied between source and drain electrodes. Under illumination with photons of energy $hv > E_g$, where E_g is the band gap energy of the semiconductor, electron-hole pairs are generated in the semiconductor layer with efficiency η_{gen}. Depending on the dielectric constant, the Coulombic force of attraction between the electron and hole can either be overcome by k_BT or will require a suitably large electric field to facilitate dissociation into free charge carriers. In either case, the efficiency of dissociation is η_{diss}. Once dissociated, charge carriers can be separated across either side of the graphene-semiconductor interface according to a built-in field or selective trapping of electrons/holes in the semiconductor layer. The efficiency with which one of the free charge carriers from the dissociated electron-hole pair transfers across the interface is η_{CT}. The result of this entire process is that the charge

carrier density in graphene is modulated under illumination. This is illustrated in the band diagram and energy level diagram in Figure 2.10b. The generation rate of excited charge carriers in graphene due to the photo-gating effect can be expressed as

$$\frac{\Delta n}{\tau_L} = \eta_{PG} \cdot \frac{P}{hv} \tag{2.46}$$

where τ_L is the average lifetime of the photo-excited charge carrier which remains in the semiconductor layer. $\eta_{PG} = \eta_{gen}\eta_{diss}\eta_{CT}$ is the photo-gating quantum efficiency (PGQE), it describes the number of charge carriers injected into graphene per incident photon. If the phototransistor is electrostatically gated, it follows from Equation (2.8) that illuminating the channel will shift the gate voltage required to achieve charge neutrality in graphene, ΔV_{CNP}. This is sketched in Figure 2.46c. The semiconductor layer therefore effectively acts as a light-modulated electrostatic gate, hence the term photo-gating.

Excluding the mechanism of charge carrier generation, the photocurrent density measured at the electrodes is governed by the photo-conductive effect (Equation (2.43)). We can therefore treat Equation (2.46) in the same manner as Equation (2.42) to develop an expression for the external quantum efficiency of graphene phototransistors.

$$\eta_{EQE} = (\eta_{PG}) \cdot \left(\frac{\tau_L \mu V_{DS}}{L^2} \right) \tag{2.47}$$

The appeal of graphene phototransistors in comparison to graphene photoconductors now becomes apparent. If the charge carrier dynamics illustrated in Figure 2.10d can be tailored such that η_{PG} is maximised and $\tau_L >> \tau_{tr}$, graphene can be engineered into an amplified photodetector which is capable of responding to light signals that are many orders of magnitude below the noise-equivalent power of the lateral junctions measured in short circuit and the pristine photo-conductive devices discussed earlier. We will present a novel variation of a graphene phototransistor in Chapter 6.

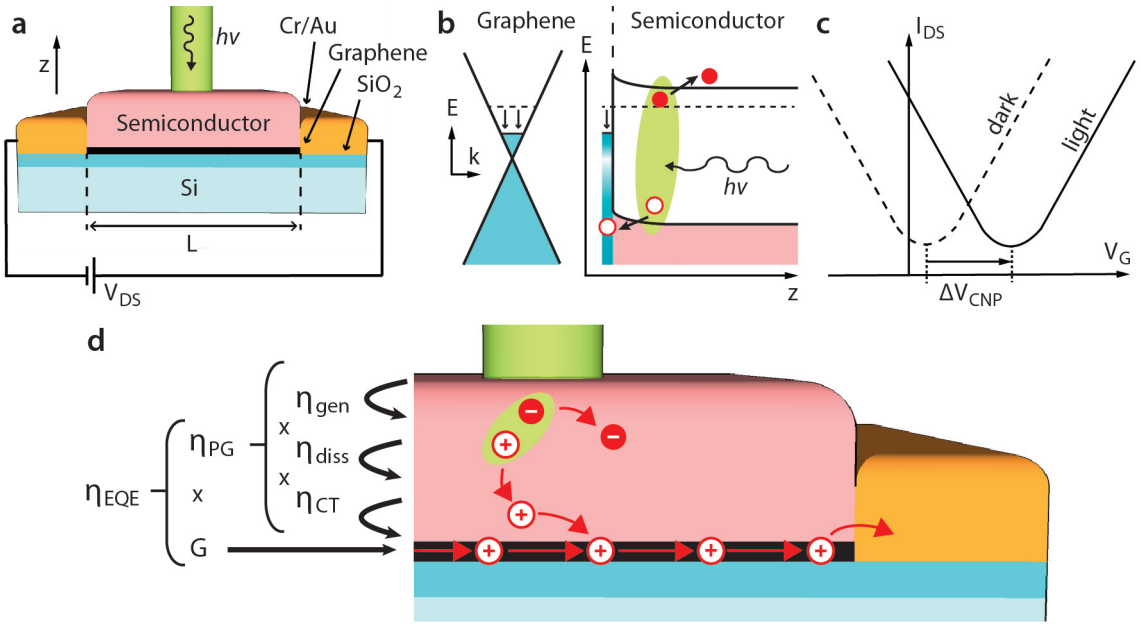

Figure 2.10: Working principles of a graphene phototransistor. a) Illustrated device structure of a graphene phototransistor. **b)** Left: Sketched band diagram of graphene showing the change in chemical potential (dashed line) when the phototransistor is illuminated. Right: Energy band diagram of a graphene-semiconductor interface. In the semiconductor, electrostatically bound excitons dissociate into free charge carriers and are separated by the built-in field at the interface. **c)** Electrical read-out of a graphene phototransistor. Transfer of photo-excited electrons/holes from the semiconductor to graphene cause a down-shift/up-shift of the charge neutrality point by ΔV_{CNP}. **d)** Sketch of the charge carrier dynamics in graphene phototransistors with associated quantum efficiency terms, η. Generation of an electron hole pair (η_{gen}), dissociation into free charge carriers (η_{diss}), charge transfer of charge carriers to graphene (η_{CT}), photo-gating quantum efficiency (η_{PG}), photo-conductive gain (G) and external quantum efficiency (η_{EQE}).

2.5 Rubrene single crystals

Small molecule organic semiconductors differ markedly from inorganic semiconductors. The bonding between organic molecules is typically governed by very weak Van der Waals forces in comparison to covalent and ionic bonds across the lattice of an inorganic semiconductor. In general, this makes organic semiconductors more pliable than inorganic counterparts and allows them to be synthesised at far lower temperatures. Both of these traits are appealing for the purposes of developing cheap, flexible electronic devices. However, the lack of significant overlap between the electronic wavefunctions of neighbouring molecules means that transport of charge carriers in organic semiconductors is comparatively poor and can be particularly sensitive to defects or grain boundaries within a polycrystalline film. The use of highly-ordered single crystal organic semiconductors presents a better prospect of accessing the intrinsic charge transport properties of organic semiconductors. It should be noted, however, that interactions between the crystal surface and the sample substrate will still present limitations.[74] Growth of organic single crystals will be discussed in Section 3.2.

In Chapter 6, we demonstrate that single crystals of a small molecule organic semiconductor, rubrene, can be used as a light-absorbing layer in graphene phototransistors. Rubrene is a polyacene; it is comprised of four phenyl groups bonded to the two central benzene rings of a tetracene molecule. The structures of tetracene and rubrene molecules are illustrated in Figures 2.11a and 2.11b respectively. Each carbon atom in these benzene rings form the same sp^2-hybridised orbitals as in graphene, with strong σ-bonds between carbon atoms and p_z orbitals oriented perpendicular to the plane of the benzene rings. As we have just mentioned, inter-molecular forces are quite weak in organic semiconductors. As a result the electronic structure of a crystalline organic semiconductor will largely correlate with the energy levels of an isolated molecule. The highest occupied molecular orbital (HOMO) and lowest unoccupied molecular orbital (LUMO) of a rubrene molecule are shown in terms of their probability density functions in Figures 2.11c and 2.11d respectively. These represent the highest energy ground state and first excited state for π electrons in a rubrene molecule. These energy levels are $E_{HOMO} = -4.69eV$ and $E_{LUMO} = -2.09eV$ from the vacuum level respectively.[75] The side-arms of rubrene are oriented such that the plane of each phenyl ring lies almost perpendicular ($\sim 85^o$)[75] to the plane of the tetracene backbone. As a result, p_z orbitals on the side-arms do not intermix with the rest of the molecule and the HOMO/LUMO orbitals of rubrene remain much the same as tetracene. The phenyl side groups do, however, have a large effect on the arrangement of molecules in a rubrene crystal. Figure 2.11e shows that, without these side-arms,

tetracene molecules arrange in a 'herringbone' stacking formation whereby they form rows along the crystal's b axis with the M axis of each molecule parallel (molecular axis labels are shown in Figure 2.11c). This arrangement does not allow for much overlap of molecular orbitals projected along the N axis of each molecule. As a result, tetracene single crystals exhibit a maximum room-temperature field-effect mobility of $\mu_h \approx 1.6 cm^2 V^{-1} s^{-1}$.[74] In the case of rubrene, the phenyl side-arms encourage molecules to form the same herringbone stacking pattern across the ab plane of the crystal. In this case, however, the molecules arrange in staggered rows with significant co-facial overlap of molecules along the crystal's b axis[76] (see Figure 2.11f). This results in a room-temperature field-effect mobility of $\mu_h \approx 20 cm^2 V^{-1} s^{-1}$,[74] which is extremely high for an organic semiconductor. Electronic coupling between rubrene molecules broadens the HOMO and LUMO levels such that electrons and holes travel in narrow energy bands.[75]

The significant overlap of neighbouring molecular orbitals in rubrene single crystals has implications for the ability of photo-excited excitons to diffuse throughout the crystal. Experimental observations of long-range photoluminescence quenching[77] and delayed surface photoconductivity signals[78] in rubrene single crystals suggest that long-lived triplet excitons are formed under illumination via fission of singlet states. Triplet states have a total spin number $S = 1$ and multiplicity $M_S = 3$, in comparison to singlet states where $S = 0$ and $M_S = 1$.[79] Because the electric dipole operator associated with radiative transitions cannot change the symmetry of both the spatial distribution and spin components of a multi-particle wavefunction,[80] triplet states are forbidden from fast fluorescent decay to a singlet ground state and remain excited for microsecond time-scales or longer. Triplets also cannot diffuse via Förster-type resonant energy transfer, which requires an ove rlap between the emission and absorption spectra of initial and final states.[81] Instead, it is expected that triplet excitons diffuse via Dexter energy transfer which necessitates an overlap between both the HOMO and LUMO levels of neighbouring molecules.[82] Although this is an ongoing topic of research, efficient Dexter energy transfer in rubrene is thought to enable triplet states to diffuse as far as $1 \mu m$ before re-combining.[77,83] This offers a method by which to overcome the conflicting geometric requirements of efficient light absorption and efficient extraction of photo-excited charge carriers in organic semiconductors. For these reasons, we considered rubrene single crystals to be a novel choice of material to trial as the light-absorbing layer in an organic semiconductor-graphene phototransistor. We explore this further in Chapter 6.

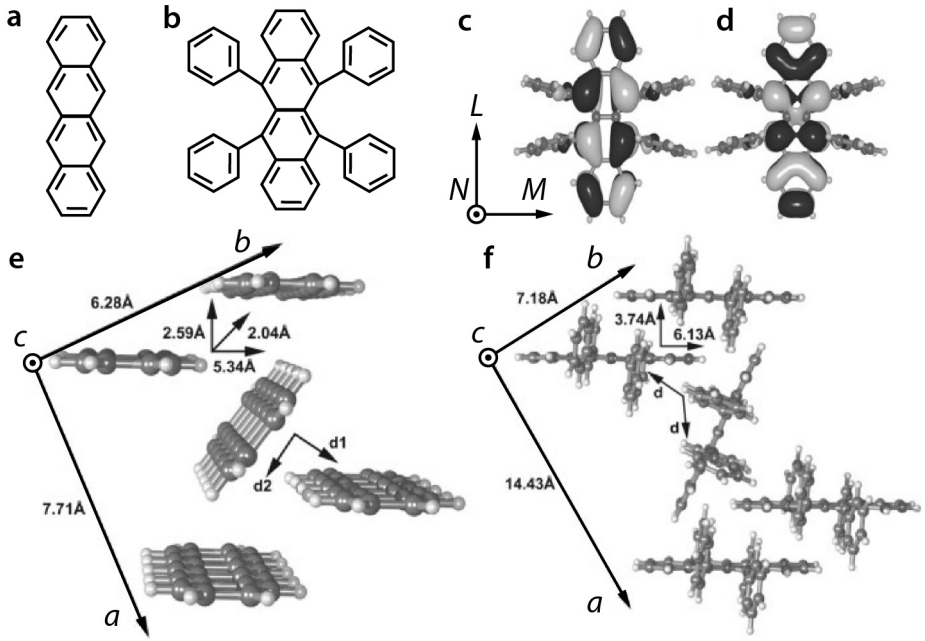

Figure 2.11: Structural of rubrene and tetracene crystals. Two dimensional drawings of the molecular structure of **a)** tetracene and **b)** rubrene, which contains a tetracene backbone. C-H bonds have been omitted. The **c)** HOMO and **d)** LUMO wavefunctions of rubrene molecules are confined to the tetracene backbone and remain similar to those of tetracene molecules. The phenyl side groups affect the molecular stacking arrangement of rubrene molecules. **e)** Tetracene molecules form a herringbone structure along the short axis with very little overlap between neighbouring molecular orbitals. **f)** Rubrene molecules assume herringbone stacking along the long axes of the tetracene backbones with a significant transfer integral along the b axis of the crystal. c)-f) are adapted with permission.[75]

3

Experimental Techniques

3.1 Synthesis of graphene

3.1.1 Chemical vapour deposition of graphene

Chemical vapour deposition techniques are used in Chapters 4 and 6 to produce large-area continuous films of few-layer and monolayer graphene respectively. Both of these processes involve the heating of a carbon feed-stock, in our case methane gas, in the presence of a metal catalyst which breaks the gas down and initiates the growth of graphene films on its surface. A detailed review of CVD growth processes is beyond the scope of this thesis. We include the essential process details relating to the monolayer films fabricated in Chapter 6 below. Few-layer graphene films used in Chapter 4 were purchased from a commercial supplier (*Graphene Supermarket*).

Continuous $1cm^2$ films of monolayer graphene used in Chapter 6 were grown on 25μm thick Cu foils (99.999% pure, *Alfa Aesar*) via chemical vapour deposition in a cold wall furnace (*Moorfield NanoCVD-8G*). Cu foils were pressed flat and loaded onto the ceramic heated stage of the furnace chamber which was then purged with Ar gas and evacuated to a pressure below $0.01Torr$. Foils were initially annealed by increasing the stage temperature under a H_2 flow rate of $0.4sccm$ and pressure of $0.01Torr$. Upon reaching 1035^oC, the stage temperature was kept constant for 10 minutes under the same conditions. After annealing, the temperature was reduced to 1000^oC and continuous films of graphene were synthesised via a two stage growth process: nucleation of carbon feedstock for $40s$ with H_2 and CH_4 flow rates of $0.4sccm$ and $1.4sccm$ respectively, followed by growth and coalescence of the graphene grains with an increased CH_4 flow rate of $7sccm$ for $360s$. Once complete, the stage was cooled to room temperature under an argon flow rate of $0.4sccm$ before the chamber was vented. Growth parameters used are based upon those reported by Bointon et al.[84]

3.1.2 Intercalation of few-layer graphene

Intercalation describes a phenomenon whereby atomic or molecular species are inserted between the planar sheets of a Van der Waals-stacked material such as few-layer graphene. The practice of intercalating few-layer graphene was directly inspired from earlier research efforts conducted throughout the 20th century concerning intercalation compounds of bulk graphite. A comprehensive review of this topic is provided by Dresselhaus et. al.[85] Intercalation compounds are fabricated by numerous variations of a two-zone physical vapour transport method. In the case of our experiments, this is conducted in a digitally-controlled three-zone furnace, where the third zone is surplus to requirement. A schematic of our apparatus is shown in Figure 3.1a. A sample of few-layer graphene on Si/SiO_2, quartz or any other substrate which is impervious to Cl_2 gas is loaded into a quartz tube and positioned in zone-1 of the furnace. A glass vial containing anhydrous $FeCl_3$ powder is then loaded into the other side of the quartz tube and positioned in zone-2 of the furnace. $FeCl_3$ is extremely hygroscopic, so this loading process must be performed quickly if the powder is to remain dry. Once loaded and sealed with vacuum flanges, the quartz tube is evacuated to a pressure of $10^{-6}mbar$ using a turbo-molecular pump and rotary pump in series. Approximately 30 minutes after reaching base pressure, the quartz tube is isolated from the vacuum line and the heating process sketched in Figure 3.1b is initiated. The temperature of each zone is increased at an identical rate until zones 1 and 2 reach stable temperatures of T_G and T_i respectively. Both T_G and T_i must be sufficiently high for $FeCl_3$ to sublimate and the condition $T_G > T_i$ is generally adhered to in order to avoid condensation of intercalant species on the surface of few-layer graphene. After a set run time, each zone is allowed to cool to room temperature, with the cooling of zone-2 initiated first as an additional attempt to avoid condensation on samples. The temperature difference between intercalant and sample zones, $T_G - T_i$, is a crucial parameter and will affect the number of graphene layers which $FeCl_3$ vapour is able to diffuse between. The degree of intercalation can be quantified in terms of the staging index, a positive integer which represents the number of graphene layers between each successfully inserted layer of intercalant molecules. A diagram for the case of potassium-intercalated graphite is provided in Figure 3.1c. In the case of few-layer graphene, we typically deal with five or less graphene layers, so staging indexes of 1, 2 and > 2 are sufficient to describe our samples. The optimum intercalation run parameters used throughout this thesis are $T_G = 360^oC$ and $T_i = 315^oC$ maintained for 12 hours.

$FeCl_3$ acts as an acceptor molecule in proximity to graphene, with DFT models predicting a shift in Fermi energy of $-1eV$ from charge neutrality for a graphene sheet

intercalated to stage-1.[86] This presents a radical degree of p-doping compared to what is practically achievable with electrostatic gating (see Equation (2.10)) and so should significantly impact the optical and electronic properties of few-layer graphene. Figures 3.2a-c detail these effects.[18] In mechanically exfoliated graphene flakes, $FeCl_3$ intercalation does not, in fact, produce a significant change in transmittance to visible wavelengths (comparing Figure 3.2a with Figure 3.2b). This can be attributed to an enhancement in $Tr(\lambda)$ due to the eliminated interband transitions in highly-doped graphene (see Figure 2.5b) and an approximately equivalent reduction in $Tr(\lambda)$ due to the additional absorbance of $FeCl_3$ molecules. A notable change does occur, however, in the electrical properties of few-layer graphene flakes after intercalation with $FeCl_3$. Magneto-transport measurements,[18] and Raman spectroscopy measurements which will be discussed later, show $FeCl_3$ molecules surrounding stage-1 intercalated graphene sheets to electrically de-couple them from adjacent layers. As a result, the electronic structure of fully intercalated $FeCl_3$-FLG may be considered as a parallel stack of highly-doped monolayers. Charge carrier densities as high as $n_h = 1 \times 10^{15} cm^{-2}$ and an extremely low sheet resistance, $R_{sq} = RW/L$, of $9\Omega/sq$ are achieved in in five-layer flakes compared to $R_{sq} \approx 150\Omega/sq$ in pristine equivalents. This combination of low sheet resistance and high transmittance makes $FeCl_3$-FLG an appealing material for use as a transparent electrode in optoelectronic devices such as LEDs and photovoltaic cells. This is demonstrated in Figure 3.2c,[18] where the sheet resistance and transmittance of transparent conductive electrode materials are compared for a variety material thickness. For an optimum thickness of 3-5 layers, stage-1 intercalated $FeCl_3$-FLG outperforms indium tin oxide (ITO) thin films, which are widely used in commercial devices. Surprisingly, the hygroscopic nature of $FeCl_3$ does not result in instability of these films to humid environments[20] and, as results in later Chapters will show, the staging index is not significantly affected by exposure to organic solvents. The remaining challenge to address before $FeCl_3$-FLG can be incorporated into practically sized optoelectronic devices is to produce macroscopic films of this material rather than microscopic flakes. We will address this matter in Chapter 4.

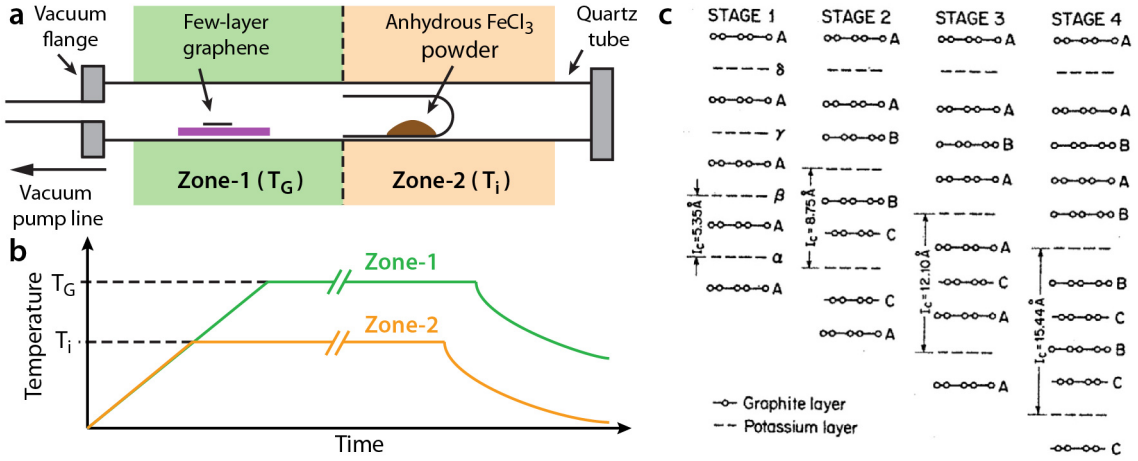

Figure 3.1: Intercalation of few-layer graphene. **a)** Schematic of the two-zone physical vapour transport method used to intercalate few-layer graphene with $FeCl_3$. **b)** Sketched plots of the relative temperature of each furnace zone during an intercalation cycle. **c)** Diagrams outlining the staging index nomenclature for graphite and few-layer graphene intercalation compounds. c) is reproduced with permission.[85]

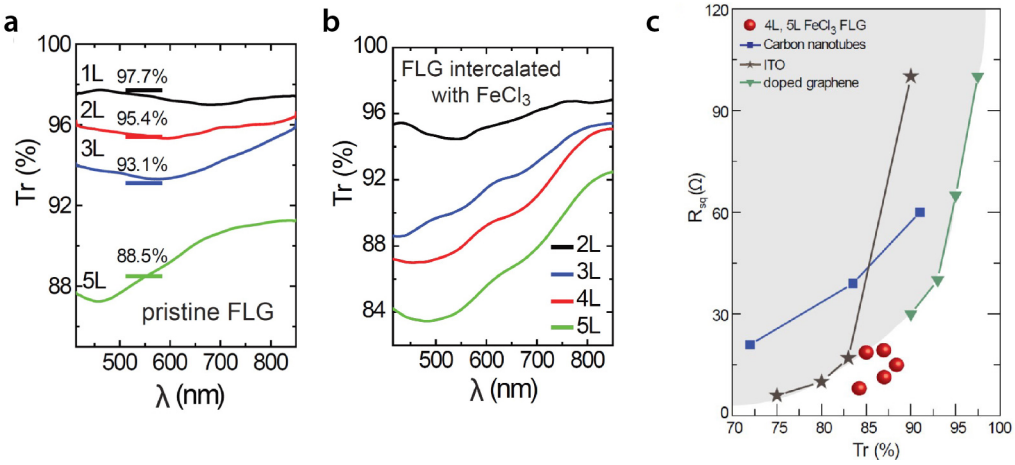

Figure 3.2: $FeCl_3$-FLG flakes as a transparent electrode. The transmittance spectra of mechanically exfoliated **a)** intrinsic few-layer graphene flakes and **b)** $FeCl_3$-intercalated few layer graphene flakes which are $1-5$ layers thick. **c)** Comparative plot of sheet resistance (R_{sq}) as a function of transmittance for various candidate materials which could be used as transparent electrodes in optoelectronic devices. Grey region highlights the range of $R_{sq}(Tr)$ encompassed by all materials apart from $FeCl_3$-FLG. All figures are reproduced with permission.[18]

3.2 Growth of rubrene single crystals

We used a carrier gas-assisted physical vapour transport process[87] to grow structurally pristine single crystals of rubrene for our experiments in Chapter 6. Figure 3.3a shows a schematic of the apparatus used for this process. A resistive heating element was wound around an open-ended quartz tube such that the density of coils gradually reduced along its length. Several smaller quartz tube sections were than placed inside the original tube in order to easily extract crystals at the end of the process. A vial of rubrene powder (*Sigma Aldrich*, 99.99% pure) was then placed in the region with the highest density of coils before purging the tube with a constant flow of Ar gas for 15 minutes. Once purged, a DC voltage was applied to the resistive coil such that the tube region containing rubrene powder was heated to approximately 310^oC. Upon reaching this temperature, the rubrene powder sublimates and flows with the carrier gas down the temperature gradient sketched in Figure 3.3a. For an appropriately shallow temperature gradient, single crystal crystals of rubrene and residual impurities then condense at separate regions of the tube. After three purification cycles whereby rubrene single crystals were returned to the vial position and re-sublimated, highly pure needle and platelet shaped crystals could be synthesised. A photograph of macroscopic platelet and needle crystals is shown in Figure 3.3b. We selected far thinner ($< 1\mu m$) crystals for use in Chapter 6 in order to enable successful lamination onto graphene. These thin crystals are extremely delicate to handle. We used a technique whereby the crystals electrostatically adhere to sharpened cocktail sticks (Figure 3.3c) and could then be positioned on top of graphene films. All growth cycles were performed in dark conditions.

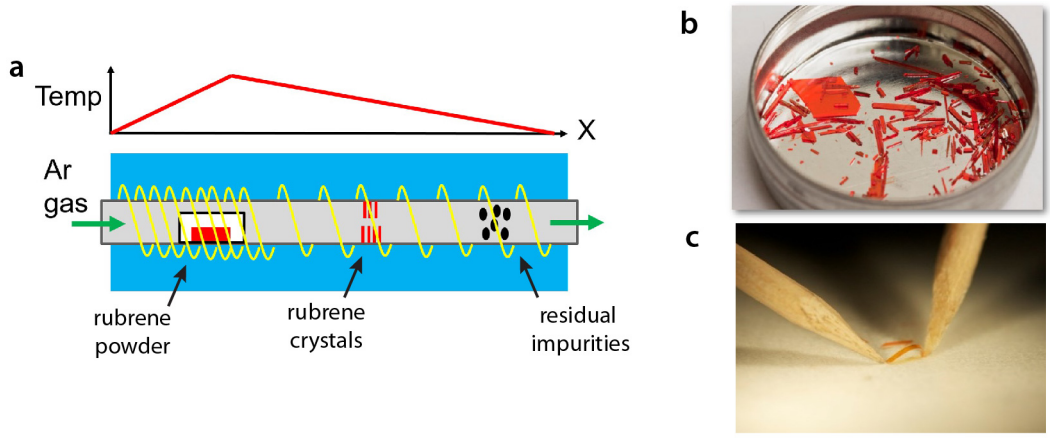

Figure 3.3: Physical vapour transport growth of rubrene single crystals. a) Scematic diagram of the physical vapour transport process used to grow rubrene single crystals and a sketched plot of the temperature gradient along the quartz tube. **b)** Photograph of macroscopic rubrene single crystals grown via physical vapour transport. **c)** Photograph detailing the electrostatic adhesion procedure used to handle rubrene single crystals. Photographs a) and b) are courtesy of Dr. Ana Neves.

3.3 Transfer of graphene films

In Chapter 6, monolayer films of CVD graphene were transferred onto p-doped Si substrates with a 280nm-thick surface layer of SiO_2 using a commonly employed wet transfer technique[88] which uses PMMA as a supportive layer. In this process, 100nm of PMMA is spin coated on top of graphene and the underlying Cu foil is subsequently etched by floating on an ammonium persulfate solution. After thorough rinsing with de-ionised water, the remaining PMMA/graphene film is scooped onto a substrate and allowed to dry before removal of the PMMA top layer with acetone. If large area ($> 100\mu m \times 100\mu m$) continuous graphene films are required, a common problem with this method is ineffective drainage of water from the graphene-SiO_2 interface (shown schematically in Figure 3.4a). This arises due to the beading of water trapped between two hydrophobic surfaces. These beads usually rupture and cause tears in monolayer graphene films during subsequent drying and cleaning procedures (see Figure 3.4b). To mitigate this problem, we pre-treated SiO_2/Si substrates for 5 seconds in a 3:1 solution of de-ionised water:buffered hydrofluoric acid.[89] This acts as a mild etchant of both organic surface residues and SiO_2. The substrate is thoroughly cleaned by this process and a sufficient density of silanol groups are introduced to make the surface hydrophilic but not so many as to create a large concentration of scattering centres which would critically impair the charge carrier mobility in subsequent devices.[90] The effect of this treatment is demonstrated in Figure 3.4c, where the contact

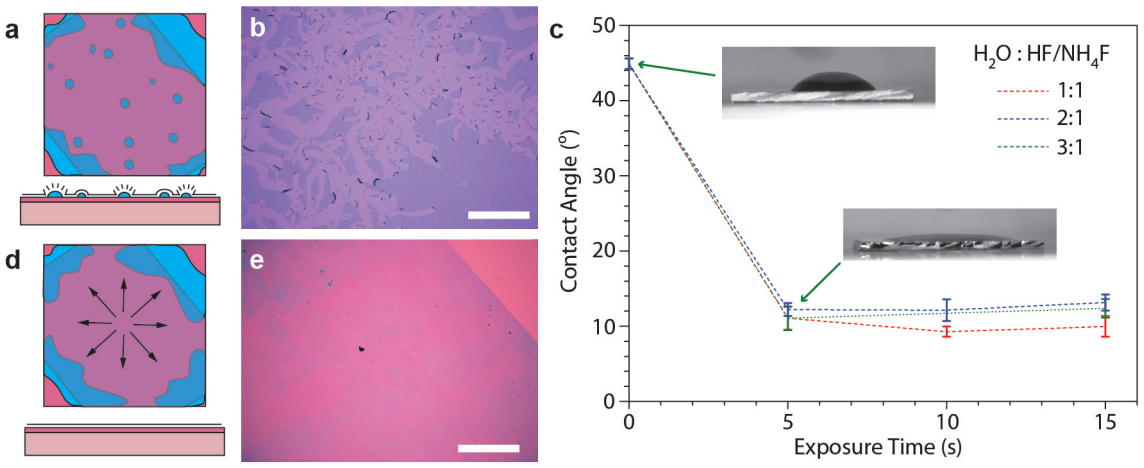

Figure 3.4: A substrate treatment method for improved yields of CVD graphene transferred onto SiO_2/Si. a) Top-view and side-view schematics of water beading underneath transferred graphene films and subsequent perforation during drying. **b)** Micrograph image of a perforated graphene film. **c)** Contact angle of de-ionised water on SiO_2/Si as a function of exposure time to three different concentrations of buffered hydrofluoric acid. Inset: Photographs of de-ionised water droplets on substrates treated and untreated by the 3:1 mixture. A **d)** schematic and **e)** micrograph image show graphene transferred onto a substrate treated by 3:1 H_2O:HF/NH_4F for 5 seconds. Scale bars = $500\mu m$.

angle of de-ionised water on an HF-exposed SiO_2/Si substrate is significantly reduced in comparison to substrates cleaned solely with acetone and isopropanol. By implementing this process, we were able to improve the graphene substrate transfer procedure such that large-area continuous films were attained with a sufficiently high yield (see Figure 3.4d and 3.4e).

3.4 Raman spectroscopy

Raman spectroscopy involves the study of in-elastically scattered light. As we have already discussed, the absorption of a photon with energy hv involves the promotion of an electron to an energy $\Delta E = hv$ higher than its original state. The excited electron may then relax to a lower electronic state some time later via the emission of a photon. This emitted light is said to have been scattered.

The time-varying electric field, $(\mathcal{E}(x, y, z, t))$ of an incident light wave can induce a similarly time-varying polarisation $(\mathcal{P}(x, y, z, t))$, or electric dipole moment, in the molecule/lattice in which light is scattered. The time varying displacement, $q(t)$, of lattice ions/molecules will have a vibrational frequency v_m where $m = (0, 1, 2, 3, ...)$ denotes

harmonic levels of the vibration. The degree of polarisation depends on a constant of proportionality known as the polarizability, $\alpha_{x,y,z}$. This can be expressed in a matrix form as

$$\begin{bmatrix} \mathcal{P}_x \\ \mathcal{P}_y \\ \mathcal{P}_z \end{bmatrix} = \begin{bmatrix} \alpha_{xx} & \alpha_{xy} & \alpha_{xz} \\ \alpha_{yx} & \alpha_{yy} & \alpha_{yz} \\ \alpha_{zx} & \alpha_{zy} & \alpha_{zz} \end{bmatrix} \begin{bmatrix} \mathcal{E}_x \\ \mathcal{E}_y \\ \mathcal{E}_z \end{bmatrix} \tag{3.1}$$

where the 3×3 matrix on the right hand side of Equation (3.1) is the polarizability tensor.[91] Hence the polarisation of incident light can affect which terms in the polarizability tensor are probed. The vast majority of scattered photons ($\sim 99.999\%$) will undergo elastic Rayleigh interactions whereby the emitted photon has the same frequency as incident light. However, if the polarizability of the scattering medium varies with displacement ($(\partial\alpha/\partial q)_0 \neq 0$), the vibrational mode is Raman-active and energy may be exchanged with the excited electron via inelastic Stokes and anti-Stokes processes. Illustrations of Rayleigh, Stokes and anti-Stokes processes are shown in Figure 3.5. For resonant Raman processes, the energy of incident photons correlates with a real excited electronic state. The absence of a band gap in graphene implies that all photon wavelengths can induce resonant Raman processes. The wavenumber of in-elastically scattered light will differ from the wavenumber of the incident photon by

$$\Delta\omega = \left(\frac{1}{\lambda'} - \frac{1}{\lambda_0}\right) \tag{3.2}$$

where λ' and λ_0 are incident and scattered photon wavelengths respectively. This difference in wavenumber, known as the 'Raman shift', will vary according to the frequency of the phonon mode which light has coupled to. Hence, if a sample is illuminated with monochromatic light and an appropriate notch filter is used to absorb signals from Rayleigh processes, inelastically-scattered light can be analysed with a spectrometer and will reveal information regarding the vibrational modes and structure of the sample.

In Figures 3.5b-d, sketched band diagrams illustrate the Stokes processes which are relevant to the Raman spectrum of monolayer graphene (shown in Figure 3.5e). The G peak centred around $\Delta\omega \approx 1585cm^{-1}$ in Figure 3.5e corresponds to the transition shown in Figure 3.5b and is activated by the E_{2g} vibrational mode shown in Figure 3.5f. The intensity of the G peak increases with the number of graphene layers[92] and its position can be altered by changes in strain[93] or charge carrier concentration.[94,95] The D peak, positioned around $\Delta\omega \approx 1350cm^{-1}$, is a two phonon scattering process (Figure 3.6c) which involves the 'breathing mode' vibration sketched in Figure 3.6g. This mode is only Raman active in proximity to a lattice defect such as a missing carbon atom. As a

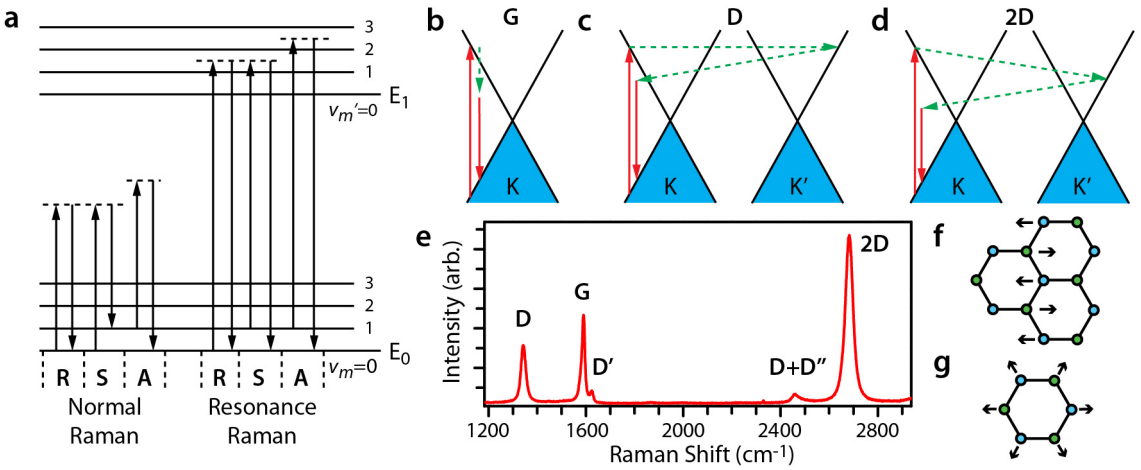

Figure 3.5: Raman spectroscopy of monolayer graphene. a). Illustration of normal and resonant Rayleigh (R), Stokes (S) and anti-Stokes (A) scattering processes in a diatomic molecule. Band diagrams of the inelastic scattering processes in graphene which correlate to the **b)** G, **c)** D and **d)** 2D Raman peaks. Green dashed arrows indicate scattering with a phonon. **e)** Raman spectrum of disordered monolayer graphene. Diagrams of the graphene lattice vibrations corresponding to the **f)** E_{2G} phonon mode and **b)** breathing modes in proximity to a lattice defect.

result, the intensity of the D peak provides a metric for the level of structural disorder in graphene samples.[96] The $2D$ peak, positioned at $\Delta\omega \approx 2680cm^{-1}$ is a second order process of the D peak, meaning that an electron is scattered with two phonons of equal and opposite momentum such that no defect-related breathing mode is required for its activation. The main feature of the 2D peak is that it becomes degenerate, splitting into multiple overlapping Lorentzian peaks in few-layer graphene samples. Hence, the $2D$ peak is most useful as an indicator of the number of layers within a few-layer graphene sample.[97] Overall, careful analysis of the G, D and $2D$ Raman peaks provides a quick and non-invasive method of assessing the doping, structural disorder and layer number of graphene samples. As a result, we employ this method throughout Chapters 4-6 of this thesis. As an attempt to keep our discussions of Raman spectra concise, we will refer to the position, full-width half maximum and area of a Raman peak (the G peak in this example) as $Pos(G)$, $FWHM(G)$ and $A(G)$.

As a final note on Raman spectroscopy, we will briefly review the effects of $FeCl_3$ intercalation on the Raman spectrum of few-layer graphene. Figure 3.6a shows a plot that has been reproduced from the work of Lazzeri et. al.,[94] in which they developed a theoretical model to describe the shift in $Pos(G)$ as a function of charge carrier concentration in monolayer graphene. Crucially, it was found that the experimentally-measured change in frequency of the E_{2g} phonon mode during gate voltage sweeps of graphene FETs[95] cannot

be described whilst assuming that electrons fully equilibrate around vibrating lattice ions (i.e. the Born-Oppenheimer approximation is invalid).[98] Instead, the solid line in Figure 3.6a represents a theoretical model which accounts for dynamic changes in the screening of lattice ions by charge carriers at low levels of doping in monolayer graphene. Typically, it would not be valid to directly apply this model to the case of few-layer graphene. The π and π^* bands of adjacent layers overlap significantly in few-layer graphene so the hopping of electrons between lattice ions on neighbouring layers must be considered when solving the Schrödinger equation. The resultant energy band structure of few-layer graphene is quite different from the case of monolayer graphene, with a complex mixture of overlapping parabolic and linear sub-bands at K rather than the simple linear band structure shown in Figure 2.2b.[45] As a result, the theoretical calculations of Lazzeri et. al.[94] which assume the density of states of monolayer graphene (Equation 2.7) will not accurately describe electron-phonon interactions in few-layer samples. An important exception to this argument is shown in Figures 3.6b and 3.6c, which plot the Raman spectra of pristine and $FeCl_3$-intercalated few-layer graphene respectively. Following intercalation, the degenerate $2D$ peaks shown in Figure 3.6b change to form a symmetric profie which can be fit well with a single Lorentzian distribution. In contrast, the position of the G band is found blue-shift to higher wavenumbers, between $1600cm^{-1}$ and $1625cm^{-1}$, and splits into two distinct peaks. These peaks, denoted G_1 and G_2, are representative of stage-2 and stage-1 intercalation respectively.[18,99] Combined with the fact that electron diffraction patterns show the interlayer spacing of graphene layers to triple following $FeCl_3$-intercalation,[100] the Raman spectra shown in Figure 3.6c indicate that graphene layers in $FeCl_3$-FLG are electrically de-coupled from one another and can be considered as a stack of parallel, highly-doped monolayers.[18,99] The position of each split G peak in Figure 3.6c may therefore be numerically evaluated using the dynamic model in Figure 3.6c to correlate betweeen $Pos(G)$ and the carrier concentration within a single constituent graphene layer of the $FeCl_3$-FLG flake. We utilise this method in Chapters 4 and 5 of this thesis, where peaks denoted G_0, G_1 and G_2 denote a graphene layer with 0, 1 and 2 adjacent layers of $FeCl_3$ respectively. In terms of the staging nomenclature defined in Figure 3.1b, G_1 and G_2 peaks correspond to stage-2 and stage-1 intercalation of a graphene layer respectively.

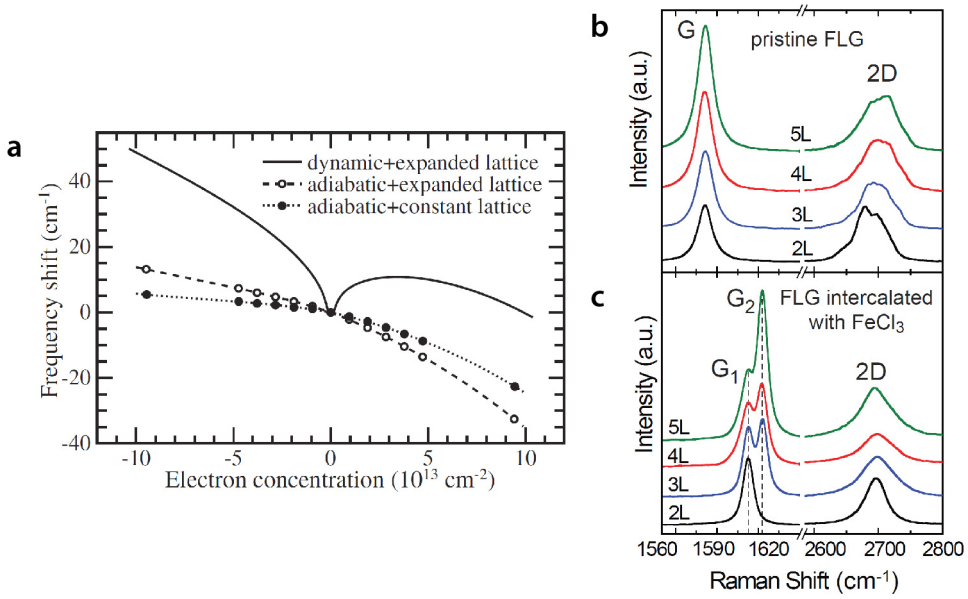

Figure 3.6: Raman spectroscopy of doped graphene. a) Theoretical shift in position of the G band of graphene as a function of electron concentration. Negative values on the x-axis denote values of hole concentration. Dashed lines assume the Born-Oppenheimer approximation of an equilibrium distribution of electrons about the lattice ions with (open circles) and without (filled circles) changing lattice constants. Solid line assumes a changing lattice constant and non-equilibrium distribution of electrons. **b)** Stacked Raman spectra of few layer graphene. The degeneracy of the 2D peak increases with the number of graphene layers. **c)** Stacked Raman spectra of $FeCl_3$-intercalated few-layer graphene. a),[94] b)[18] and c)[18] are reproduced with permission.

4

Large Area $FeCl_3$-intercalated graphene electrodes

1 2

[1]Some of the findings presented in this chapter have been published in the following articles:
Large-area functionalized CVD graphene for work function matched transparent electrodes, T. H. Bointon, **G. F. Jones**, A. de Sanctis, R. Hill-Pearce, M. F. Craciun and S. Russo, *Scientific Reports* **5**, 16464 (2015).
Homogeneously Bright, Flexible, and Foldable Lighting Devices with Functionalized Graphene Electrodes, E. Torres Alonso, G. Karkera, **G. F. Jones**, M. F. Craciun, and S. Russo, *ACS Applied Materials & Interfaces*, **8**, 16541-16545 (2016).

[2]Dr. Liping Lu recorded the PLED efficiency measurements presented in this chapter. Pictures of ACEL devices presented in this chapter were taken by Elías Torres Alonso. Matthew D. Barnes assisted with the etching and transfer of large-area $FeCl_3$-FLG films . Gareth F. Jones made significant contributions to all aspects of this project including (but not limited to) device fabrication, design/construction of apparatus, electronic transport and spectroscopy measurements, analysis/interpretation of all data and the writing of all associated manuscripts.

4.1 Introduction

As discussed in Section 3.1.2, the sheet resistance and optical transparency of mechanically exfoliated flakes of few-layer graphene intercalated with $FeCl_3$ ($FeCl_3$-FLG) is comparable to that of indium tin oxide (ITO), a material used as a transparent electrode in many optoelectronic devices. Naturally, the next logical step for research efforts is to test the performance of devices, such as LEDs and solar cells, in which ITO is replaced with $FeCl_3$-FLG as the transparent electrode. Flexible optoelectronic devices are particularly relevant for such studies because ITO is a highly brittle material[7] and it has a high energy cost of production in comparison to organic polymers.[101] However, the mechanical exfoliation of few-layer graphene flakes with scotch tape is not an industrially scalable method for producing large-area, transparent graphene electrodes. To this end, in this chapter we develop a method of up-scaling the production of $FeCl_3$-FLG to macroscopic, continuous films and embed them, for the first time, into light-emitting devices. We use the non-invasive method of Raman spectroscopy as a fast and simple way to assess the quality of $FeCl_3$-intercalation in these films and identify inhomogeneous grain density as a cause of spatial variations in sheet resistance and optical transmittance in the visible range. Overall, we are able to produce large-area, transparent electrodes with sheet resistance and transmittance to visible light of $R_{sq} = 100\Omega/sq$ and $Tr = 70\%$ respectively and demonstrate their functionality in AC electroluminescent devices and polymer light-emitting diodes.

4.2 Experimental Details

Device fabrication

As a starting material, we used CVD few-layer graphene grown on nickel. This was purchased from a commercial supplier (*Graphene Supermarket*) and was grown via the dissolution, segregation and precipitation of carbon from methane gas in a sputtered thin film of Nickel.[88] Thin films sputtered onto 4-inch diameter SiO_2/Si wafers were used instead of thicker free-standing foils in order to avoid excess dissolution of carbon into Ni, which is highly carbon soluble. This promoted the growth of few-layer graphene films rather than bulk graphite. Figure 4.1a details the layered structure of these wafers. Before intercalation with $FeCl_3$, the few-layer graphene film was removed from the underlying substrate and transferred onto glass, quartz, or SiO_2/Si. For small samples ($\leq 1cm^2$) this process is trivial and can be completed by the $FeCl_3$ etching and scoop-transfer process discussed in Section3.3. For samples as large as the 6cm×6cm scribed wafer shown in Figure 4.1b

however, this procedure is far more delicate and a freely floating PMMA/graphene film is extremely likely to rupture under the weight of the substrate halfway through etching. The transfer of PMMA/graphene films onto substrates by hand also becomes un-feasible, with tears and cracks inevitably occurring due to physical stress of the film during lamination. To overcome these problems, we built a system to automate the etching and transfer of graphene, shown in Figure 4.1c. This process eliminated the need to to physically disturb large-area PMMA/graphene films during etching and transfer. In this system, the as-grown few-layer graphene film sits in a large basin on a sloped wedge and is kept centred by a surrounding polypropylene frame (shown in Figure 4.1d). The basin is filled with 1 molar $FeCl_3$ in de-ionised water using peristaltic pumps at a rate calibrated to etch the underlying nickel whilst not stressing or cracking the PMMA/few-layer graphene film. The floating PMMA/graphene film is then held in place by the polypropylene frame whilst de-ionised water is pumped into the basin, diluting the $FeCl_3$, and overflowing out to an external reservoir. Once sufficiently cleaned, the SiO_2/Si wafer used for CVD growth is replaced with a new substrate on the wedge underneath PMMA/graphene and de-ionised water is pumped out allowing graphene to be steadily re-laminated without cracks, folds or bubbles forming. Figures 4.1e-i show snapshots taken from a time-lapse video of this process.

After drying the transferred samples at 60^oC and removing the PMMA support layer with acetone and IPA, large-area few-layer graphene samples were intercalated with $FeCl_3$ using the procedure outlined in Section 3.1.2 with an initial two hour bake-out phase at 100^oC (Figure 4.1) The intended purpose of this additional step was to de-hydrate the $FeCl_3$ powder and remove residual water vapour away from the central furnace zones, which otherwise causes an increase in pressure up to $10^{-1}mbar$ within the first minute after sealing the vacuum pump line (see Figure 4.1k). Based on observations of samples produced over many intercalation cycles, we found that the removal of moisture also limits condensation of $FeCl_3$ residues on the surface of graphene, which can otherwise only be partially removed with organic solvents (Figures 4.1l-m). A photograph of a typical $FeCl_3$-FLG film on glass is shown in Figure 4.1n with the right edge of the substrate exposed for comparison. Upon careful examination, randomly distributed 'holes' with diameters ranging between $50\mu m$ and $500\mu m$ are found across the film. Micrograph images of similar films transferred onto SiO_2/Si (Figure 4.1o) show that these 'holes' are, in fact, continuous regions of few-layer graphene where an alternate rate of carbon precipitation from nickel has produced a comparatively low grain density consisting of dispersed islands connected by a continuous bilayer film. Each island is approximately $10\mu m$-wide and consists of more than 10 graphene layers (Figure 4.1p). On the other hand, the visibly darker surrounding

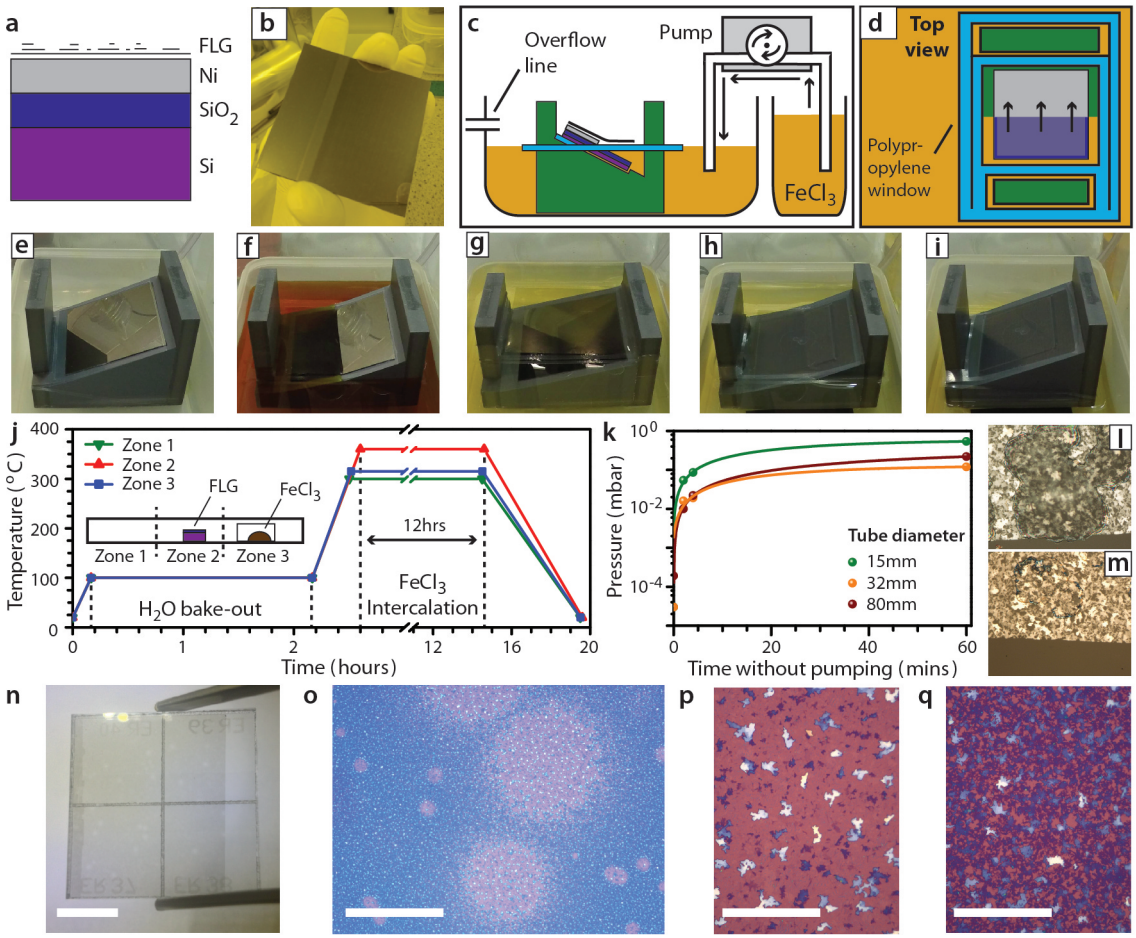

Figure 4.1: Fabrication of large area $FeCl_3$-intercalted few-layer graphene films. **a)** Schematic of the layer structure of CVD graphene grown on sputtered Ni films. **b)** Photograph of a scribed CVD graphene wafer with a PMMA surface layer before undergoing the etching and transfer procedure detailed in **c)-d)** schematics and **e)-i)** time-lapse photos. **j)** Plot of the transient temperature in each furnace zone (*inset*) during a modified version of the $FeCl_3$ intercalation process. **k)** The increase in pressure over time after sealing tubes of various diameter prior to a bake-out. Micrograph images show $FeCl_3$ surface residues **l)** before and **m** after cleaning with IPA. **n)** Photograph of a $FeCl_3$-FLG film on glass. Scale bar: 1cm. Micrograph images of $FeCl_3$-FLG on SiO_2/Si show **o)** the variation in grain density across a film (scale bar: $500\mu m$) and magnified pictures of **p)** low and **q)** high density regions (scale bars: 50μm).

regions of the film are comprised of a higher density of few-layer (≤ 9 layer) islands (Figure 4.1q). On average, these islands are approximately $4\mu m$-wide and are distributed across the same bilayer film. All layer numbers are approximate and based upon optical contrast measurements.[47]

Methods

All Raman spectra, apart from Figures 4.3a and 4.3d were excited with a 514nm wavelength laser focused to a diffraction-limited spot diameter of $320nm$ and incident power of $4mW$. The other spectra were recorded using a $532nm$ wavelength laser under similar conditions. Black pixels in the Raman maps of Figures 4.3 and 4.4 represent masked positions, where the total area of all fitted peaks fell below 5% of the maximum recorded value. This was a threshold imposed in our analysis designed to avoid the spurious fitting of peaks to background noise. For the transmittance map in Figure 4.2f, emission from an incandescent bulb was focused by a condenser lens ($NA = 0.3$) through our sample and collected by a $50\times$ microscope objective ($NA = 0.8$). Four-terminal sheet resistance measurements were recorded in AC using a lock-in amplifier in constant rms current configuration. The ACEL devices in Figures 4.5a-d were fabricated by either spin coating or screen printing successive layers of ZnS:Cu ($30\mu m$), $BaTiO_2$ ($25\mu m$) and Ag paste ($> 20\mu m$) onto $FeCl_3$-FLG on glass/PET and drying on a hot plate at 130^oC after each step. Electroluminescence was imaged under an applied AC voltage of $V_{AC} < 180V$ at $681Hz$. Transfer of $FeCl_3$-FLG films from SiO_2/Si substrates into onto PET was achieved using thermal release tape (*Graphene Supermarket*) as a supportive layer.[102]

4.3 Results

4.3.1 Characterising $FeCl_3$-FLG electrodes

Given the significant variation in grain density and layer number across macroscopic CVD films of $FeCl_3$-FLG, we considered it important to establish whether any similar spatial variation in intercalation staging was also present. Direct electrical measurements of the Hall voltage across a multitude of individual $FeCl_3$-FLG grains would be a cumbersome approach to establish the degree of p-doping and charge carrier concentration across these films. Therefore, we adopted Raman spectroscopy, which is a fast and non-invasive method. In Figure 4.2a, we plot Raman spectra that were recorded at four separate positions across a $100\mu m \times 100\mu m$ area of $FeCl_3$-FLG on SiO_2/Si. These spectra are representative of the maximum variation in intercalation staging observed across these

CVD-grown films. Focusing on the G-band region in each case, we fit three Lorentzian peaks to each Raman spectra, representing the G_0, G_1 and G_2 modes introduced in Section 3.4. From this, it follows that the relative area of each of these peaks is indicative of the proportion of non-intercalated, stage-2 intercalated and stage-1 intercalated graphene layers at each location respectively. In practice, individual comparison of the area and position of all three peaks at every scanned location of a mapped area becomes difficult to interpret. Instead, we considered the area-weighted average G peak position, $\langle Pos(G)\rangle$, as a single term which empirically describes the general degree of intercalation for all graphene layers at each measured location.

$$\langle Pos(G)\rangle = \frac{Pos(G_0)A(G_0)/2 + Pos(G_1)A(G_1) + Pos(G_1)A(G_0)}{A(G_0)/2 + A(G_1) + A(G_2)} \tag{4.1}$$

In Equation (4.1), the weighting of $A(G_0)$ has been skewed to compensate for a narrowing of the G-band by a factor of two when its position is blue-shifted past $\sim 1587cm^{-1}$.[95,98] This is due to the Pauli exclusion principle blocking the main mechanism of linewidth broadening for the E_{2g} phonon mode, decay into an electron-hole pair, when the Fermi level of graphene is shifted away from the charge neutrality point. We also considered the approximately four-fold enhancement in $I(G)$ reported from measurements of graphene at high levels of charge carrier concentration using ionic polymer gating.[103] This effect also arises from the Pauli exclusion principle, where non-resonant Raman pathways are screened out when the Fermi level is lowered enough to approach the ground state of resonant Raman transitions. The onset of this effect is dependent upon the excitation wavelength used and, in our case, should have a negligible effect across the wavenumber range of the G_0, G_1 and G_2 peaks. In Figure 4.2a, inset values of $\langle Pos(G)\rangle$ were calculated from each representative Raman spectra and serve as references when interpreting scanning maps which we will now discuss. Figure 4.2b shows a micrograph image of a $225\mu m^2$ region of $FeCl_3$-FLG with a high density of grains. Using interval steps of just $500nm$, we traced a rasterised scan across this entire region and analysed the Raman spectra recorded at each point using Equation (4.1). A high-resolution map of $\langle Pos(G)\rangle$ over this area is shown in Figure 4.2c. Colour bar scales are consistent across all $\langle Pos(G)\rangle$ maps in this chapter, with the orange/purple/blue ranges indicative of Raman spectra dominated by the $G_0/G_1/G_2$ peak respectively. Comparing Figures 4.2b and 4.2c, regions that display significant stage-2 intercalation loosely correlate with the positions of the thickest few-layer graphene grains. Intuitively this makes sense, given that intercalation is initiated by diffusion of $FeCl_3$ vapour in from the edge planes of graphene stacks.[85] It is therefore reasonable to expect that thicker grains, with a larger fraction of layer edges exposed above the base bilayer, will undergo a higher degree of intercalation.

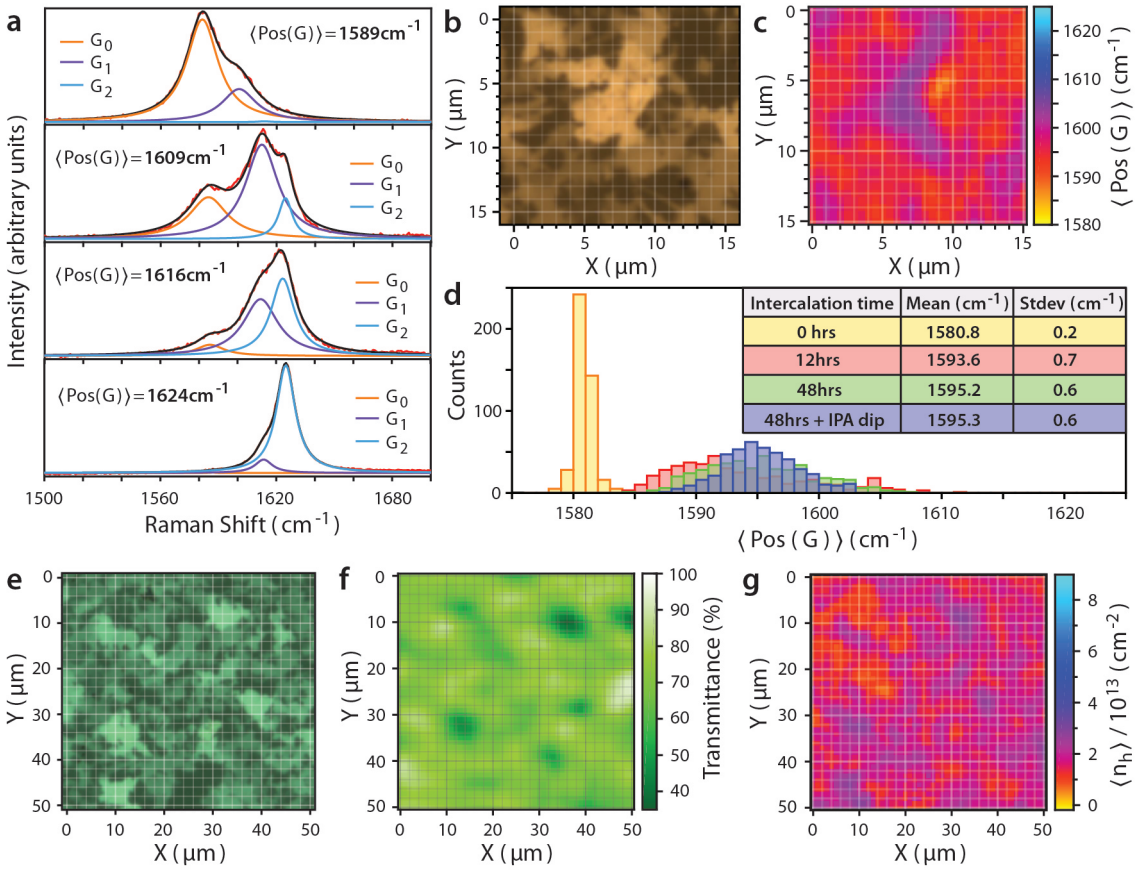

Figure 4.2: Carrier concentration and transmittance of large-area FeCl$_3$-FLG films. a) Stacked Raman spectra representative of varying degrees of $FeCl_3$ intercalation present across a CVD few-layer graphene film. The area-weighted average G peak position is provided for each case. **b)** Micrograph image and **c)** high resolution Raman map of a $15\mu m \times 15\mu m$ region of $FeCl_3$-FLG on glass. **d)** Histograms showing repeat measurements of the area-weighted average G peak position across a $100\mu m \times 100\mu m$ $FeCl_3$-FLG region after each stage of two successive 12-hour intercalation cycles and subsequent immersion in isopropanol. **Inset:** Compiled values of the mean and standard deviation for each distribution. **e)** Micrograph image of a $50\mu m \times 50\mu m$ region of $FeCl_3$ on glass, across which scanning maps of **f)** transmittance ($\lambda = 550nm$) and **g)** estimates of the average hole concentration per graphene layer were recorded.

In order to ascertain whether a longer period of exposure to $FeCl_3$ vapour or exposure to organic solvents affects the staging of intercalation across these large-area films, we recorded Raman maps over a $100\mu m \times 100\mu m$ area of another $FeCl_3$-FLG sample after four successive fabrication steps: lamination onto a glass substrate; a 12 hour intercalation cycle; a second 12 hour intercalation cycle; and immersion in isopropyl alcohol (60^oC for 30 seconds). The results from each stage of this process are compiled in a histogram in Figure 4.2d, where the value of $\langle Pos(G) \rangle$ measured at each map position is binned into $1cm^{-1}$ intervals. Minor variations in doping, likely due to surface adsorption of moisture, create a narrow distribution centred at $1581cm^{-1}$ before intercalation. In contrast, the distribution after 12 hours exposure to $FeCl_3$ vapour shows a far wider variation in doping and up-shifts to a mean value of $\sim 1594cm^{-1}$. With the $\langle Pos(G) \rangle$ distribution largely unchanged after an additional 12 hour intercalation cycle, we find no evidence to suggest that slow kinetic processes of $FeCl_3$ vapour are limiting the degree of doping induced in our samples. Further systematic alterations to variables such as zone temperature and vapour pressure could produce stage-1 intercalation of the kind shown in the bottom plot of Figure 4.2a, and would need further investigation. Finally, the absence of de-intercalation after treatment with IPA provides preliminary evidence that, once fabricated, CVD $FeCl_3$-FLG films are found to be as environmentally stable as mechanically exfoliated flakes.

As a next step in characterising large area CVD $FeCl_3$-FLG films, we assessed the electronic and optical properties of different grains. Figure 4.2e shows a micrograph image of a high grain density region laminated on glass, over which we have recorded complimentary scanning measurements of transmittance ($\lambda = 550nm$) and charge carrier concentration. The transmittance map shown in Figure 4.2f reveals a mean of $Tr = (70 \pm 2)\%$ over the entire area, with dips/peaks of $Tr \approx 50\%/94\%$ across the thickest/thinnest grains respectively. The map shown in Figure 4.2g shows the estimated average charge carrier concentration per graphene layer. This was established by numerically evaluating measured values of $\langle Pos(G) \rangle$ across the mapped region with the non-adiabatic model of phonon mode stiffening, shown in Figure 3.6a of Section 3.4, which accurately relates the E_{2g} mode wavenumber to the charge carrier concentration in a single graphene layer. The adjusted colour bar scale in Figure 4.2g reflects the non-linear relation between Raman shift and charge carrier concentration. Whilst the thickest grains are indeed the most strongly doped, $\langle n_h \rangle \approx 2.8 \times 10^{13} cm^{-2}$, the few-layer grains which cover the majority of the $FeCl_3$-FLG film also exhibit extremely high charge carrier concentrations of approximately $2 \times 10^{13} cm^{-2}$ per layer. As a result, we estimate the mean charge carrier concentration over the entire high grain density region of $FeCl_3$-FLG to be $(1.8 \pm 0.2) \times 10^{13} cm^{-2}$ per layer.

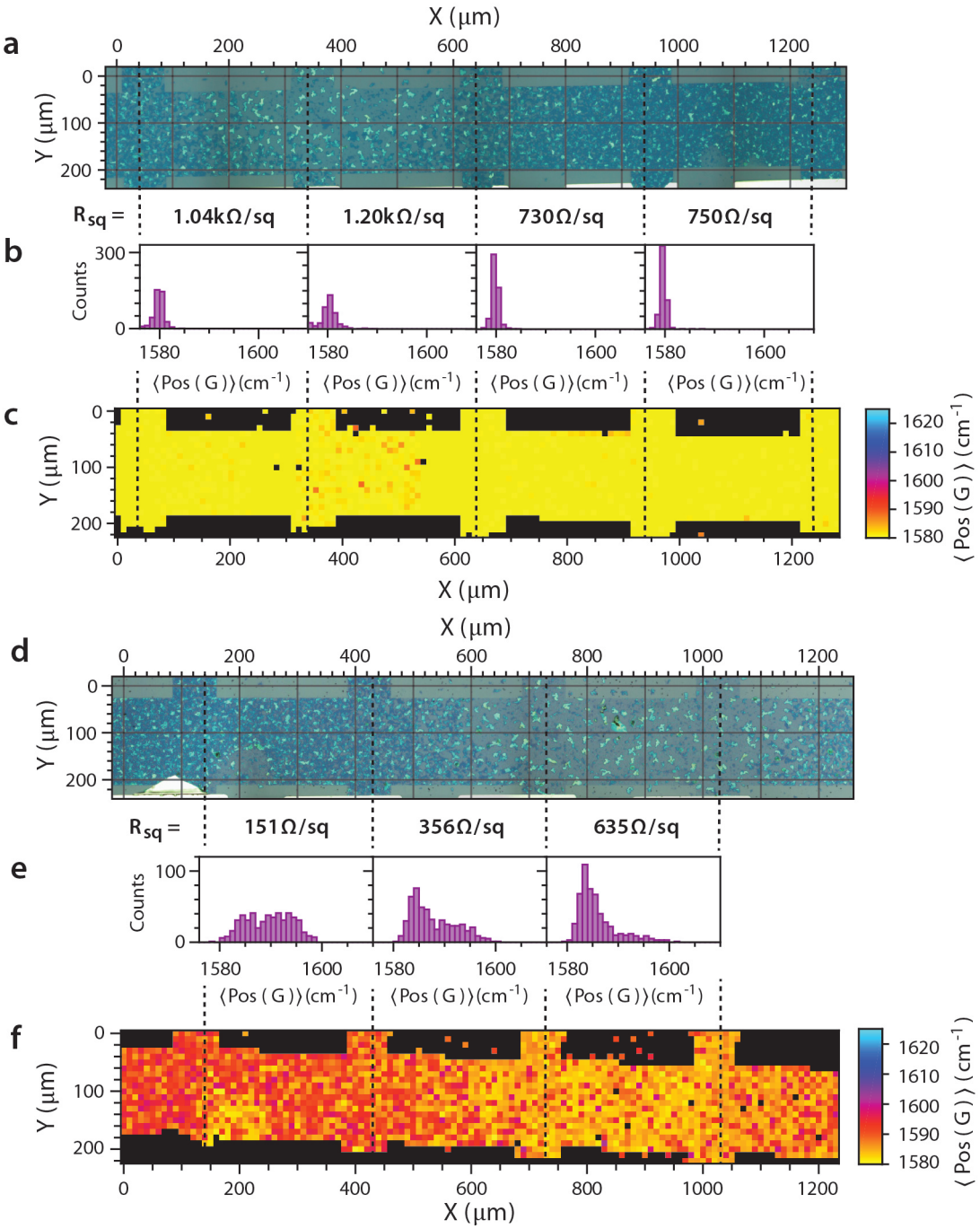

Figure 4.3: The influence of grain density on sheet resistance in FeCl$_3$-FLG films. a) Micrograph image of a Hall bar consisting of pristine few-layer graphene. Values of four terminal sheet resistance are listed between the voltage probes where they were measured. **b)** Histograms of the area-weighted average G peak position taken from **c)** a Raman map of the entire device are plotted for region enclosed between a pair of voltage probes (dashed lines). **d)-f)** Figures equivalent to a)-c) for an Hall bar intercalated with FeCl$_3$ for 12 hours.

Having established the transparency and charge carrier concentration of/within microscopic grain regions of CVD $FeCl_3$-FLG films, we investigated whether macroscopic variations in grain density, imaged in Figures 4.1n-q, influence the sheet resistance of resulting electrodes. To do this, we fabricated multiple Hall bars of CVD few-layer graphene laminated onto SiO_2/Si with channels defined using optical lithography and O_2 plasma etching. 5nm/50nm of Cr/Au was thermally evaporated onto selected regions of the etched film to serve as voltage probes and source/drain electrodes. A micrograph image of such a device is shown in Figure 4.3a. The four terminal resistance of each $300\mu m \times 150\mu m$ channel segment was measured in ambient conditions. Calculated values of sheet resistance are provided below each channel segment. Examining the micrograph, we can see that the highest sheet resistance, about $1.20k\Omega/sq$, corresponds to the channel segment which probes a region of low grain density. Successively lower sheet resistance was measured across channels containing less of these sparse regions, with a minimum of about $730\Omega/sq$ recorded in the centre-right segment made entirely of few-layer graphene with a high grain density. This difference can be explained by the presence of continuous percolation pathways for the electrical current through the more conductive few-layer grains. Histograms of $\langle Pos(G)\rangle$ in each segment (Figure 4.3b) and a Raman map of the entire Hall bar (Figure 4.3c) show almost no variation in doping before intercalation, supporting our claim that variations in R_{sq} are due to differences in grain density and average layer number.

Figure 4.3d shows the micrograph image of an equivalent few-layer CVD graphene device that has undergone 12 hours of $FeCl_3$ intercalation. Similar to the pristine sample, variations in sheet resistance are apparent across the Hall bar channel with a maximum, $R_{sq} \approx 635\Omega/sq$, measured across the rightmost section where the grain density is low. However, significant macroscopic variations in doping are present after intercalation with $FeCl_3$. Evidence of this can be seen from the inconsistent $\langle Pos(G)\rangle$ distributions in Figure 4.3e and non-uniform $\langle Pos(G)\rangle$ map in Figure 4.3f. Areas with poor doping levels directly correlate with the more resistive regions of low grain density, suggesting that $FeCl_3$ vapour does not effectively diffuse between the base bilayer graphene sheets. In contrast, an intercalated Hall bar consisting entirely of a few-layer graphene film with high grain density (Figures 4.4a-c) exhibited consistently low sheet resistance of $R_{sq} \approx 100\Omega/sq$ across all measured segments. Compared to the pristine few-layer graphene film in Figure 4.3d, this represents a seven-fold improvement in R_{sq} across high grain density regions once stage-2 intercalation is achieved. The results of all electrical measurements conducted across few-layer graphene Hall bars are compiled in Figure 4.4d, where sheet resistance is plotted as a function of $\langle Pos(G)\rangle$, which appears to serve as an effective empirical gauge of sheet

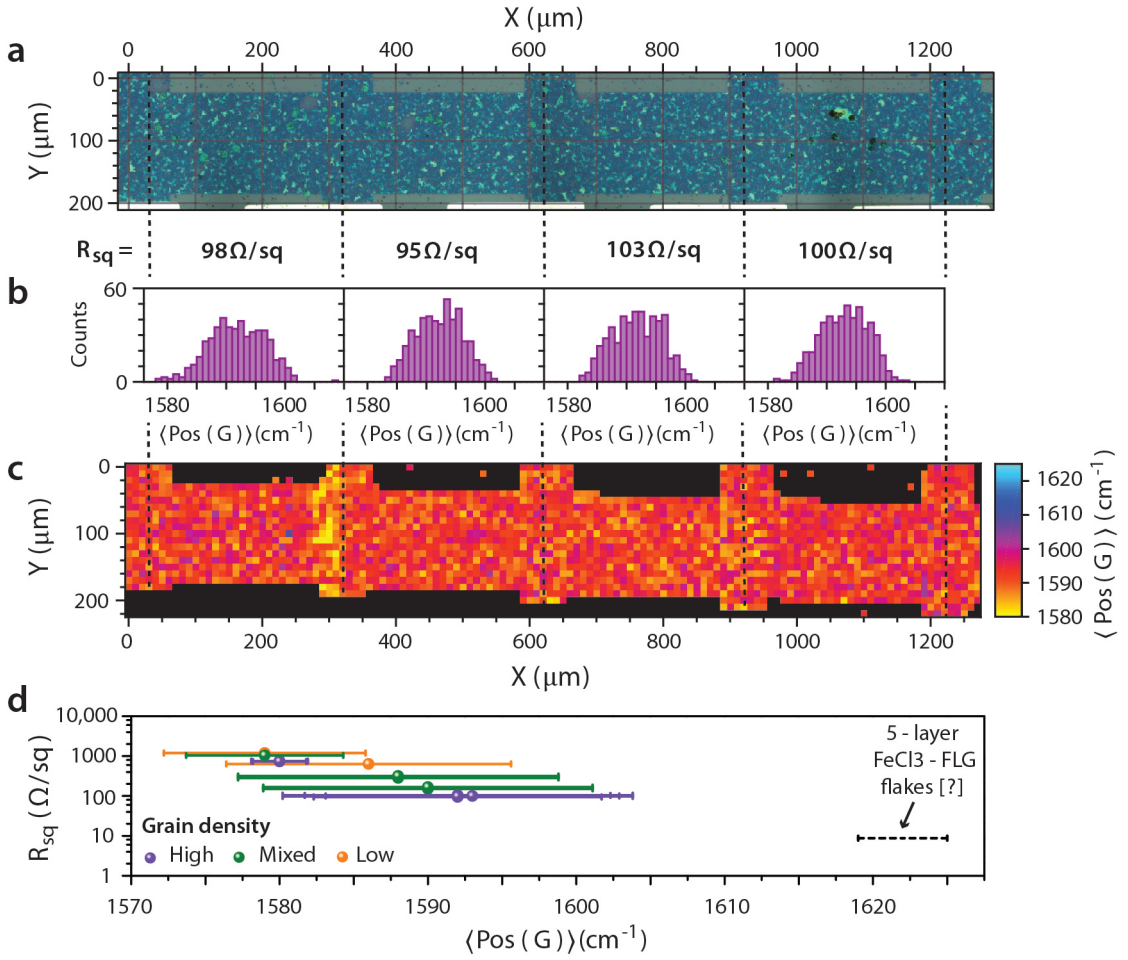

Figure 4.4: The influence of grain density on sheet resistance in FeCl$_3$-FLG films (continued). a) Micrograph image of a CVD few-layer graphene Hall bar with high grain density. Black dashes separate channel segments over which the four-terminal sheet resistance was measured (listed below). **b)** Statistical distribution of $\langle Pos(G) \rangle$ over each of the four segments. Values were obatined from **c)** a scanning Raman of the entire sample. **d)** Plot compiling data from all complimentary resistivity and Raman spectroscopy measurements conducted on FeCL$_3$-FLG films at various stages of intercalation. Legend: Qualitative labels of the grain density within each channel segment.

resistance by means of a non-invasive measurement. The black dashed line, included for reference, represents the record-low sheet resistance reported for a predominantly stage-1 intercalated five layer graphene flake.[18] Clearly, there is a disparity in the intercalation staging that we are currently able to achieve in large-area $FeCl_3$-FLG films compared to the mechanically exfoliated flakes which have been investigated previously by our research group.[18] This results in a typically higher sheet resistance, $R_{sq} \approx 100\Omega/sq$ compared to $Rs \approx 9\Omega/sq$, when up-scaling production of this material for practical device applications. We have focused on the reproducible average transmittance and sheet resistance values of CVD $FeCl_3$-FLG in this chapter, but we also note that outlier samples have been fabricated that exhibit considerably improved metrics of $R_{sq} \approx 20.5\Omega/sq$ and $Tr \approx 77\%$ at $550nm$.[102] A more refined control of parameters such as atmospheric humidity needs to be investigated to attain a uniform stage 1 intercalation. Nevertheless, the fact that higher stages of intercalation have been achieved sporadically gives reason for us to persevere in the development of this material as transparent electrode in optoelectronic devices.

Although processes related to the fabrication of CVD $FeCl_3$-FLG electrodes can still be improved, the work undertaken in this chapter presents the first ever example of successful up-scaling of intercalated few-layer graphene to a size which can be utilised as a transparent electrode in technologically-relevant proof-of-concept samples for electronic industries. Furthermore, values of $R_{sq} \approx (100 - 25)\Omega/sq$ and $Tr(\lambda = 550nm) \approx (70 - 77)\%$ are certainly adequate for this novel material to be implemented into proof-of-concept optoelectronic devices.

4.3.2 $FeCl_3$-FLG electrodes in light-emitting devices

The first examples of such devices are demonstrated in Figure 4.5, where we have substituted the conventional indium tin oxide electrodes in alternating current electroluminescent (ACEL) devices[104] and inverted structure polymer light emitting diodes (PLEDs) with CVD $FeCl_3$-FLG on either glass or PET substrates. Figure 4.5a illustrates the layered structure of an ACEL device, in which particles of zinc sulphide doped with metal ions are suspended in a dielectric resin to form the active layer, see Figure 4.5b. A high-k dielectric of $BaTiO_2$ (*Dupont Luxprint 8153*, $\epsilon_{BaTiO_3} \approx 35$) serves as a buffer layer to prevent short circuits between a back electrode of Ag paste and the transparent $FeCl_3$-FLG front electrode. A band diagram of the operating mechanism within the phosphor particles is shown in Figure 4.5c.[105] Under sufficiently large applied electric fields, electrons occupying shallow interface trap states tunnel into the conduction band of ZnS and continue to accelerate under the potential gradient. Impact excitation then occurs when these charge carriers scatter at luminescent centres localised within the bandgap. Energy

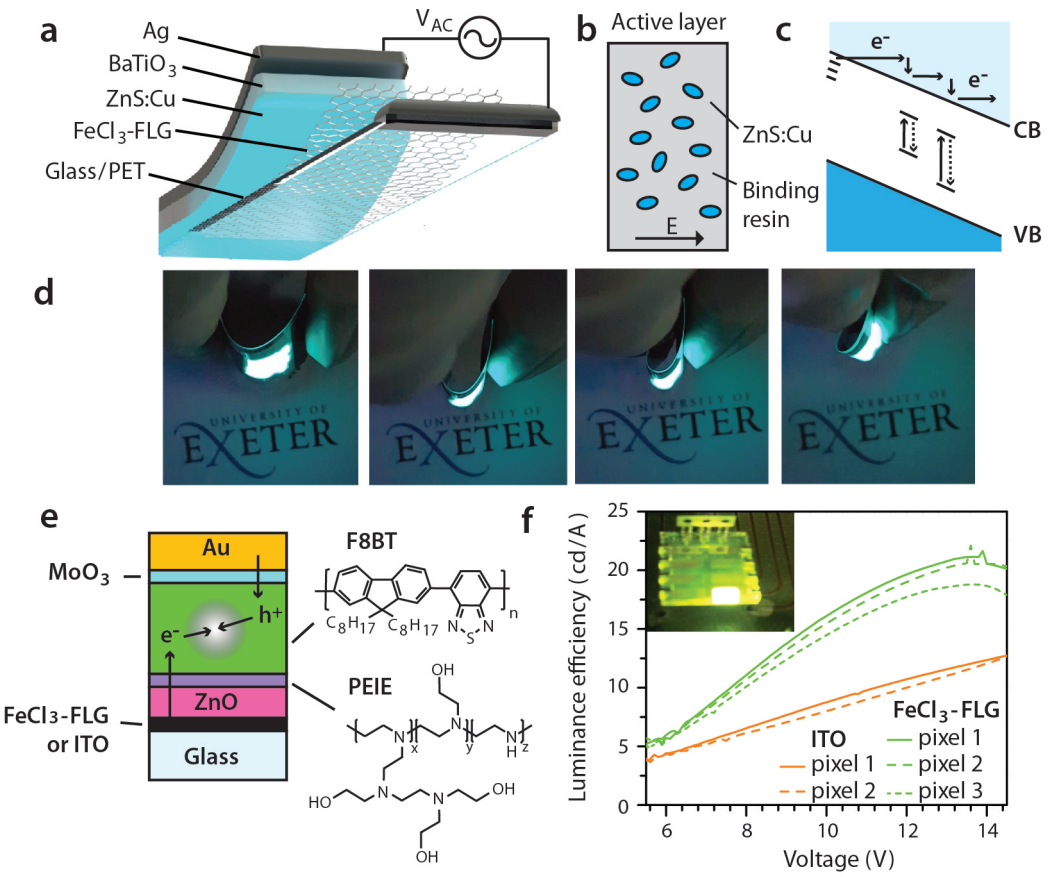

Figure 4.5: Light emitting devices with FeCl$_3$-FLG electrodes. a). Schematic layer structure and circuit diagram of an alternating current electroluminescent (ACEL) device. Exploded layer structure is for visualisation purposes only. **b)** Schematic of the active layer in an ACEL device, where doped ZnS phosphor particles are suspended in a binding resin. **c)** Band diagram of the impact excitation process at luminescent centres in ZnS:Cu under high electric fields. **d)** Time lapse photographs of an ACEL device on a PET substrate under extreme bending stress whilst maintaining full operation. **e)** Schematic inverted layer structure of a polymer light-emitting diode (PLED) with a FeCl$_3$-FLG or ITO cathode. Chemical structures of the polymer layers, F8BT and PEIE, are provided as insets. **f)** Comparative plot of the luminance efficiency of PLED pixels with FeCl$_3$-FLG (green) or ITO (orange) cathodes. **Inset:** Photograph of a PLED with FeCl$_3$-FLG electrode with a DC voltage applied across one of eight pixels.

is imparted to the luminescent centre which promotes a trapped electron to an excited state before recombining radiatively. These devices function entirely as capacitive structures, with no charge carriers injected from the electrodes. Their main applications are for large area display panels used for ambient back-lighting and advertising boards.[106] Therefore, the main requirements of a top electrode material in ACEL panels are that it be transparent enough to allow efficient light emission, low sheet resistance such that a consistent voltage is applied over large surface areas and highly flexible so as not to limit the functionality of an otherwise pliable device structure. Even with sub-optimal intercalation staging, $FeCl_3$-FLG electrodes meet all of these requirements, with the resultant ACEL devices producing uniform brightness across panels with aspect ratios as extreme as 39:1. Moreover, these panels exhibit extreme flexibility almost to the point of complete folding, as shown in Figure 4.5d. The second device that we have trialled with intercalated graphene electrodes is an inverted structure PLED in which $FeCl_3$-FLG functions as a transparent cathode, as shown in the layer diagram in Figure 4.5e. An in-depth discussion of the motivation behind selection of each constituent material in this PLED structure goes beyond the scope of this thesis. However, we simply point out that the large-area $FeCl_3$-FLG electrode again serves as an effective replacement for sputtered ITO films, showing an improvement in luminance efficiency over an applied voltage range of $(4 - 15)V$ for the small preliminary sample of pixels measured in Figure 4.5f.

Future research directions

Based upon the findings of this chapter, we conclude that it would be necessary to systematically identify the variables which influence $FeCl_3$ vapour kinetics in order to attain uniform intercalation of few-layer CVD graphene. Although it is certainly possible that films as thin as just two atomic layers will behave radically differently to bulk materials, we can offer some initial suggestions from the well-established field of graphite intercalation compounds.[85,107] A higher energy input is required to initially separate adjacent layers in bulk graphite than the energy required to facilitate subsequent diffusion of intercalant vapour throughout the Basal plane. It therefore could be worthwhile to investigate the effect of increasing the temperature of the zone in which few-layer graphene films are housed during the initial stage of intercalation. Additionally, the presence of excess chlorine gas was found to lower the threshold vapour pressure at which $FeCl_3$ saturates between all layers of bulk graphite. The use of compressed Cl_2 gas cylinders is undesirable but it may be possible to manipulate the equilibrium concentration of Cl_2 in $FeCl_3$ vapour by adjusting environmental parameters. If none of these efforts prove successful, $FeCl_3$-FLG films could be applied in LED devices where they are in contact with a charge transport layer

such as MoO_3 which has been shown to p-dope monolayer graphene films.[108] This could potentially solve the challenge of inducing sufficiently high charge carrier concentrations in the base bilayer film of regions with low grain density. Secondly, efforts to optimise the growth of CVD graphene on nickel would be highly useful, given the influence of grain density on the sheet resistance across these electrodes.

4.4 Conclusions

In conclusion, we have developed the first method of up-scaling $FeCl_3$-intercalated few-layer graphene from micron-scale flakes to macroscopic continuous films which can be utilised as transparent electrodes in optoelectronic devices. Through the method of scanning Raman spectroscopy, we have established that stage-2 (i.e. complete) intercalation can consistently be achieved in few layer graphene grains with more than two layers which are formed during the precipitation phase of CVD growth. However, neither stage-1 (one $FeCl_3$ layer adjacent to graphene) nor stage-2 intercalation could be achieved within the continuous films of bilayer graphene which interconnect these thicker grain regions. This was found to produce spatial variations in sheet resistance across large-area $FeCl_3$-FLG electrodes ranging from $R_{sq} = 635\Omega/sq$ in regions with low grain density to $R_{sq} = 95\Omega/sq$ in regions of high grain density. Nevertheless, this study provides valuable information as to what challenges remain in optimising the electrical and optical properties of large-area $FeCl_3$-FLG films. It also signifies the first successful attempts to incorporate $FeCl_3$-FLG electrodes into light-emitting devices.

5

Laser written intercalated graphene photodetectors

[1] [2]

[1]The findings presented in this chapter have been published in the follwing article: *Extraordinary linear dynamic range in laser-defined functionalized graphene photodetectors*, A. de Sanctis, **G. F. Jones**, D. J. Wehenkel, F. Bezares, F. H. L. Koppens, M. F. Craciun and S. Russo, *Science Advances*, **3**, e1602617.

[2]Photocurrent and Raman spectroscopy measurements of $FeCl_3$-FLG presented in this chapter were recorded by Dr Adolfo de Sanctis. Gareth F. Jones made significant contributions to all aspects of this research project including (but not limited to) device fabrication, preliminary photocurrent/Raman spectroscopy measurements, analysis/interpretation of data and the writing of associated manuscripts.

5.1 Introduction

In Section 2.4.2 of Chapter 2, we reviewed the range of ways by which photocurrent can be generated at planar junctions in graphene. These junctions are defined by changes in the local density of states, created by either electrostatic gating,[23,26,60] chemical doping[27,62–64] or variations in layer number.[109] Graphene photodetectors containing such junctions almost always respond to light in a manner that is dominated by hot charge carrier dynamics and photo-thermoelectric effects. Prolonged hot carrier lifetimes are potentially useful for the purpose of solar energy harvesting,[110] but they also create a sub-linear proportionality between photocurrent and optical power.[25] This is undesirable in applications such as radiometry. Building from the conclusions of the previous chapter, we report here that $FeCl_3$-FLG can also be used for the purposes of light detection. Photo-responsive p-p' junctions are selectively written into $FeCl_3$-FLG using the simple method of scanning optical lithography. From theoretical estimations, we conclude that strong p-doping from $FeCl_3$ accelerates the cooling of hot carriers at lateral graphene junctions. This minimises the contribution of thermoelectric currents in short circuit read-out signals, thereby leaving photovoltaic effects as the dominant source of photocurrent. Hot carriers which remain are maintained at temperatures close to that of the lattice, preventing the onset of a sub-linear photo-response even at powers as high as $10 MW cm^{-2}$. Overall, this results in photo-responsive graphene junctions with a linear dynamic range of 44dB, approximately 2-3 orders of magnitude larger than similar structures in pristine monolayer graphene.[111] These results present a new method by which the charge carrier dynamics in graphene can be reliably tailored for use in photodetector devices.

5.2 Experimental Details

5.2.1 Laser-assisted de-intercalation of $FeCl_3$-FLG

The starting material for the photodetector devices discussed in this chapter was an isolated flake of few-layer graphene on an SiO_2/Si substrate with a $280nm$-thick gate dielectric. Flakes were deposited by means of the mechanical exfoliation method (i.e. cleaved using scotch tape).[3] For this experiment, we opted not to use CVD-grown films because the research presented in Chapter 4 has shown that a higher degree of $FeCl_3$ intercalation can currently be achieved uniformly across mechanically exfoliated flakes.[18] Figure 5.1a shows the Raman spectrum of one such flake, which we identified as four-layer graphene from the degenerate nature of the 2D peak[92] and optical contrast measurements under white light[47] (shown as an inset). Once graphene flakes of a suitable layer number and

size for our experiment had been identified, we intercalated these samples with $FeCl_3$ following the physical vapour transport method outlined in Section 3.1.2. After intercalation, source and drain contacts of 5nm/50nm Cr/Au were thermally evaporated onto selective regions of each flake using standard electron beam lithography methods followed by lift-off in acetone. A Raman spectrum focussing on the G band of the same four-layer flake was acquired before de-intercalation and is presented in Figure 5.1b. The spectrum shows all three split modes G_0, G_1 and G_2 centred around $\sim 1589cm^{-1}$, $\sim 1615cm^{-1}$ and $\sim 1625cm^{-1}$ are present after intercalation and electrode fabrication. As stated in Section 3.4 of Chapter 3, these peaks represent $FeCl_3$-intercalation staging orders of > 2, 2 and 1 respectively. Focusing on the $1345cm^{-1} > \Delta\omega > 1355cm^{-1}$ range of the spectrum, we see that no D peak is present. This signifies that the degree of disorder is low within this sample. From the relative intensity of the three G peaks, we made the following conclusions about the molecular stacking within this flake: Firstly, the presence of all three G_0, G_1 and G_2 peaks implies that staging orders of 1, 2, and > 2 each apply to at least one of the four graphene layers. Secondly, the dominant intensity of the G_1 peak signifies that two of the four layers are stage-2 intercalated. Thirdly, the weak intensity of the G_0 peak suggests that the graphene layer with a staging order > 2 is not on the top surface of the flake. As a final caveat, we also note that it is highly unlikely for $FeCl_3$ to be present on the top or bottom surface of the flake, where it would come into direct contact with all the organic solvents used during electron beam lithography fabrication processes. Based upon these conclusions, we inferred the molecular stacking order in this four-layer graphene flake which is illustrated in the inset of Figure 5.1b. We deduced that $FeCl_3$ vapour has diffused throughout all but the lowermost interlayer regions of the flake during intercalation.

Following initial Raman spectroscopy measurements, the middle region of the $FeCl_3$-FLG flake was irradiated by a focused $\lambda = 532nm$ laser line at an optical power density of ($P = 15.3MW/cm^2$). This power density is two orders of magnitude stronger than those used in Raman spectroscopy measurements (see Section 5.2.2). High intensity laser irradiation was delivered by means of a rasterised scan in $\Delta x, \Delta y = 500nm$ steps, waiting 3 seconds at each position. Returning to the same location from which we inferred the stacking order before irradiation, we recorded a second Raman spectrum at this position. The resulting spectrum is shown in Figure 5.1c. It is clear that the relative intensity of the G_0, G_1 and G_2 peaks have radically altered such that the spectrum is now reminiscent of the CVD $FeCl_3$-FLG films that we characterised in Chapter 4. The G_2 peak has disappeared, whilst the G_1 peak has broadened and red-shifted to $\sim 1608cm^{-1}$. Additionally, the G_0 peak intensity has markedly increased and its position has undergone a marginal

red-shift to $\sim 1587cm^{-1}$. All of these changes point towards a mechanism whereby $FeCl_3$ is partially de-intercalated under intense laser irradiation. An inset in the lower plot of Figure 5.1b illustrates the new proposed molecular stacking order, which we have inferred from the changes to the G band that were just discussed. In this new arrangement, $FeCl_3$ molecules which remain between graphene layers in the laser-mapped region are no longer tightly packed and have dispersed such that the molecular stacking now forms a broad variation of higher staging orders (≥ 2).

Figure 5.1d shows a schematic illustration of the $FeCl_3$-FLG transistor. A diagram of the short circuit configuration used in all photocurrent measurements in this chapter is also provided. The $5.5\mu m$-wide partially de-intercalated region of the channel is highlighted in green. Extrapolating downwards from this schematic, Figure 5.1d sketches two lines of potential energy within graphene: the Fermi energy (dashes) and the charge neutrality point (solid line) as a function of displacement, y, along the length of the channel. Superimposed band diagrams (with k, not y along the bottom axis) denote the doping at a finite location in the middle of each region. In the remainder of our discussion we refer to highly intercalated regions as 'p-doped' and the partially de-intercalated laser-irradiated regions as 'p'-doped'. Similarly, dashed terms (e.g. σ') denote physical parameters of the p'-doped region. Line scans of the G_1 and G_2 peak positions along the length of the same channel are plotted in Figure 5.1e for measurements taken before (black) and after (red) laser-induced de-intercalation of the middle section. From these plots, we can confirm that a red-shift in $Pos(G_1)$ and removal of the G_2 peak occurs throughout the laser-mapped region. In contrast, the position of G_1 and G_2 peaks remain largely unchanged across the immediate surrounding area of the mapped region. The transistion between p and p' regions occurs over a length of approximately $1\mu m$, which correlates with the laser spot resolution. Based upon these observations, we can offer a few comments regarding the mechanism of laser-induced de-intercalation: Raman spectra recorded after partial de-intercalation of $FeCl_3$-FLG are also absent of a D peak (see Figure 5.1b). Combined with the fact that micrograph images (discussed later) show no signs of physical damage, we have excluded the possibility that laser ablation contributes towards the observed changes in Raman spectra. Furthermore, defect-free graphene sheets are known to be impermeable to all atoms.[112] It is therefore highly improbable that $FeCl_3$ molecules escape vertically through the graphene stack if we observe no signatures of structural damage. Finally, we find no evidence in Figure 5.1d to suggest an increased concentration of $FeCl_3$ in regions directly next to the laser-irradiated area. With these points in mind, we suspect that intercalated $FeCl_3$ molecules are sublimated or otherwise displaced under intense laser irradiation and, over the duration of a rasterised laser scan, diffuse out of the side walls

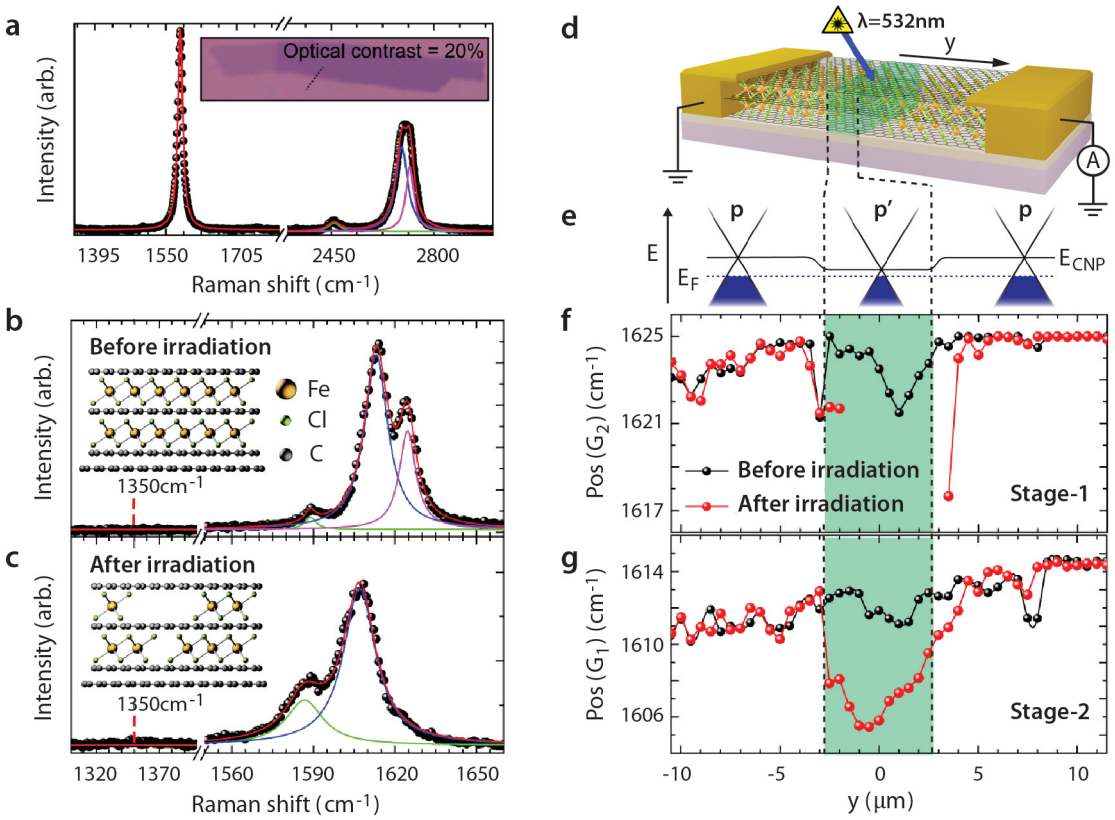

Figure 5.1: Laser-induced de-intercalation of $FeCl_3$-FLG. a). Raman spectrum of a four-layer pritine graphene flake on SiO_2/Si. **Inset:** Micrograph image of the same few-layer flake illuminated by white light. Dashed line denotes the boundary across which optical contrast values were calculated. **b)** Raman spectra of the same four-layer flake after intercalation with $FeCl_3$ and **b)** after laser-induced de-intercalation. **Insets:** Illustrations of the molecular stacking structure inferred from each Raman spectrum. **d)** Schematic diagram of a laser-irradiated $FeCl_3$-FLG transistor and **e)** the built-in field created at the interfaces of a p-p'p junction. Line scans detailing the position of **f)** G_2 and **g)** G_1 peak positions along the length of the $FeCl_3$-FLG transistor channel before (black dots) and after (red dots) irradiation of the middle zone (green) with a scanning high intensity laser.

of the $FeCl_3$-FLG flake. Regardless of the exact kinetic process, this method presents an extremely simple way, akin to standard optical lithography procedures, to arbitrarily tailor the degree of p-doping throughout few-layer graphene.

5.2.2 Methods

All Raman spectra presented in this chapter were acquired in ambient conditions using a continuous-wave $\lambda = 532nm$ laser focused through a 50× objective to a spot diameter of $1\mu m$ and power density of $130kW/cm^2$. Spectra were collected using a $2400g/mm$ diffraction grating and acquisition time of 5 seconds. The power density of the laser line was attenuated using a motorised wheel of various neutral density filters. Photocurrent measurements were conducted using light sources from an array of solid-state laser diodes with various emission wavelengths. Light was focused using a 50× microscope objective ($NA = 0.8$) to produce a laser spot diameter of $l_0 \approx 1\mu m$. $l_0 = 297nm$ in the case of Figures 5.2f, 5.3a and Equation (5.11) following a system upgrade to diffraction-limited optics. The photocurrent signal was measured in short circuit configuration at the drain electrode with an inverting current amplifier (DL Instruments Model 1211) and its read-out voltage input to a lock-in amplifier (Ametek 7124). Optical power density was modulated as a square wave at the lock-in amplifier reference frequency of $73.3Hz$. Light intensity was adjusted by means of a variable voltage signal applied to the laser diode power module and physical insertion of neutral density filters into the beam's optical path. Power density levels were quantified by measuring the photocurrent produced by a calibrated Si photodiode (Thorlabs FDS100-CAL) when exposed to each light signal under reverse bias. All measurements were conducted in air at room temperature and were found to be reproducible over a period of more than one year.

5.3 Results

5.3.1 Photo-responsive p-p' junctions

Having established that p-p' junctions can be arbitrarily defined in select regions of $FeCl_3$-FLG via high-intensity laser patterning, we proceeded to examine the electronic response of these junctions to illumination at lower optical powers. High-resolution scanning photocurrent maps of the entire area of the four-layer $FeCl_3$-FLG flake were recorded before and after laser-assisted de-intercalation of the channel's middle region. These maps are shown in Figures 5.2a-e. Before de-intercalation (Figure 5.2b), doping across the the $FeCl_3$-FLG channel is uniform such that almost no photocurrent is generated away from

the $FeCl_3$-FLG - Cr/Au interfaces at source and drain electrodes. Photo-response from graphene in proximity to metallic contacts is a regularly reported phenomenon[111,113] and will not be discussed here. Two spots that show very faint photocurrent signals in Figure 5.2b correlate loosely with microscopic surface residues on the channel, as can be seen from the device image in Figure 5.2a. Following laser-assisted de-intercalation of the central channel region, two regions at the boundaries of the mapped area exhibit an approximately equal and opposite photo-response. Figures 5.2c-e show this effect to be independent of excitation wavelength across the UV-A to visible (red) range.

In Figure 5.2f, we measure the magnitude of photocurrent produced at one of the p'-p interfaces ("A" in Figure 5.2d) as a function of optical power density. A best fit to $I_{ph}(P)$ reveals a consistently linear photo-response over more than three decades of incident power. This behaviour extends up to higher power densities, until the onset of laser-assisted de-intercalation at $P > 10MWcm^{-2}$, and was found to be consistent across all measured excitation wavelengths (see Figure 5.2g). In contrast, a reference device of pristine few-layer graphene (black data in Figures 5.2f and 5.2f) produces a bolometric photocurrent under a DC source-drain bias of $10mV$ with a power exponent of $\alpha \approx 2/3$. Following our discussion in Section 2.4.2 of the power laws compiled in Figure 2.9, this sub-linear power exponent is a typical example of hot carrier effects in the case where $T_h >> T_L$ and hot carrier-phonon scattering is mediated by sites of disorder. The power law of these hot carrier effects saturates at significantly lower powers, $P \approx 30kWcm^{-2}$, which correlates closely with previous reports of lateral photocurrent signals in graphene photodetectors.[25,111,114,115]

5.3.2 Linear dynamic range

Photocurrent signals at p-p' junctions in $FeCl_3$-FLG appeared to exhibit consistent responsivity across an unusually large range of incident optical powers. Because of this, we decided to quantify the linear dynamic range (LDR) of these interfaces. Having established the saturation power density to be $P_{sat} = 10MWcm^{-2}$ from Figure 5.2f, we examined the lower limit of LDR in Figure 5.3a. By measuring the noise current, I_n, generated at a reference frequency slightly away from the frequency of light modulation, we determined the noise-equivalent power at the point where $I_n(P)$ and $I_{ph}(P)$ intersect. Importantly, the noise bandwidth, Δf, was kept constant amongst photocurrent and noise current measurements. We found $NEP = 4kWcm^{-2}$. Using Equation (2.24) from Section 2.3.1, we calculated a linear dynamic range of $LDR = 44dB$. In order to asses this value, we compiled the reported saturation power, noise-equivalent power and linear dynamic range of all published graphene photodetectors where $\alpha = 1$[25,28,111,114–117] in Figure 5.3.

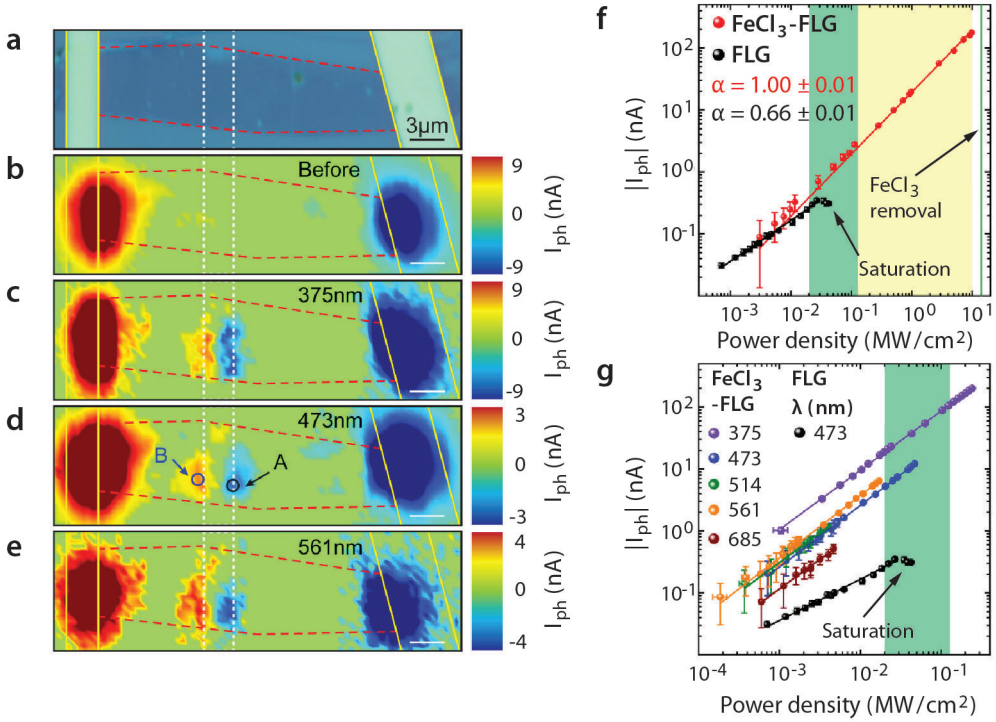

Figure 5.2: Photocurrent signals at p-p' junctions in $FeCl_3$-FLG. a). Micrograph image of a $FeCl_3$-FLG transistor with a laser-written p-p'p junction in the middle of the channel. Boundaries of the laser-written region are highlighted (dashed lines). Scanning maps of the short circuit current generated across the device area **b)** before ($\lambda = 473nm$) and **c)-e)** after ($\lambda = 375nm, 473nm, 561nm$) laser-assisted de-intercalation of the central region (dashed lines). $P = 38kW/cm^{-2}$ for all excitation wavelengths. **f)** Absolute magnitude of the short circuit photocurrent produced at a p-p' junction in $FeCl_3$-FLG (red) and the bolometric current produced by a pristine graphene transistor where $V_{DS} = 10mV$ (black). $\lambda = 473nm$. Power-law exponents determined from fits to $I_{ph} \propto P^{\alpha}$ (solid lines) are provided in the legend. Green highlight: The range of power density at which pristine graphene detectors are reported to saturate (see Figure 5.3b). Yellow highlight: The extended dynamic range of $FeCl_3$-FLG. **g)** Linear dynamic range measured at a p-p' junction in $FeCl_3$-FLG , (region A labelled in d)) for various excitation wavelengths.

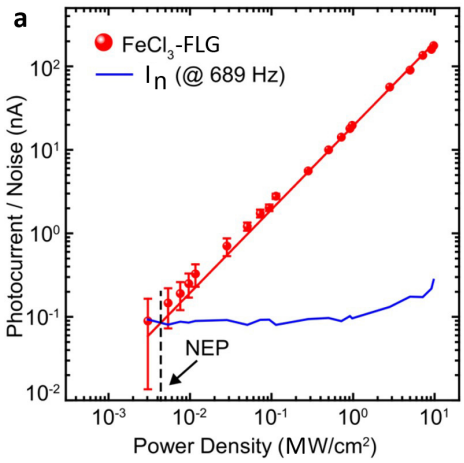

b

Reference	P_{sat} [a]	NEP [b]	LDR [c]
Kim *et al.* (116)	10^{-3} W/cm^2	-	-
Liu *et al.* (117)	1.27 W/cm^2	0.03 W/cm^2	15 dB [d]
Tielrooij *et al.* (114)	23 kW/cm^2	-	-
Mueller *et al.* (111)	51 kW/cm^2	10 kW/cm^2	7.5 dB [e]
Graham *et al.* (25)	57 kW/cm^2	-	-
Patil *et al.* (115)	14 kW/cm^2	-	-
Wang *et al.* (28)	120 kW/cm^2	3.3 kW/cm^2	15 dB [e]
This work			
FLG	45 kW/cm^2	-	-
FeCl$_3$-FLG	**$> 10^4$ kW/cm^2**	**4 kW/cm^2**	**44 dB** [d]

Figure 5.3: The linear dynamic range of reported graphene photodetectors. a) Plot of the photocurrent (red) and electrical noise (blue) generated at a p-p' interface of $FeCl_3$ as a function of optical power density. $\lambda = 473nm$. Dashed line highlights the noise equivalent power. **b)** Table compiling the reported [a] saturation power, [b] noise-equivalent power (if available) and [c] linear dynamic range (if available) of graphene photodetectors. [d] Measured value. [e] Estimated value.

Comparing these values, it appears that the linear dynamic range of p-p' interfaces in $FeCl_3$-FLG is unusually large. Suspecting that the high charge carrier concentration induced by $FeCl_3$ intercalation has a significant role to play in this anomalous behaviour, we next endeavoured to understand the effect of $FeCl_3$ intercalation on photovoltaic and photo-thermoelectric photocurrent signals.

5.3.3 Theoretical estimates of PV and PTE effects in $FeCl_3$-FLG.

As an attempt to understand our findings of an enhanced linear dynamic range in p-p' $FeCl_3$-FLG junctions compared to pristine graphene photodetectors, we applied the PV-PTE model of Song et. al.[60] to the case of these highly-doped interfaces. This model corresponds to theoretical concepts introduced in Section 2.4.2 concerning short circuit photocurrent in monolayer graphene. By applying this to $FeCl_3$-FLG, we are making the assumption that adjacent graphene sheets in a few-layer graphene flake are electronically de-coupled monolayers once $FeCl_3$ molecules diffuse between them. Whilst this is valid for stage-1 intercalated layers (see Section 3.1.2), the assumption becomes more tenuous in regions with a lower degree of intercalation. We discuss this further in Section 5.4.

Using Equations (2.39) and (2.37) as starting points, we need to establish values for the chemical potential and conductivity either side of the p-p' junction. Electrical measurements of the Hall voltage across our device would provide the most accurate values of total charge carrier concentration but this requires incrementally spaced voltage

probes along the channel. These could act as additional heat sinks and interfere with the density of states near photo-responsive junctions. Hall voltage measurements would also not provide an easy way by which to evaluate the conductivity of each electrically isolated graphene layer. Instead, we chose to use Raman spectroscopy to estimate n and ϕ_c throughout the $FeCl_3$-FLG flake.

Based on our interpretation of molecular ordering throughout the partially-irradiated channel, the flake shown in Figure 5.4a is four-layer graphene where the bottom two sheets remain electrically coupled as a bilayer. Going from top to bottom, we now refer to the decoupled graphene systems as A, B and C (Figure 5.4b). The chemical potential of the bilayer system C will not be affected as radically as the monolayers A or B when in proximity to just one layer of $FeCl_3$, we therefore focus our discussion on the upper two layers of the flake. We also simplify the system to a single p-p' junction, given that the laser spot does not illuminate the entire p-p'-p structure at once. In Figure 5.4d, we numerically evaluated the DFT model of Lazzeri et al[94] to convert from the positions of G_1 and G_2 Raman peaks in Figures 5.1f and 5.1f to the carrier concentration in each layer before and after laser writing ($n'_A \approx n'_B$ after irradiation). Taking a linear band approximation, we then estimated the spatial variation in chemical potential in Figure 5.4d. This yielded average values of $\phi_{cA} = (-0.88 \pm 0.02)\, eV$, $\phi_{cB} = (-1.12 \pm 0.2)\, eV$ and $\phi'_{cA,B} = (-0.76 \pm 0.02)\, eV$. Marginally smaller values of chemical potential have been measured via Kelvin probe microscopy in the CVD $FeCl_3$-FLG films discussed in Chapter 4,[102] but our estimates correlate well with previously reported DFT calculations[118] and Raman spectroscopy measurements[99] of exfoliated flakes.

Two terminal resistance measurements of the $FeCl_3$-FLG flake in Figure 5.4a were taken before and after laser patterning using a lock-in amplifier in constant current configuration. Through image analysis, we calculated the change in channel width along each region of the flake (plotted in Figure 5.4c) and related these dimensions to the total conductivity of the channel, σ_{tot}.

$$R_{SD} = \frac{1}{\sigma_{tot}} \int_{-L/2}^{L/2} \frac{1}{W\,(y)} dy \tag{5.1}$$

$$R'_{SD} = \frac{1}{\sigma_{tot}} \left[\int_{-L/2}^{y_1} W\,(y)^{-1}\, dy + \int_{y_2}^{L/2} W\,(y)^{-1}\, dy \right] + \frac{1}{\sigma'_{tot}} \int_{y_1}^{y_2} W\,(y)^{-1}\, dy \tag{5.2}$$

Here, y_1 and y_2 denote the boundaries of the irradiated p' area. Through Equations (5.1) and (5.2) we found $\sigma_{tot} \approx 27mS$ and $\sigma'_{tot} \approx 10mS$, slightly below the maximum reported conductivity of fully intercalated four-layer flakes.[18] Approximating $n_{tot} \approx 2n_A + n_B$ and $n'_{tot} \approx 3n'_{A,B}$, the average hole mobility was taken to be $\langle \mu \rangle = 650 cm^2 V^{-1} s^{-1}$.

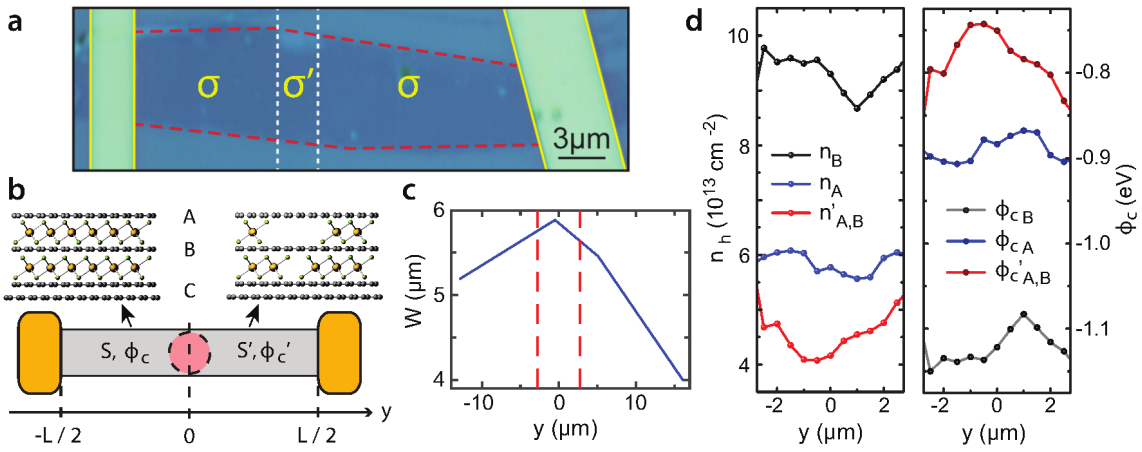

Figure 5.4: Calculation of the carrier concentration and chemical potential at p-p' interfaces of $FeCl_3$-FLG. a), Micrograph picture of a four-layer $FeCl_3$-FLG flake with a p-p'-p junction patterned by $\lambda = 532nm$ laser irradiation. Superimposed lines represent flake boundaries (red), contacts (yellow) and the de-intercalated area (white). **b)** Schematic of a p-p' interface located at the centre of a long, narrow $FeCl_3$-FLG channel. The degree of intercalation, inferred from Raman spectroscopy measurements, is illustrated for each region with the three decoupled systems labelled A, B and C. **c)** Width of the flake shown in a) as a function of displacement from the channel's middle. Red dashes mark the boundaries of the p' region. **d)** Concentration of charge carriers in decoupled graphene layers inferred from the position of the G_1 and G_2 Raman peak positions shown in Figure 5.1e. The chemical potential is then calculated using the density of states for monolayer graphene.

Finally, we established conductivity values for the individual systems A and B using Equation (2.13), which is repeated below (we will duplicate several equations from Chapter 2 in this section for the sake of clarity).

$$\sigma\left(\phi_c\right) = \sigma_{min}\left(1 + \frac{\phi_c^2}{\Lambda^2}\right) \tag{5.3}$$

From this, we estimated $\sigma_A = 6.0mS$, $\sigma_B = 9.6mS$ and $\sigma'_{A,B} = 4.5mS$.

Equations (2.39) and (2.37), established in Section 2.4.2 provide us with expressions for the drift-assisted and diffusion-assisted components of photocurrent at asymmetrically-doped interfaces in monolayer graphene. Considering the temperature gradient driven component first, we write

$$I_{PTE} = \frac{2\pi^2 k_B^2 T_h}{3eR} \cdot \frac{\Delta T}{\phi_c \phi_c{}'} \cdot \left[\phi_c{}'\left(1 - \frac{\sigma_{min}}{\sigma}\right) - \phi_c\left(1 - \frac{\sigma_{min}}{\sigma'}\right)\right] \tag{5.4}$$

The elevated hot carrier temperature, ΔT, is difficult to measure experimentally. Typically, one would require picosecond resolution of photocurrent transients in low temperature environments[25] which is beyond the scope of our experimental apparatus. Alternative methods which approximate values of ΔT using Equation (5.4) rely on the assumption that any measured photovoltage is produced solely by thermoelectric currents.[23] This inference cannot be made for $FeCl_3$-FLG interfaces; extremely high carrier densities (up to $3 \times 10^{14} cm^{-2}$ per layer) efficiently screen electrostatic gating potentials and prohibit experimental methods which would otherwise be used to verify the 'six fold pattern' signature of hot carriers[22,23,25,61] (see Section 2.4.2). Instead, we use the solution of Song et. al.[22] (Equations (2.35) and (2.34), repeated below)

$$\Delta T = \frac{\alpha_\lambda \epsilon_0 l_0 N_{ph}}{\frac{\kappa}{\xi} coth\left(\frac{L}{2\xi}\right) + \frac{\kappa'}{\xi'} coth\left(\frac{L}{2\xi'}\right) + \frac{T_L}{RW}\left(S' - S\right)^2} \tag{5.5}$$

$$\xi = \sqrt{\frac{\sigma}{\gamma_h e^2 D\left(\phi_c\right)}} \tag{5.6}$$

Provided $k_B T \leq \left(\phi_c, \phi_c{}', \Lambda\right)$, the third term of the denominator in Equation (5.5) is negligible. The cooling length, ξ, of each graphene layer is dependent upon its electrical conductivity, density of states ($D\left(\phi c\right)$) and the hot carrier cooling rate (γ_h).[23] Our next task must therefore be to establish whether supercollisions or single acoustic phonon processes dominate cooling mechanisms.

For graphene layers where $n \geq 10^{13} cm^{-2}$, the Bloch-Grüneisen temperature reaches hundreds of Kelvin and hot electrons may completely equilibrate with the lattice via just a single acoustic phonon interaction under CW illumination.[51] Disorder-mediated scattering is therefore not relevant in our devices. This can be shown by substituting

Equation (5.3) into Equation (2.28) using the relation for the mean free path of a two-dimensional electron gas, $l = \sigma\hbar\pi/ke^2$, to estimate the relative magnitudes of power loss via supercollisions and momentum-conserving scattering events in $FeCL_3$-FLG. For $T_h - T_l << T_l$, we find supercollisions to make up as little as 3% (11%) of the total heat loss from hot electrons before (after) laser-induced de-intercalation. The scattering rate can therefore be approximated by considering just single acoustic phonon processes (Equation (2.26), repeated below).[70]

$$\gamma_h \approx \frac{3D^2\phi_c^3}{4\pi^2\hbar^3\rho_m {v_F}^4 k_B T_L} \tag{5.7}$$

Due to the doping induced by $FeCl_3$ intercalation, the cooling rate of momentum-conserving acoustic phonon coupling dramatically increases from $\gamma_h \sim 10^9 s^{-1}$ at $\phi_c = 100meV$ to $\gamma_{h(A)} = 6 \times 10^{11} s^{-1}$, $\gamma_{h(B)} = 1 \times 10^{12} s^{-1}$ and $\gamma'_{h(A,B)} = 4 \times 10^{11} s^{-1}$. This is in agreement with the picosecond relaxation time-scales of $FeCl_3$-FLG measured via pump-probe spectroscopy.[118] Hence, we use Equation (5.6) to calculate cooling lengths of $\xi_A = 220nm$, $\xi_B = 170nm$ and $\xi'_{A,B} = 260nm$. Given that $\xi << L/2$ for all of our devices, Equation (5.5) simplifies to

$$\Delta T \approx \alpha_\lambda \epsilon_0 l_0 N_{ph} \left(\frac{\kappa}{\xi} + \frac{\kappa'}{\xi'}\right)^{-1} \tag{5.8}$$

Substituting Equation (5.8) into Equation (5.4) and employing the Wiedemann-Franz relation (Equation (2.14)),[49] we arrive at a full expression for the photo-thermoelectric current produced at a p-p' junction in $FeCl_3$-FLG.

$$I_{PTE} \approx \frac{2e\eta_i k_B T_L l_0 N_{ph}}{\phi_c \phi_c' R} \cdot \left[\phi_c' \left(1 - \frac{\sigma_{min}}{\sigma}\right) - \phi_c \left(1 - \frac{\sigma_{min}}{\sigma'}\right)\right] \cdot \left[\frac{\sigma}{\xi} + \frac{\sigma'}{\xi'}\right]^{-1} \tag{5.9}$$

where $\eta_i \sim \alpha_\lambda \epsilon_0 / k_B T_L$ is the internal quantum efficiency. We then eliminate unknown quantum efficiency terms by approximating $N_{ph} \approx n_{ph}/\eta_{EQE} \langle\tau\rangle$, where η_{EQE} is the external quantum efficiency, $\langle\tau\rangle \sim \langle\gamma\rangle^{-1}$ is the average hot carrier lifetime and $\langle\gamma\rangle$ is the average scattering rate of hot carriers with phonons across both sides of the junction. The low responsivity of all measured devices ($\gamma \leq 10^4 A/W$) indicates that the external quantum efficiency is not limited by the absorbance of $FeCl_3$-FLG. We therefore make a final approximation that $\eta_{EQE} \approx \eta_i$.

$$I_{PTE} \approx \frac{2ek_B T_L l_0 n_{ph} \langle\gamma\rangle}{\phi_c \phi_c' R} \cdot \left[\phi_c' \left(1 - \frac{\sigma_{min}}{\sigma}\right) - \phi_c \left(1 - \frac{\sigma_{min}}{\sigma'}\right)\right] \cdot \left[\frac{\sigma}{\xi} + \frac{\sigma'}{\xi'}\right]^{-1} \tag{5.10}$$

Dividing Equation (5.10) by Equation (2.39), the relative magnitudes of photo-thermoelectric and photovoltaic currents at $FeCl_3$-FLG p-p' junctions may be estimated.

$$\frac{I_{PTE}}{I_{PV}} \approx \frac{2ek_BT_Ll_0\langle\gamma\rangle}{\mu\Lambda} \cdot \frac{\sigma_{min}\left[\phi_c{}'\left(1-\frac{\sigma_{min}}{\sigma}\right)-\phi_c\left(1-\frac{\sigma_{min}}{\sigma'}\right)\right]}{\phi_c\phi_c{}'\left(\frac{\sigma}{\xi}+\frac{\sigma'}{\xi'}\right)\left[tan^{-1}\left(\frac{\phi_c}{\Lambda}\right)-tan^{-1}\left(\frac{\phi_c{}'}{\Lambda}\right)\right]} \tag{5.11}$$

For both decoupled systems A and B, we calculate $I_{PTE}/I_{PV} \approx -0.06$. We therefore expect the thermally-assisted diffusion of hot carriers to make a minor contribution towards the total photocurrent generated at $FeCl_3$-FLG p-p' junctions and to act in the opposite direction to current produced by the photovoltaic effect. This result supports our findings in Figure 2.8 of Section 2.4.2.

5.4 Future research directions

Through a combination of experimental and theoretical investigations, we have come to the conclusion that laser-written p-p' junctions in $FeCl_3$-FLG exhibit an unusually large linear dynamic range due to the accelerated cooling of hot carriers in highly-doped graphene layers. However, our calculation of $I_{PTE}/I_{PV} \approx -0.06$ in Section 5.3.3 involved several approximations. In particular, we have assumed that the base bilayer graphene sheet does not contribute towards photocurrent signals and that all partially-intercalated graphene layers are electronically de-coupled from one another. If our dismissal of the base layer is incorrect, a magneto-transport study of bilayer graphene[119] has shown $\gamma_h(n)$ to increase at a faster rate than in graphene monolayers. Therefore, our prediction that photo-thermoelectric current signals are reduced is likely to remain valid. With regards to our assumption of parallel monolayer graphene systems, we have attempted to experimentally verify the predicted change in photocurrent polarity during the transition between predominant photo-thermoelectric and photovoltaic currents in samples of monolayer graphene at high charge carrier concentrations. The only method by which n can be electrically modulated to approach levels induced by $FeCl_3$ intercalation is through ionic polymer gating. This involves depositing a polymer containing mobile ions, usually Li^+ and ClO_4^-, on top of a graphene device. Mobile ions drift under an applied DC voltage to electrostatically gate graphene with a capacitance per unit area approximately two orders of magnitude greater than is possible using SiO_2/Si gates.[95] Figure 5.5a shows an AFM phase image of such a device. A 40nm dielectric spacer of hexagonal boron nitride was laminated onto the middle of a monolayer graphene channel before depositing the ionic polymer gate so that p-p' and n-n' junctions could be induced with a single global gating potential. Unfortunately, as the photocurrent map in Figure 5.5b shows, these mobile ions are also unstable in air and introduce inhomogeneous doping throughout the entire device. Because of this, we were unable to accurately asses the number of polarity changes in I_{ph}

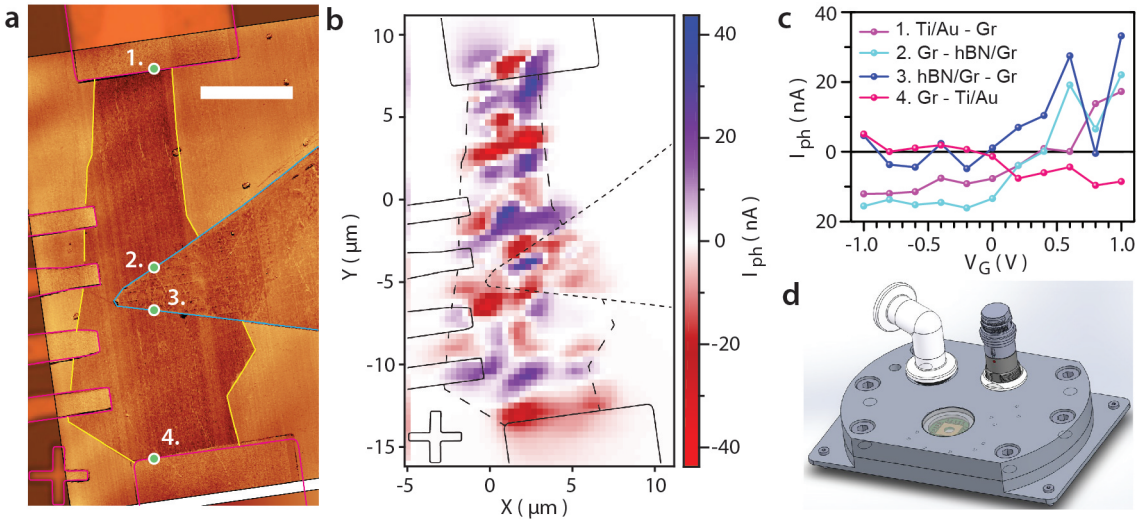

Figure 5.5: Ionic polymer-gated n-n'/p-p' junctions. **a)** AFM phase map with overlaid outlines of a $40nm$ hexagonal boron nitride ('hBN', blue) dielectric spacer partially covering a monolayer graphene flake ('Gr', yellow) with Ti/Au electrodes (pink). **b)** A scanning short-circuit photocurrent map of this device in ambient conditions, where $V_G = 1V$, $\lambda = 561nm$ and $P = 210kWcm^{-2}$. **c)** Short circuit photocurrent as a function of gate voltage recorded at locations labelled in a). **d)** 3D rendering of a prototype slim-line vacuum chamber probe station for various scanning microscopy measurements.

during sweeps of gate voltage (see Figure 5.5c). To assist future research projects concerning environmentally unstable materials, we have recently designed, proto-typed and installed a custom vacuum chamber probe station that retro-fits to our existing scanning optical microscope system. A 3D schematic of this chamber is provided in Figure 5.5d. With this newly-installed equipment, we are now able to conduct future research projects concerning environmentally unstable materials using a wide variety of scanning optical microscopy and spectroscopy measurements in a high vacuum environment.

5.5 Conclusions

In this chapter, we have shown that asymmetrically-doped p-p' junctions can be laser-written into $FeCl_3$-intercalated few-layer graphene to produce photo-responsive interfaces with a linear dynamic range of $LDR = 44dB$. Through examining the polarity of photocurrent signals and theoretical calculations based on a model of competing photovoltaic and photo-thermoelectric effects, we concluded that the accelerated cooling of hot carriers in highly p-doped graphene is responsible for this extended linear photo-response. Overall, this presents a novel method by which the electronic properties of graphene may be tailored to exhibit a linear electrical response to a variable light source. The comparatively large

linear dynamic range that we have engineered could be of use in high-power radiometry applications. However, we note that the responsivity of these junctions is extremely low ($\gamma < 10^{-4} A/W$ across visible wavelengths), which prevents detection of light signals below a high noise-equivalent power density of $4kWcm^{-2}$. In the final experimental chapter of this thesis, we will focus on a method of adapting graphene such that light intensities far below this limit may be electrically detected.

6

Rubrene single crystal-graphene phototransistors

1 2

[1]Some of the findings discussed in this chapter have been accepted for publication in the following manuscript: *Highly efficient rubrene-graphene charge transfer interfaces as phototransistors in the visible regime*, **G. F. Jones**, R. M. Pinto , A. de Sanctis, V. K. Nagareddy, C. D. Wright, H. Alves, M. F. Craciun and S. Russo, *Advanced Materials*.

[2]Dr Rui M. Pinto assisted with the growth and lamination of all rubrene single crystals presented in this chapter. Gareth F. Jones fabricated all devices, undertook all measurements, analysed/interpreted all data and wrote the manuscript associated with this chapter.

6.1 Introduction

As discussed in Section 2.4.2, the planar interfaces formed between monolayer graphene and semiconductor materials present unique opportunities for the detection of extremely weak light signals. Specifically, the non-zero band gap and strong light-matter interactions in semiconductors provide spectral selectivity and efficient optical absorption which graphene lacks. Conversely, an optimum surface area to volume ratio and high charge carrier mobility makes graphene extremely sensitive to the injection of photo-excited charge carriers and facilitates large photo-conductive gain, a combination which bulk semiconductors cannot offer. In comparison to the lateral graphene interfaces discussed in Chapter 5, this synergistic combination of materials radically enhances the responsivity of graphene-based photodetectors such that they produce resolvable signals in ultra-low light environments where, conventionally, only photomultiplier tubes and avalanche photodiodes are effective. Optimising the external quantum efficiency (EQE) of graphene phototransistors through the exploration of various material combinations is now a highly active field of research. Previous studies have focused on graphene interfaced with colloidal quantum dots;[29,35–37,120] transisiton metal dichalcogenides;[38,39] III-VI semiconductors;[40] metal oxides;[41] perovskites;[42] organometallic complexes[43,44] and polymeric/small-molecule organic semiconductors.[31–34] Room temperature EQE as great as 10^8 has been reported,[29] whilst variations in photo-generated charge trapping lifetimes make the speed of some detectors suitable for video-rate imaging[29,121] whereas others show memory capabilities.[38] However, several challenges still remain. It has not yet been determined which materials are best suited for light absorption in these systems and a lack of standardised characterisation procedures has promoted the use of ambiguous performance metrics which hinders accurate comparison amongst studies.

In this chapter, we systematically characterise graphene phototransistors which utilise a single crystal organic semiconductor, rubrene, as the light-absorbing layer. The choice of a single crystal was inspired by the short exciton diffusion lengths[122] and inhomogeneity[123] in solution-processed and thermally evaporated organic films which are expected to limit the quantum efficiencies of devices. Indeed, studies utilising amorphous[31,33,37,43,44] and polycrystalline[32,34] organic photo-active layers in graphene phototransistors have so far all displayed a photo-gating quantum efficiency (PGQE) less than 0.008% and 0.6% respectively. This is significantly lower than the maximum PGQE of $\sim 25-32\%$ achieved using inorganic semiconductor equivalents.[29,38] Our use of a structurally pristine single crystal organic semiconductor rather than a disordered film marks the first attempt to explore the underlying cause of this discrepancy and to determine the quantum efficiency

for every constituent process of photocurrent generation in a graphene phototransistor. We find that, through minimisation of structural disorder in light-absorbing layers and the use of appropriate characterisation methods, our devices exceed previously reported photo-gating quantum efficiencies of organic semiconductor-graphene phototransistors by one order of magnitude. Internal PGQE as large as 5% is measured at ultra-low light levels, whilst responsivity as large as $10^7 AW^{-1}$ and a detectivity of $9 \times 10^{11} Jones$ are attained at room temperature. Finally, we undertake a comparative study of all reported graphene phototransistors in order to argue the need for a renewed consensus regarding the appropriate figures of merit for these novel photodetectors.

6.2 Experimental Details

Device Fabrication

Continuous films of polycrystalline monolayer graphene were grown on Cu foils using the low pressure cold-wall CVD growth method[84] detailed in Section 3.1. Graphene films were then transferred onto SiO_2/Si substrates using the wet transfer technique detailed in Section 3.3. Graphene transistors were fabricated by performing three rounds of electron beam lithography on the transferred CVD-grown films using PMMA as a resist. After the first lithography cycle, incrementally spaced Au (30nm) electrodes were deposited on graphene by thermal evaporation. A rectangular channel was then defined using a 15W O_2/Ar plasma to etch graphene after the second lithography stage and, finally, Cr/Au (5nm/50nm) leads and bonding pads were thermally evaporated onto the exposed substrate after the third lithography stage. The quality of graphene was assessed after fabrication using Raman spectroscopy, a typical spectrum is shown in Figure 6.1 with relevant parameters of Lorentzian peak fits compiled in an inset table. The identified peaks are typical of polycrystalline graphene,[92] with the blue-shifted G peak position ($Pos(G) = 1588 cm^{-1}$) revealing a significant degree of p-type doping ($n \approx 6 \times 10^{12} cm^{-2}$ using the non-adiabatic model[94] described in Chapter 4), a common effect of adsorbed O_2, H_2O and PMMA residues from the transfer process.[124] Without a notch filter capable of resolving extremely low frequency interlayer shear modes,[125] we based our analysis of the film layer number upon the G and 2D peak profiles. The intensity ratio $I(G)/I(2D) = 0.49$ is larger than typical reports of pristine monolayer graphene[126] but a suppression of $I(2D)$ is expected due to the additional electron-electron scattering pathways present in doped samples.[95,127] Furthermore, the non-degenerate nature of the 2D peak indicates that interlayer transitions associated with multilayer stacking are absent.[97] The uncharacteristically

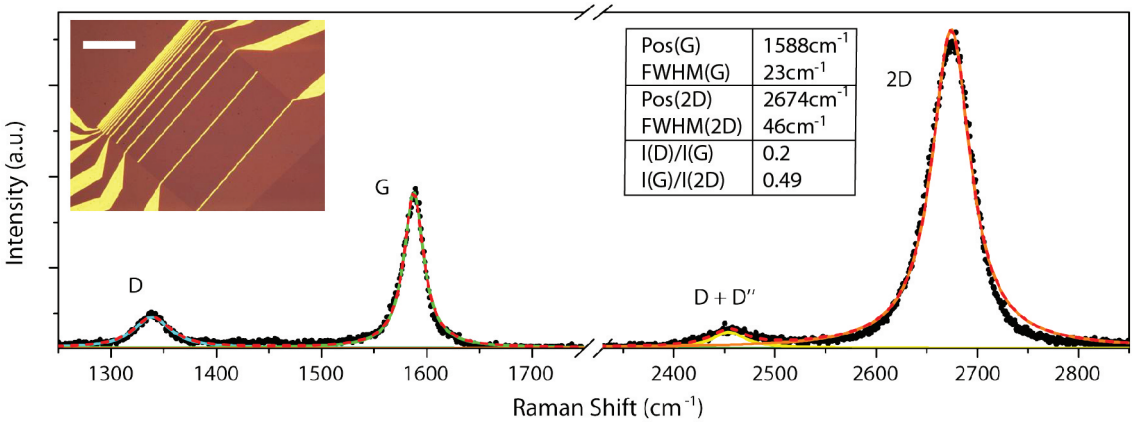

Figure 6.1: Raman spectrum of a CVD graphene transistor on SiO_2/Si. $\lambda_0 = 532nm$. Insets: Micrograph image of the measured graphene transistor (scale bar = $500\mu m$) and a table compiling relevant parameters of the Lorentzian peak fits.

broad FWHM of the 2D peak could be interpreted as a signature of turbostratic few layers[128] but, given the low carbon solubility of Cu, is more likely to be caused by nano-scale strain variations induced from the substrate transfer process.[93] We estimated the density of Raman-active scattering centres, using an empirical relation proposed by Cancado et. al.,[96] to be $n_D = 2.3 \times 10^{11} \cdot [I\,(D)\,/I\,(G)] = 4.5 \pm 1.2 \times 10^{10} cm^{-2}$. We note that scattering events at charged impurities do not contribute towards the Raman D band of graphene, which explains why n_D is much lower than the typical density of silanol groups on SiO_2 after exposure to HF.[90] Thin ($< 500nm$) single crystals of rubrene were grown via the physical vapour transport procedure discussed in Section 3.1.[87] A sharpened cocktail stick was used to pick up selected crystals via electrostatic adhesion and laminate them onto graphene transistors. Any graphene regions remaining un-covered by rubrene were then removed through a 40 second exposure to a 15W Ar plasma. Photoluminescence, cross-polarised optical microscopy and polarised Raman spectroscopy measurements, discussed below, did not show any evidence of significant damage to the rubrene crystal structure from this etching procedure. Micrograph images of an interface before and after etching are shown in Figure 6.2a and 6.2b respectively. Several rubrene crystals were laminated onto electrodes with no graphene present and several graphene transistors were not laminated with rubrene, serving as negative control samples in photocurrent measurements.

Crystallographic orientation and quality of rubrene

After complete fabrication of rubrene-graphene transistors, three independent experimental methods were used to confirm that rubrene samples were indeed highly ordered single crystals. One of these methods, cross-polarised optical microscopy, is presented in Figures

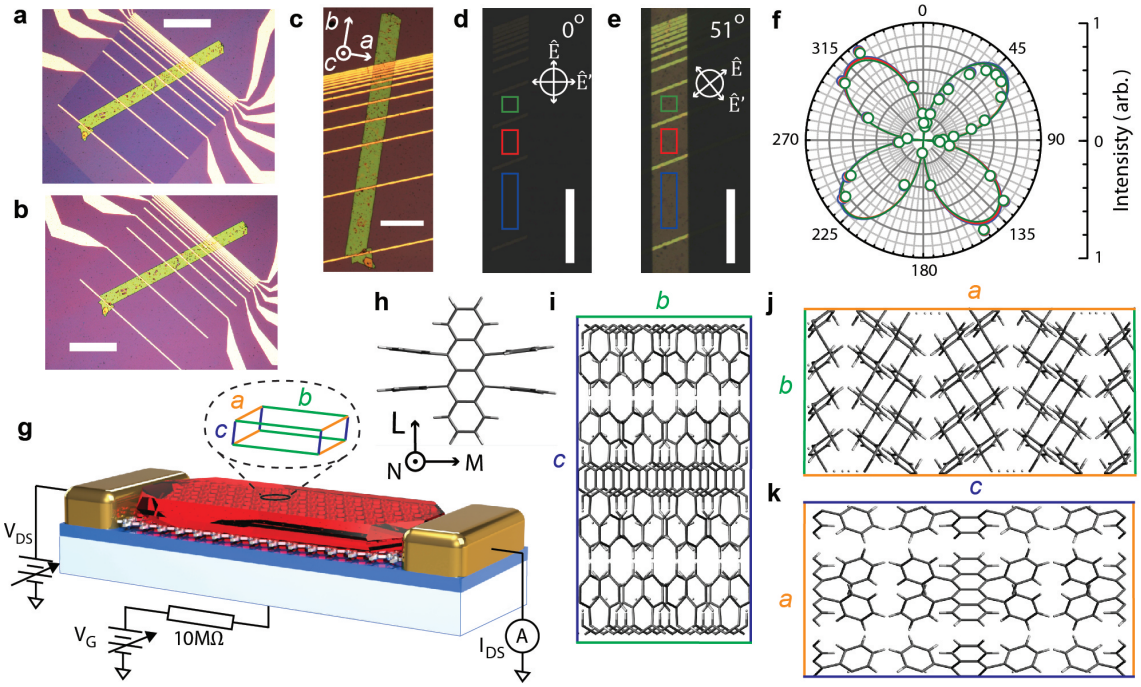

Figure 6.2: Lamination of rubrene onto graphene transistors. Micrograph images show a rubrene-graphene phototransistor **a)** before and **b)** after removal of exposed graphene with a 15W Ar plasma with crystallographic axes of the top surface labelled in **c)**. Cross-polarised optical microscopy images, captured with the rubrene crystal *b* axis oriented **d)** parallel and **e)** 51^o to the electric field vector of incident light, are overlaid with outlines of the channel regions that were analysed to produce polar plots of average grey-scale intensity shown in **f)**. **g)** A schematic of the rubrene-graphene transistor structure details the circuit configuration used in photocurrent measurements and the rubrene crystallographic axes relative to the macroscopic facets. Diagrams are provided of **h)** a single rubrene molecule and **i)-k)** molecular stacking in each crystallographic plane.

6.2d and 6.2e where micrograph images of a rubrene-graphene interface were captured for two different sample orientations. Uniform brightness was observed across the entire interface in each case, with intensity strongly dependent on the angle between the long axis of the crystal and the polarisation plane ($\vec{\mathcal{E}}$) of incident white light. Polar plots of the average brightness over three distinct interface regions (Figure 6.2 **f)** revealed a consistent four-fold pattern. This a clear signature of birefringence,[129,130] where the intensity captured by the microscope camera is proportional to the projection of electric field vectors for both ordinary and extraordinary rays exiting the rubrene crystal's top surface onto the polarisation plane ($\hat{\mathcal{E}}'$) of the filter in the analysed light path. If the sample were a polycrystalline rubrene film consisting of randomly oriented grains, bright and dark patches would be apparent in Figures 6.2d and 6.2e. On the other hand, if the sample were an amorphous film consisting of randomly oriented rubrene molecules, Figure 6.2f would have shown the image intensity to be independent of sample orientation. These cross -polarised optical microscopy measurements therefore provided strong evidence of consistent anisotropy throughout the entirety of each rubrene crystal used in our devices. Based on this finding and previous reports of lath-shaped rubrene single crystals,[131–133] we assigned crystallographic axes to the macroscopic facets of the rubrene samples as shown in Figures 6.2g-k. For this crystallographic orientation, the tetracene backbones of rubrene molecules (Figure 6.2h) form a herringbone stacking structure along the *ab* plane (Figure 6.2j) which extends parallel to the top and bottom surfaces of the crystal. Experimental evidence of this crystallographic orientation and confirmation of the structural quality of rubrene was provided by the photoluminescence (PL) spectrum shown in Figure 6.3, which was measured from the same interface as Figures 6.2a-e. The PL spectrum was fit with two sets of equidistant Voigt functions, which represent the vibronic progression of radiative transitions polarised along the L, N ($< 2.05eV$) and M ($> 2.05eV$) axes of rubrene molecules.[134] Although M-polarised emission is typically 10-20 times stronger, these peaks are less intense than L and N polarised PL in Figure 6.3. From this, we can infer that our axis of illumination and detection (normal to the top surface of rubrene) is oriented parallel to the M axes of all constituent molecules and therefore parallel to the c axis of the crystal. This correlates with the crystallographic orientation illustrated in Figure 6.2g. It is also important to note that a PL band located at 1.91eV, originating from surface photo-oxidation of rubrene[134] and deep trap states,[135] was absent from all measured samples. This demonstrated the high structural quality of the single crystals employed in our experiments.

The absorption coefficient (α) of rubrene single crystals is plotted on the right y-axis of Figure 6.3. This was determined from experimental measurements of the re-

flectance ($R(\lambda)$), transmittance ($Tr(\lambda)$) and thickness ($d = 1.6\mu m$, measured using a Dektak 3030ST profilometer) of a similar lath-shaped crystal laminated on glass. The following expression, derived from Beer's Law, assumes negligible absorption in glass, strong absorption in rubrene and the reflectance of the system to be dominated by the first reflection at the air/rubrene interface.:[136]

$$\alpha(\lambda) = -\frac{1}{d}\ln\left\{\frac{Tr(\lambda)}{[1-R(\lambda)]^2}\right\}. \tag{6.1}$$

The resultant absorption coefficient spectrum agrees well with established values for incident light normal to the *ab*-facet of rubrene single crystals.[134] Similar to our discussion of PL in rubrene, the 2.32eV peak in $\alpha(\lambda)$ represents the $HOMO \rightarrow LUMO$ electronic transition that only satisfies transition dipole moment selection rules if the electric field of absorbed light is polarised along the M axes of constituent rubrene molecules.[134,137] The more prominent series of peaks positioned above 2.32eV are higher vibronic modes of the same electronic transition, which are excited by light polarised along the L and N axes of rubrene molecules.[134] The 2.32eV peak is commonly observed as a shoulder peak, even with incident light upon the *ab* crystal facet, due to the experimental artefact of a microscope objective with a non-zero numerical aperture ($NA = 0.15$). In Section 6.3, we use this absorption coefficient spectrum to estimate the density of absorbed photons and the internal photo-gating quantum efficiency (PGQE) of rubrene-graphene phototransistors.

Polarized Raman spectroscopy[138–140] was used as a final tool to confirm the crystallographic orientation and structural quality of the rubrene single crystals in our transistor devices. For these measurements, we used an excitation wavelength of $\lambda = 633nm$ in order to avoid strong fluorescence from rubrene and allow the signatures of normal Raman scattering processes to be resolved. Raman spectra were recorded from the rubrene-graphene interface under two polarization configurations, one with the electric field vector of both incident and backscattered light rays parallel to the long edge of the crystal surface and the other with rays polarized parallel to the short edge. With incident and analyzed light polarized in the same plane, only phonon modes associated with diagonal terms in the polarizability tensor of crystalline rubrene are probed. In rubrene single crystals, which belong to the D_{2h} point group, these polarizability terms produce Raman-active vibrational modes with A_g symmetry.[139] Figures 6.4a and 6.4b show typical spectra collected in short axis and long axis polarisation configurations respectively. In both cases, peaks centred close to $73cm^{-1}$, $105cm^{-1}$, $116cm^{-1}$ and $139cm^{-1}$ were detected, corresponding well with reported A_g symmetry modes.[139] An additional A_g mode positioned around $220cm^{-1}$ is typically very weak and could not be resolved by our experimental set-up. Crucially, no significant peaks were recorded within the $85cm^{-1} < \Delta\omega < 90cm^{-1}$ range

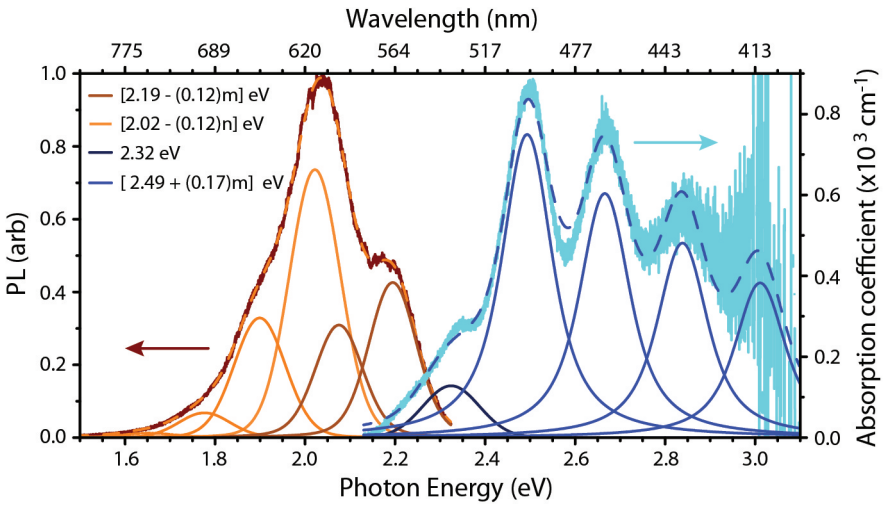

Figure 6.3: Photoluminescence and absorption spectra of rubrene single crystals. Normalised photoluminescence (maroon) emitted from a 202nm-thick rubrene crystal laminated on CVD graphene. Excitation wavelength, $\lambda = 532nm$. The absorption coefficient (blue) was calculated from reflectance and transmittance measurements of a $1.6\mu m$-thick rubrene crystal on a glass substrate. The superposition (dashed lines) of two series of equidistant Voigt profiles (solid lines) are fit to each spectra. Legend: peak positions in each series, where $m, n = 0, 1, 2$,etc.

corresponding to B_{1g}, B_{2g} and B_{3g} symmetry modes which dominate the spectra of disordered rubrene samples. The peaks centred close to $73cm^{-1}$ and $116cm^{-1}$ are associated with non-local electron-phonon coupling (Peierls coupling)[140] which is strongest along the b-axis of rubrene crystals where the transfer integral between neighbouring molecules is largest. Hence, the enhancement of these two peaks in Figure 6.4b relative to Figure 6.4a indicates that the short and long edges of the rubrene crystal surface align with the a and b axes respectively, thereby completing the experimental picture of crystallographic orientation within our samples. We recorded similar spectra at various positions along the length of the rubrene-graphene interface, shown in Figure 6.4c, for both short edge (aa, Figure 6.4d) and long edge (bb, Figure 6.4e) polarization to demonstrate the long-range crystallographic order present throughout rubrene and the absence of randomly oriented grains. Similarly, Figure 6.4e shows that spectra recorded at darker patches of the interface, shown in the inset micrograph, display the same characteristic Raman peaks. There was no evidence to indicate that these regions represent disorder within rubrene. Instead, these dark patches were found to coincide with microscopic residues of PMMA located on top of graphene and underneath the rubrene crystal.

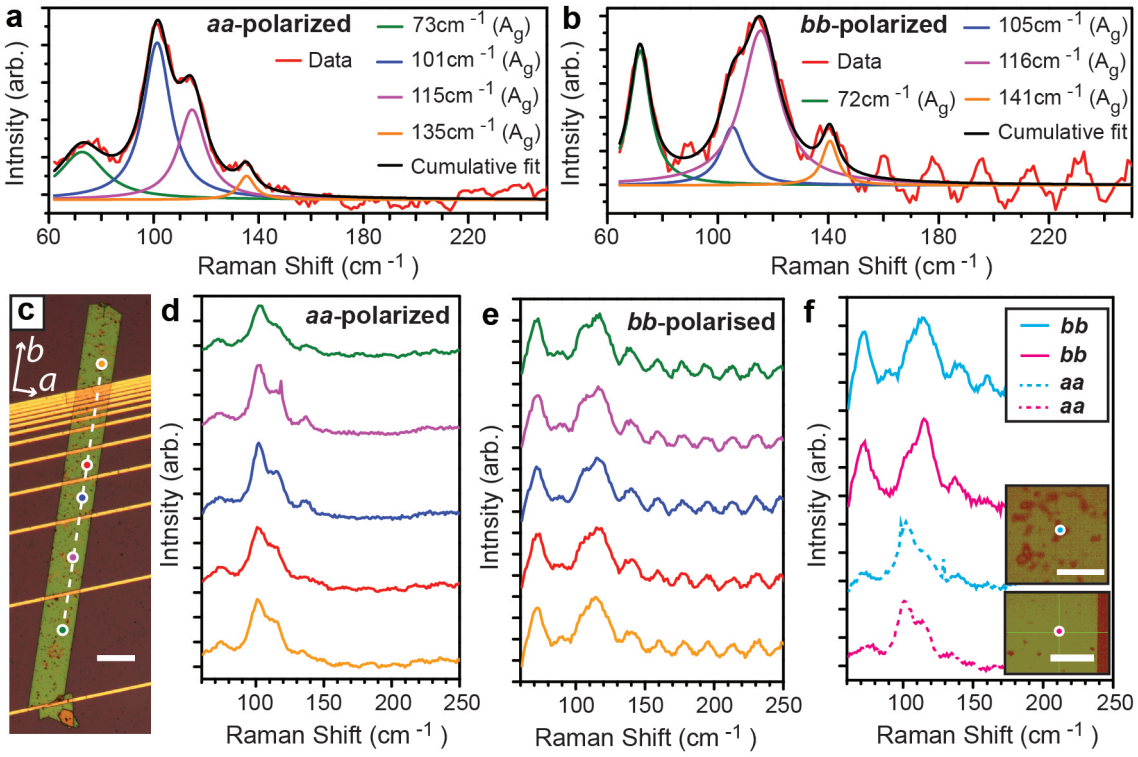

Figure 6.4: Polarized Raman spectra of a rubrene-graphene interface. Lorenztian peaks are fitted to spectra taken with the electric field of incident and analyzed light rays polarised along the **a)** short edge (*aa*-polarized) and **b)** long edge (*bb*-polarized) of the crystal surface. **c)** Micrograph image of a rubrene-graphene interface (scale bar= $200\mu m$). Arrows denote the crystallographic axes of the surface plane and circles mark locations where Raman spectra were recorded ($\lambda_{ex} = 637nm$) under **d)** *aa*- and **e)** *bb*-polarization configurations. **f)** Polarized Raman spectra recorded at locations on the same rubrene crystal with (blue) and without (pink) underlying PMMA residue. Inset scale bars= $20\mu m$.

Charge transport measurements

The circuit configuration used for photocurrent measurements of rubrene-graphene phototransistors is shown in Figure 6.2g, where any neighbouring pair of Au contacts incrementally spaced along the channel can be used as a source or drain electrode. For short channel segments with high conductance, Cr/Au leads and Au/graphene contact interfaces significantly contribute to the total circuit resistance and it is therefore necessary to ascertain what fraction of the applied source-drain voltage (V_{DS}) actually drops across the graphene channel (V_{ch}). To this end, the two-probe and four-probe resistance of each channel segment was measured in constant current configuration using the AC output (V_{osc}) of a lock-in amplifier and a ballast resistor ($R_B >> R_{ch}$) in series (see Figure 6.5a). In both configurations, the equation $R_{(2,4)P} = V_{(2,4)P}R_B/V_{osc}$ is valid. From Ohm's Law, the fraction of applied source-drain voltage dropping across the channel may be calculated using

$$\frac{V_{ch}}{V_{DS}} = \frac{R_{4P}}{R_{2P}} = \left(1 + \frac{2\langle R_C\rangle W}{\rho L}\right)^{-1} \tag{6.2}$$

where ρ is the resistivity of graphene and $\langle R_C\rangle$ is the average contact resistance of each source/drain electrode. The measured values of V_{ch}/V_{DS} are plotted in Figure 6.5b, where the dependence on channel length is found to be in good agreement with Equation (6.2). The significant discrepancy between V_{DS} and V_{ch} for short channels was taken into account for all subsequent calculations of photocondctive gain and quantum efficiencies in this chapter. In a similar fashion, Figure 6.5c details the DC measurement configuration used to ascertain the field-effect mobility of each rubrene-graphene channel segment, with measured values plotted as a function of channel length in Figure 6.5d. The average charge carrier mobility across all channels, $\langle\mu\rangle = 1100cm^2V^{-1}s^{-1}$, is typical of CVD graphene on SiO_2[84,89] and suggests that the HF substrate treatment process shown in Figure 3.4 does not critically degrade charge transport within these transistors. The comparatively low charge carrier mobility across $75\mu m$ and $100\mu m$-long channels was attributed to the increased probability of non-uniform doping and film disorder over larger channel areas.

Measurement conditions

For all photocurrent measurements in this chapter, phototransistor devices were housed in a vacuum chamber probe station with a fused silica viewport at a pressure of $10^{-3}mbar$. The transmittance spectrum of the viewport was measured and accounted for in all calculations of incident optical power. A xenon lamp and monochromator with variable low-pass filters (Newport TLS300X) provided spectrally tunable, un-polarized, collimated light incident over the entire sample. We adjusted optical power levels using a series of

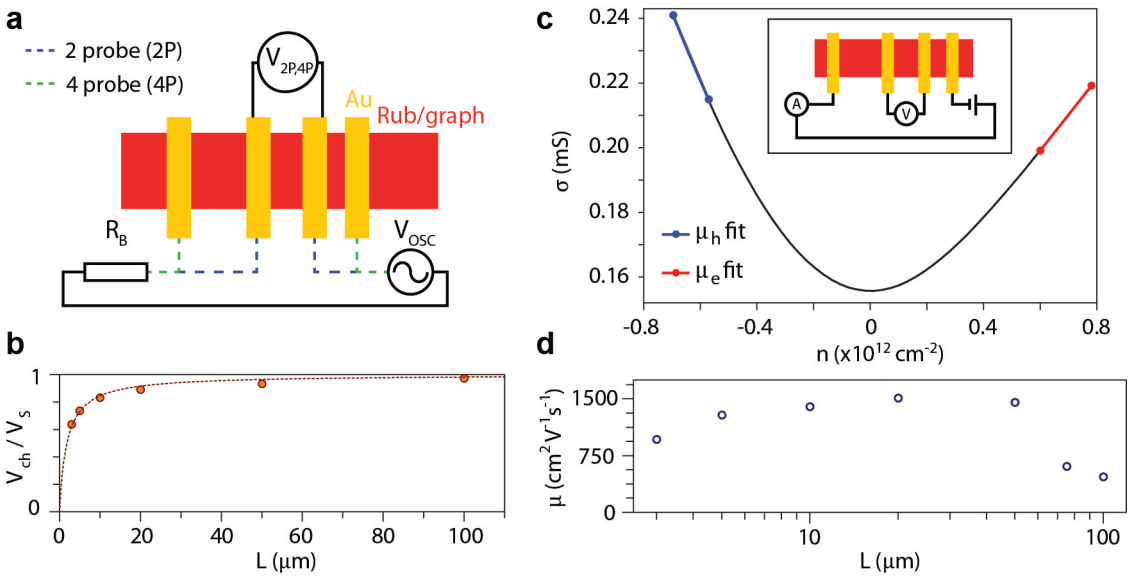

Figure 6.5: Electrical characterisation of a rubrene-graphene interface. **a)** Schematic of two probe (2P) and four probe (4P) circuit configurations used for contact resistance measurements in **b)** which plots the fraction of applied source-drain voltage to fall across the each channel segment. Dashed line fitting function: $V_{ch}/V_{DS} = 1/(1+c_1/L)$, where c_1 is a constant. **c)** Conductivity as a function of charge carrier concentration for a rubrene-graphene channel segment. Inset: Four probe DC circuit configuration used for conductivity measurements. **d)** Charge carrier mobility as a function of channel segment length.

neutral density filters. A mechanical shutter (Thorlabs SHB1T) modulated light signals and power densities were calibrated using a photodiode (Thorlabs S130CV) before and after each data-set run. Excluding spectral scans, an excitation wavelength of $\lambda = 500$nm was used for all photocurrent measurements. PL spectra were excited in atmospheric conditions using a continuous wave $\lambda = 532$nm laser focused through a microscope objective (numerical aperture, $NA = 0.5$). The power density of of the focused laser spot was kept below 100Wm^{-2} during PL measurements in order to avoid photo-oxidation of rubrene crystals.[141]

6.3 Results

Photoluminescence measurements

Figure 6.6 shows PL spectra measured at two locations on a rubrene single crystal, one with and one without an underlying sheet of graphene. Comparing the two spectra, the presence of graphene underneath rubrene causes a broadband reduction in the measured PL intensity of approximately 25%. It follows that non-radiative pathways, such as exciton dissociation and charge transfer, are available to photo-excited charge carriers in rubrene when graphene is in direct contact with the crystal surface. However, exciton dissociation at the rubrene-graphene interface is not the only process which could explain PL quenching. Förster resonance energy transfer (FRET) from rubrene to graphene is another potential mechanism[81,142] but it is often overlooked when discussing PL quenching in semiconductor-graphene heterostructures.[32,37,42] In the case of FRET, electron-hole pairs are excited within graphene, which acts as a broadband antenna for fluorescence from rubrene molecules. The population of 'hot' charge carriers created by this effect could drift under the electric field applied between source and drain electrodes, diffuse according to lateral variations in Seebeck coefficient or transfer heat to the lattice via inelastic scattering with phonons.[71] All three of these processes could result in measurable photocurrent signals but none would be as large as photo-gating effects due to the absence of any significant gain mechanism. In order to identify the relevant dynamics of photo-excited charge carriers in rubrene-graphene interfaces, it was therefore necessary to carefully examine the electrical response of semiconductor-graphene interfaces to incident light signals.

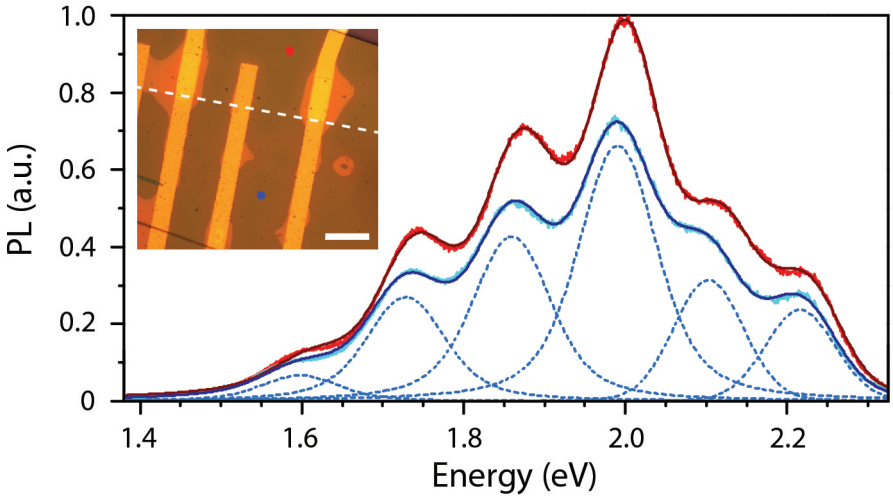

Figure 6.6: Photoluminescence quenching at a rubrene-graphene interface Photoluminescence spectra measured at regions with (blue) and without (red) an underlying graphene film. Dashed Voigt function peaks are fit to the rubrene-graphene spectrum. Inset: Micrograph picture of the interface. Circles and dashes denote the positions of each measurement and the border between rubrene/rubrene-graphene regions respectively. Scale bar = $25\mu m$.

Photocurrent measurements

Figure 6.7 displays the photocurrent measured from a rubrene-graphene channel segment as a function of applied source-drain voltage for a range of incident optical power densities (P). Photocurrent signals were found to vary linearly with V_{DS}. This linearity is expected for systems exhibiting photoconductive gain ($G \propto V_{DS}$ from Equation (2.47)). For a source-drain bias voltage of $30mV$ and a measured field-effect mobility of $1300cm^2V^{-1}s^{-1}$ (see Figure 6.5d), we estimate the transit time taken for charge carriers to drift across the $5\mu m$ long interface channel using Equation (2.47) to be $\tau_{tr} = 10ns$. In Figure 6.8a, transfer curves of the same channel were measured under a variety of optical power densities. Here, the gate voltage was modulated by applying square voltage pulses of alternating polarity about $V_G = 0V$ with a duty cycle of 1% in order to negate minor drifts in channel conductance caused by hysteresis rather than the effects of illumination.[143,144] In all cases, charge transport along the interface is clearly dominated by the ambipolar behaviour of monolayer graphene and illumination induces an up-shift of the gate voltage required to reach the charge neutrality point (ΔV_{CNP}). This up-shift is indicative of exciton dissociation and charge transfer at the rubrene-graphene interface, with holes migrating from rubrene into graphene whilst electrons remain confined to the rubrene crystal.[29] Other mechanisms of photocurrent, such as those caused by FRET to graphene, do not produce this p-doping effect. This is best exemplified by the dependence of photocurrent

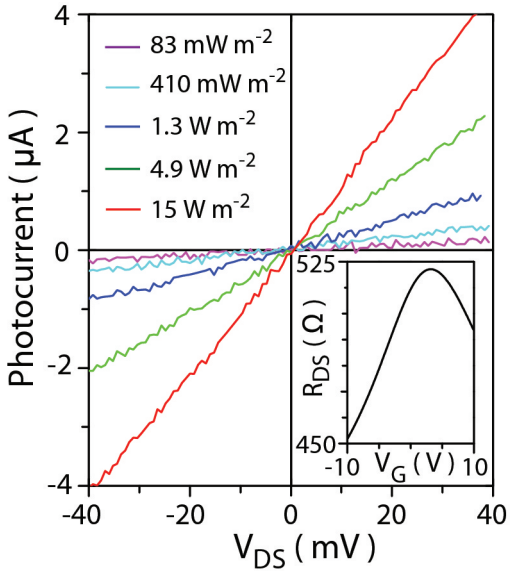

Figure 6.7: Photocurrent from a rubrene-graphene interface. Photocurrent signals produced under various optical power densities are shown as a function of source-drain voltage. ($V_G = 0V$). Inset: A transfer curve of the channel in dark conditions.

on gate voltage, shown in Figure 6.8b. If photocurrent signals were created by electron-hole pairs excited in graphene, a three-fold polarity change signifying the competing effects of field assisted extraction of hot carriers and heat exchange to lattice phonons would be observed around the charge neutrality point.[71] Instead, we find a two-fold polarity change with the magnitude of I_{ph} saturating away from the charge neutrality point, where the local density of states in graphene is the same in both dark and light conditions. As a result, the sensitivity of these interfaces to light is tunable with applied gate voltage and we observe responsivity as large as $1.4 \times 10^5 AW^{-1}$ (Figure 6.8c) and $EQE = 3.4 \times 10^7\%$ under light levels equivalent as weak as $26mWm^{-2}$. Lower responsivity was measured under illumination with successively brighter light signals. This is due to a reduction in PGQE as the density of photo-excited charge carriers in rubrene increases, shown in Figure 6.9 where ΔV_{CNP} saturates for $P_{dens} > 5Wm^{-2}$.

In order to determine the photo-conductive gain in photocurrent signals measured from this rubrene-graphene interface, we focused on the transient response to weak light signals, where $P < 300\mu Wm^{-2}$, in the inset of Figure 6.9. Whilst the rise time of the detector is relatively fast, taking approximately $100ms$ to reach steady-state current under illumination, the transition back to dark current levels lasts for tens of seconds and is indicative of the average lifetime of electrons localized in rubrene.[29] The photocurrent after illumination was fit with a bi-exponential decay function (pink dashed line), suggesting that at least two distinct lifetimes exist for photo-excited electrons in rubrene.[43] Taking a weighted average of the two decay constants, we calculate an average lifetime of $\tau_L = 24 \pm 3$

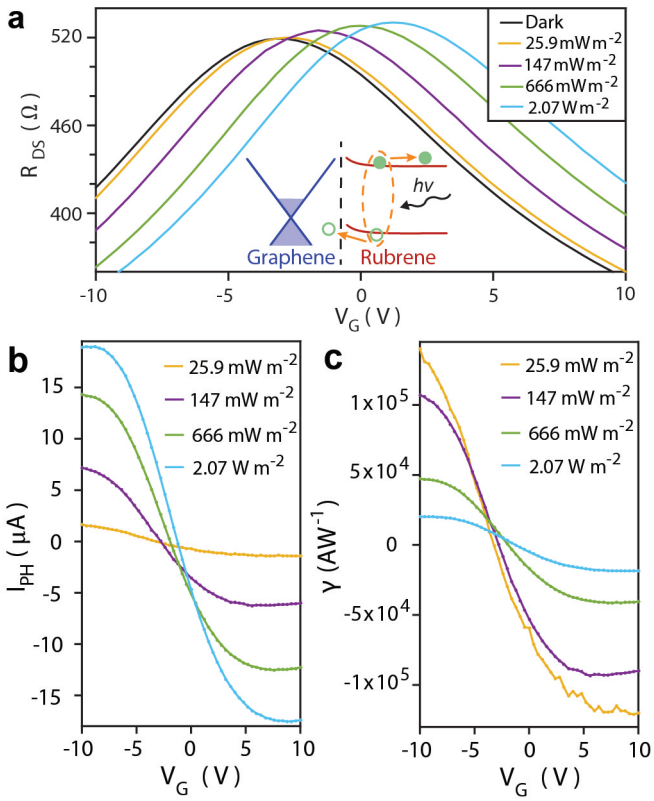

Figure 6.8: Charge transfer at a rubrene-graphene interface. a) Channel resistance, **b)** photocurrent and **c)** responsivity of a rubrene single crystal-graphene transistor as a function of gate voltage under various optical power densities listed in the legends.

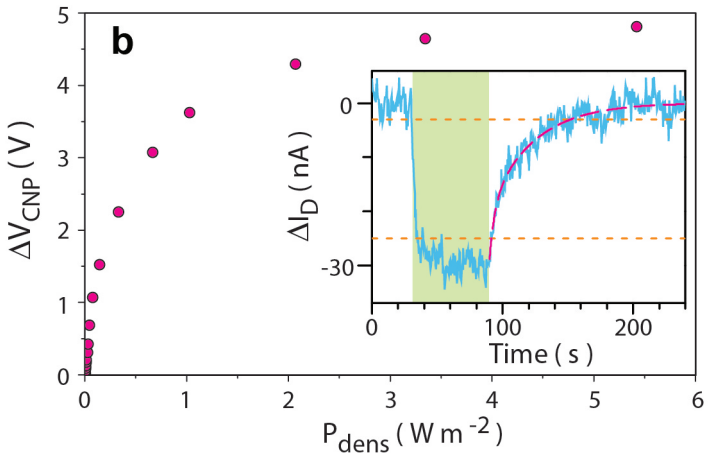

Figure 6.9: Saturation of photo-gating under stronger light intensity. The shift in gate voltage required to reach charge neutrality compared to dark conditions is plotted as a function of optical power density. **Inset:** A 20-run average of the transient photo-response from a $5\mu m$ rubrene-graphene channel to 60 seconds of illumination ($63.2\mu W m^{-2}$). Dashed lines mark 10% and 90% of the change in steady state current (orange) and a bi-exponential decay fit of the return to dark conditions (pink).

seconds and a photo-conductive gain of $G \approx 10^9$ using Equation (2.45).

Having established the magnitude of photoconductive gain from the rubrene-graphene phototransistor, the external and internal PGQE remained to be calculated. In order to assess the internal PGQE, it was necessary to first establish the efficiency of light absorption in the rubrene crystals used in our devices. Figures 6.10a and 6.10b illustrate the two device structures we considered. Device A is a 405nm-thick rubrene crystal laminated on an SiO_2/Si substrate, whilst Device B is the 202nm-thick crystal laminated on monolayer graphene/SiO_2/Si used in all of the photocurrent measurements discussed so far in this chapter. The absorbance of the rubrene single crystal in each device was simulated using the experimentally measured absorption coefficient spectrum of rubrene (shown in Figure 6.3) and simulations of the substrate reflections using thin film analysis software (TFCalc, Software Spectra Inc). A dispersion of the complex refractive index of each constituent material (rubrene,[137] graphene,[145] SiO_2[146] and Si[147]) was selected from published studies in order to calculate the substrate reflectance of each device. The methodology used in each of these studies was density functional theory,[137] ellipsometry[145] and spectrophotometry.[146,147] Each dispersion was substituted into a matrix formulation of the Fresnel equations which describe reflectance and transmittance at each thin film interface and the absorbance of each substrate material[148,149] (see Appendix A for full details). Semi-infinite initial and final media of rubrene and Si were assumed respectively, whilst the thickness of all other layers in the simulation correspond to the annotations in Figures 6.10a and 6.10b.

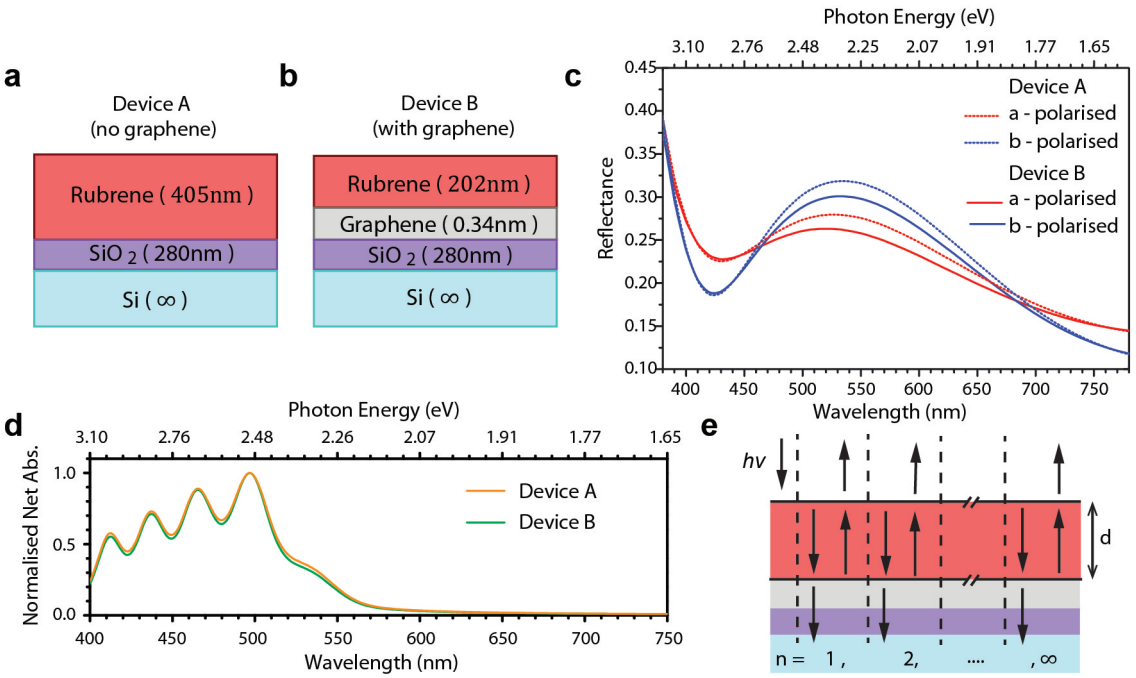

Figure 6.10: Simulations of absorbance in rubrene single crystals. Schematics show the thin film order of the constituent materials in **a)** rubrene (Device A) and **b)** rubrene-graphene (Device B) transistors. **c)** Simulated reflectance spectra of the multilayer thin-film stack underneath rubrene in Devices A (dashes) and B (solid lines) for incident light polarised along the a and b axes of rubrene crystals. **d)** Absorbance spectra of un-polarised light normal to the ab facet of rubrene crystals in Devices A and B. Spectra are normalised to the maximum of each data set. **e)** Schematic detailing the iterative internal reflections within the rubrene crystals which were considered in absorbance calculations.

Calculated reflectance spectra for light at normal incidence to the substrates of devices A (dashes) and B (solid lines) are shown in Figure 6.10c. The birefringent nature of rubrene single crystals was accounted for by calculating the reflectance of light polarised along the a (red) and b (blue) crystal axes separately. An average of these spectra was then used to match the un-polarised light source in our experimental set-up.

The absorbance (A_{rub}) of the rubrene crystals in Devices A and B were calculated assuming a satisfactorily high order ($n > 4$) of internal reflections at the vacuum-rubrene and rubrene-substrate interfaces (with reflectance of R_1 and R_2 respectively) using the following series:

$$A_{\lambda\, rub} = (1 - R_1)\left[1 - e^{-\alpha d}\right]\left\{1 + \sum_{n=1}^{\infty}\left[{R_1}^n {R_2}^n + {R_1}^{(n-1)} {R_2}^n\right]\right\} \tag{6.3}$$

Here, α is the absorption coefficient of rubrene single crystals shown for light polarised in the ab plane and d is the crystal thickness. Interference effects were not found to be significant in photocurrent spectra produced by incoherent light sources, hence phase

terms have been omitted. Using Equation (6.3), we plot the absorbance of both rubrene crystals normalized to their maxima in Figure 6.10d. A diagram of the iterative reflections considered in Equation (6.3) is shown in Figure 6.10e for the sake of clarity. The normalized spectra follow almost exactly the same profile, indicating that differences in substrate reflectance between Devices A and B do not cause any notable difference in the spectral dependence of light absorption in each rubrene crystal.

In Figure 6.11a, the responsivity spectra of three transistors with channels consisting of different material combinations - rubrene (Device A from Figure 6.10a); rubrene-graphene (Device B from Figure 6.10b); and graphene - are compared. All devices were illuminated under the same optical power density ($P \approx 10mWm^{-2}$), source-drain voltage ($V_{DS} = 30mV$) and gate voltage ($V_G = 0V$). Channel dimensions were kept as consistent as possible amongst all devices ($L = 5\mu m, W = 90-100\mu m$) with minor variations in channel width arising due to differences in the size of selected rubrene crystals. The rubrene transistor was treated with the same Ar plasma used to remove unwanted graphene from the rubrene-graphene and graphene devices. By keeping these factors consistent, the three responsivity spectra shown in Figure 6.11a could be compared in order to elucidate which materials dominate light absorption relevant to photocurrent signals in rubrene-graphene interfaces. From Figure 6.11a, the rubrene-graphene transistor exhibits a radically enhanced responsivity compared to the two transistors that are each comprised of just one channel material. The negligible responsivity of the rubrene transistor indicates that the surface conductivity of rubrene single crystals[83] does not significantly contribute towards photocurrent signals in hybrid devices. Furthermore, the similarly negligible responsivity of the graphene transistor suggests that photo-excited electrons are not trapped by surface states such as silanol groups in the SiO_2 substrate or microscopic PMMA residues on graphene. If this were the case, broadband responsivity of a similar magnitude to the rubrene-graphene device would be expected from graphene, given that photo-excited electrons be trapped and produce significant photo-conductive gain. Instead, the absence of this effect suggests that either trap states unique to the rubrene crystal surface or a Schottky barrier at the rubrene-graphene interface are responsible for localizing photo-excited electrons. Figure 6.11b displays the responsivity spectra of rubrene and rubrene-graphene transistors normalized to the maximum of each dataset. This allows the spectral selectivity of each device to be compared. The two transistors show very similar spectral profiles, each with a maximum at $\lambda = 500nm$ and cut-off for wavelengths longer than $580nm$. Peaks in responsivity correlate well with the simulated absorbance spectra of the rubrene crystals in each device (dashed lines). It follows that photocurrent signals in the rubrene-graphene interface results from the absorption of light in the rubrene single crystal rather

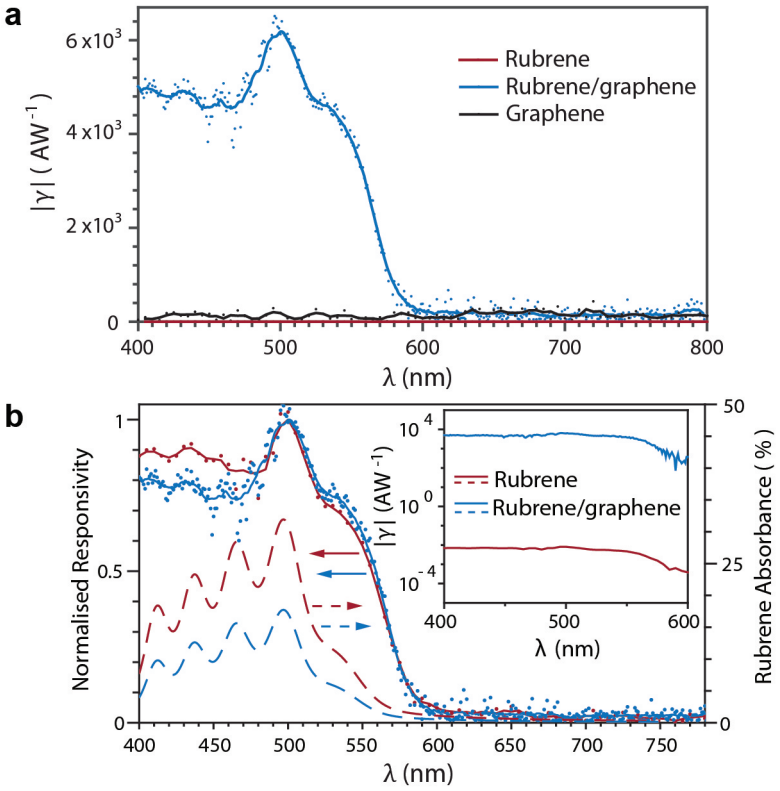

Figure 6.11: Responsivity spectra of rubrene-graphene phototransistors a) Responsivity spectra of rubrene, graphene and rubrene-graphene photodetectors with approximately equal channel dimensions ($L = 5\mu m$, $W = 90 - 100\mu m$). Measured data (dots) is smoothed using adjacent averaging over a 15nm range (solid lines). **b)** Responsivity spectra of rubrene and rubrene-graphene transistors normalized to the maximum of each data-set (main figure) and on a logarithmic scale (inset). Dashed lines show the simulated absorbance of rubrene in each device.

than graphene.

Channel geometry is a significant but extraneous factor that is largely responsible for dramatic variations in responsivity amongst previously reported graphene-based phototransistors.[29,31,33–44] Indeed, a proportionality of $\gamma \propto G\eta_{PG} \propto L^{-2}$ is expected, given that $G \propto L^{-2}$ whilst η_{PG} is independent of channel length. However, large lateral electric fields and possible exciton quenching effects at metallic source/drain electrodes could significantly affect the PGQE in shorter channels. To exclude these spurious effects, we have conducted for the first time a scaling experiment of responsivity as a function of channel length in Figure 6.12. In Figure 6.12a, the absolute responsivity measured at various rubrene-graphene interface segments ('Device B') follows an approximately linear dependence upon L^{-2}. However, the fractional residual of this fit (lower inset) shows data to deviate from a $\gamma \propto L^{-2}$ dependence by more than the uncertainty of each experimental reading. In Figure 6.12b, we find that this deviation can be eliminated by instead

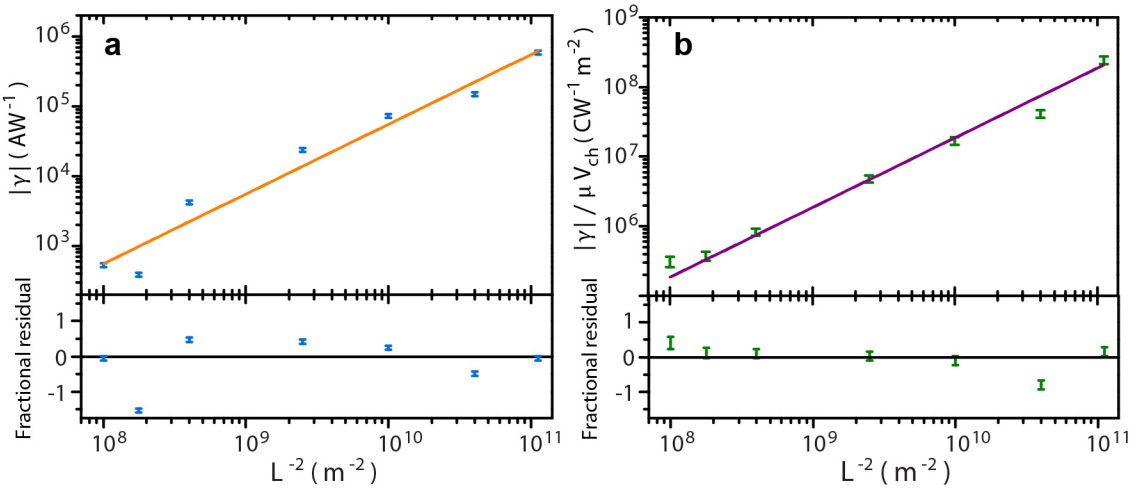

Figure 6.12: Length scaling of responsivity. Upper plots show the magnitude of photoresponse as a function of the reciprocal of the channel length squared. **a)** before and **b)** after normalizing the responsivity to the voltage drop across each channel and the mobility of charge carriers. Lower plots show the fractional residual of linear fits to each dataset (dashed lines).

considering $|\gamma|/\mu V_{ch}$ as the dependent variable. This normalizes the responsivity of each channel segment to the charge carrier mobility and potential difference across it, both of which vary due to non-zero contact resistance and variations in the quality of transferred graphene films over large areas shown in Figures 6.5b and 6.5d. Following this correction, a linear proportionality between responsivity and L^{-2} is evident. This finding validates our assumption that the active area of a rubrene-graphene phototransistor comprises the whole interface area contained between source and drain electrodes. Furthermore, Figure 6.12b demonstrates that a more meaningful comparison between the responsivity and EQE of differently shaped graphene-based phototransistors can be achieved by accounting for the inverse square dependence on channel length, provided the PGQE is independent of L in each device.

In Figure 6.13a, we test the operational speed limits of a rubrene single crystal-graphene phototransistor. The blue line plot shows photocurrent generated in a device with light modulated at a frequency of $0.5Hz$ and an applied gate voltage of $V_G = 10V$, such that the Fermi level of graphene lies within the conduction band. Over successive cycles of illumination, the fall time of the phototransistor, set by the lifetime of electrons localized in rubrene, is too slow to reach steady-state in dark conditions. The red line plot shows photocurrent generated in the same device but with a negative voltage pulse of $\Delta V_G = -10V$ applied to the gate electrode (orange line plot) whenever the light source is extinguished. The operational speed of the phototransistor is notably faster (red line

plot) and more stable. Evidently, the negative gate voltage pulse momentarily increases the recombination rate of photo-excited electrons in rubrene allowing the device to reset quickly in dark conditions. Rudimentary band diagrams detailing the transfer of photo-excited charge carriers at each stage of an illumination cycle are illustrated in Figure 6.13b. Whilst the depicted movement of charge carriers is directly supported by experimental evidence, the degree of band bending shown at the rubrene-graphene interface is speculative in the absence of further experimental information regarding the density of surface states within the band gap of rubrene that would determine the exact nature of any Schottky barrier.[150] Nevertheless, using this gate voltage pulsing strategy we were able to extend the operational bandwidth of the rubrene-graphene phototransistor. This is shown in Figure 6.13c, where device responsivity remains above the $-3dB$ threshold up to at least $1.5Hz$. Figure 6.13d displays the Fourier transform of a 360 second trace of the dark current flowing across the same rubrene-graphene channel ($V_{DS} = 40mV$) recorded with a sampling rate of 600μs. The noise follows a $1/f$ dependence typical of graphene at frequencies below $10kHz$.[55] Given this dependence, the improvement in operational speed achieved using the gate voltage pulsing strategy is especially advantageous, as it allows the phototransistor to be operated in a frequency range with a lower noise spectral density (S_n). Extrapolating from f_{BW}=1.5Hz in Figure 6.13d, we find $S_n^2 = 1 \times 10^{-16} A^2 Hz^{-1}$.

As previously mentioned, the PGQE of the rubrene-graphene phototransistor increases at lower absorbed photon densities. In Figure 6.14, we explore the limit of this effect by measuring the non-linear power dependence of responsivity with the interface exposed to ultra-weak light signals ($P < 3mWm^{-2}$). A maximum of $\gamma = 1 \times 10^7 AW^{-1}$ was reached for the lowest measured optical power densities. This marks the first report of responsivity comparable to the record room-temperature performance of inorganic semiconductor-graphene phototransistors[29,38] from an entirely organic equivalent. Analogous to previous phototransistor studies,[29,36,38] we fit this non-linear power dependence with the function

$$\gamma = \frac{\gamma_{max}}{1 + (P/P_0)^n} \tag{6.4}$$

where P_0 marks a threshold power density above which the exponent n dictates the rate of decline in responsivity. Taking a best fit of Equation (6.3) (blue dashed line), we find $P_0 \approx 1.1\mu Wm^{-2}$ and $n = 0.70 \pm 0.04$. Re-arranging the expanded expression for responsivity, $\gamma = (e\eta_{PG}/hv) \cdot \left(\mu\tau_L V_{DS}/L^{-2}\right)$, we were then able to calculate the PGQE (blue data) shown on the right y-axis in Figure 6.14. The simulated absorbance of the rubrene crystal, shown in Figure 6.11b, was then used to calculate the internal photo-gating quantum efficiency as $\eta_{iPG} = \eta_{PG}/A_{\lambda rub}$ (orange data). For power densities equivalent to sub-femtowatt signals incident on the device active area, $\eta_{PG} \approx 1\%$ and $\eta_{iPG} \approx 5\%$. This value

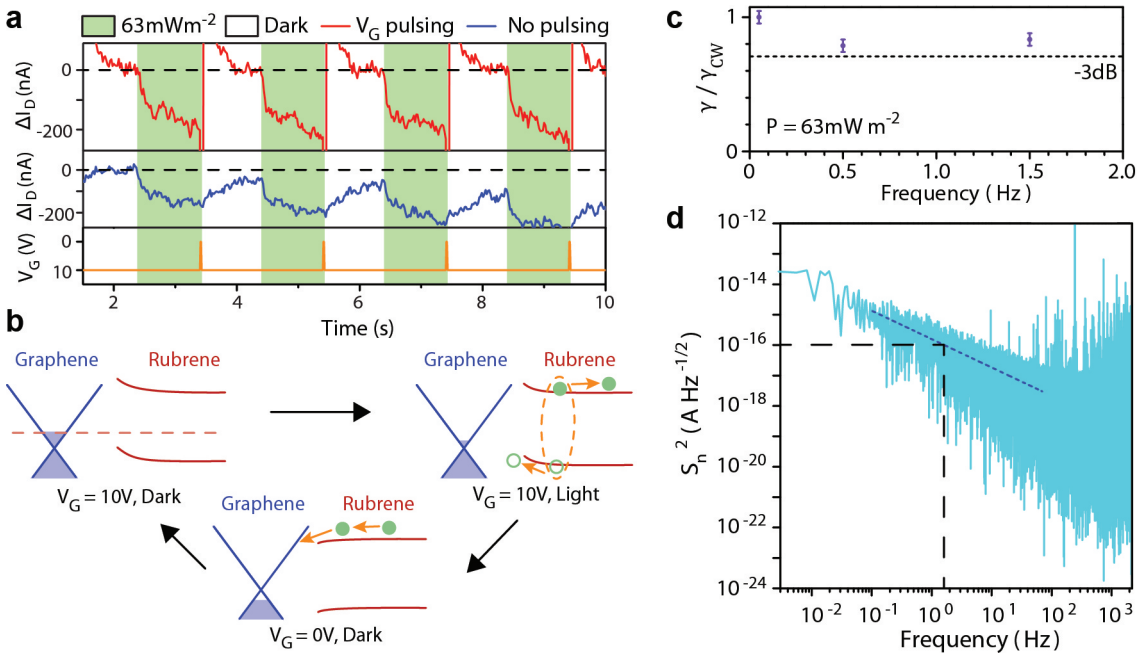

Figure 6.13: Operational speed and 1/f noise. **a)** Time-dependent response of a rubrene-graphene channel to a light signal modulated at $0.5Hz$ ($V_{DS} = 40mV$). Changes in drain current from the steady-state in dark (dashed lines) are shown both with (red) and without (blue) the application of a -10V resetting pulse to the back gate. Current spikes due to gate pulsing are readily removed with filtering circuitry. **b)** Schematic band diagrams illustrating the charge transfer dynamics across a rubrene-graphene interface at each stage of the light modulation cycle.

of PGQE is four orders of magnitude greater than a previous study that combined amorphous films of P3HT[33] with graphene and one order of magnitude higher than epitaxially grown polycrystalline films of C_8-BTBT grown on graphene.[34] We attribute the superior PGQE in rubrene-graphene interfaces to a combination of two factors. Firstly, a rubrene single crystal should, in principle, serve as an ideal light-absorbing layer in graphene phototransistors due to the extremely low density of charge traps in the bulk of the crystal[151] and the significant inter-molecular overlap of π-orbitals which facilitates Dexter-type diffusion of triplet excitons over several microns.[77,83,152] In comparison to other organic semiconductors where molecular ordering is less optimal, a far larger number of excitons should therefore able to diffuse to the graphene interface and dissociate. Secondly, this is the first study to examine the PGQE of organic semiconductor-graphene phototransistors at extremely low absorbed photon densities where bimolecular recombination and triplet-triplet fusion are not significant loss mechanisms.[83] We suspect that previous groups did not report the photo-response of organic semiconductor-graphene phototransistors in this regime because of the electrical noise floor set by either measurement apparatus or inappropriate design of device geometry. Using the noise spectral density determined from Figure 6.13d, we calculated a minimum resolvable photocurrent of $I_n = S_n\sqrt{\Delta n} = 10nA$ for a light modulation frequency of $f_{BW} = 1.5Hz$ and a noise bandwidth of $\Delta f = 1Hz$. We then numerically solved Equation (6.3) to determine the noise equivalent power density and responsivity at the noise floor of the rubrene-graphene phototransistor. Values of $NEP/WL = (5.0\pm2.4)\times10^{-6}Wm^{-2}$ and $\gamma_{NEP} = I_n/NEP = (4.3\pm2.1)\times10^{6}AW^{-1}$ were found respectively. Finally, for an active area of $91\mu m \times 5\mu m$, we calculated a maximum specific detectivity of $D^* = \sqrt{A\cdot\Delta f}/NEP = (9.2\pm4.5)\times10^{11}cmHz^{1/2}W^{-1}(Jones)$ under practical measurements conditions (i.e. without averaging photocurrent signals over multiple modulation cycles). This falls within the range of specific detectivity offered by commercially available silicon photodiodes.

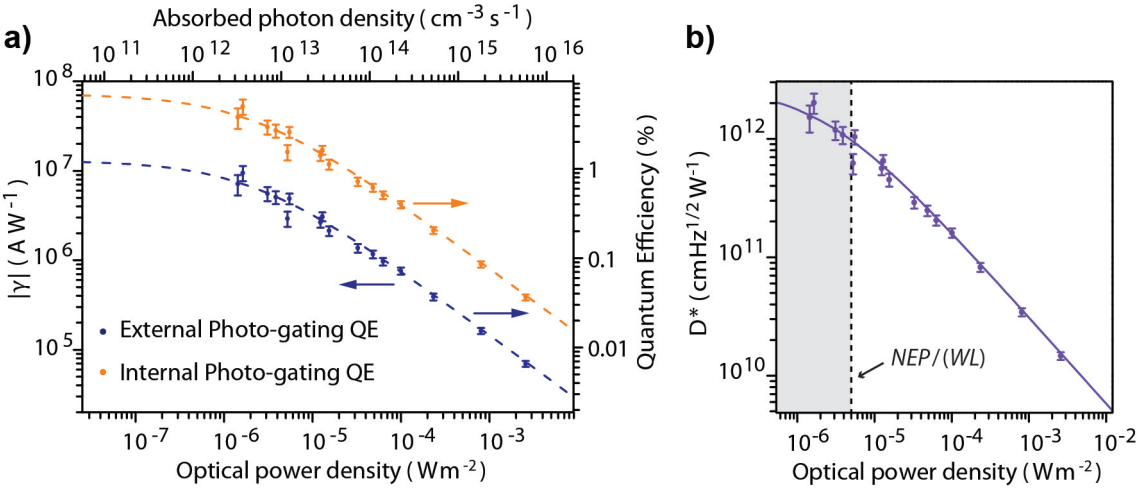

Figure 6.14: PGQE and Specific Detectivity. $V_{DS} = 40mV$ and $V_G = 0V$. **a)** Absolute responsivity as a function of incident optical power (blue points, left y-axis) determined from the averaged response of a $5\mu m$ rubrene-graphene channel to 20 illumination cycles. External (blue points, right y-axis) and internal (orange points, right y-axis) photo-gating quantum efficiencies are calculated from the same data-set. **b)** The power-dependence of specific detectivity calculated from the same data-set. Dashes indicate the noise floor of the device for $\Delta f = 1Hz$ and $f_{BW} = 1.5Hz$.

Comparative study of graphene-based phototransistors

From analysis of the photocurrent measurements shown above, we have reported a multitude of figures of merit for the rubrene-graphene phototransistor examined in this chapter. These include responsivity, specific detectivity, operational bandwidth, photo-conductive gain, EQE, external PGQE and internal PGQE. All of these values are compiled in Table 6.1 with any power-dependent terms stated at the noise spectral power density, $P = NEP/WL$. To the best of our knowledge, this represents the most comprehensive characterisation of a graphene-based phototransistor reported to date. Following this, it is essential that the performance of this device be assessed relative to that of phototransistors comprised of alternative photo-active layers using the most appropriate figures of merit. A common procedure used in comparative studies of phototransistors or photoconductors is to plot the specific detectivity of each device as a function of operational bandwidth. Applying this to graphene-based phototransistors, the most appropriate semiconductor-graphene phototransistor for a particular application should display the highest specific detectivity of any device that meets the desired spectral range and operational bandwidth. Unfortunately, as shown in Table 6.2, only a small fraction of relevant studies[29,32,40,42] report values of D^* and even fewer[29,40] provide data to support the value of noise-equivalent power used in calculations. The operational bandwidth is also rarely explicitly stated[29]

Operational Bandwidth f_{BW} (Hz)	**Noise Equivalent Power NEP (W)**	**Responsivity γ (A/W)**	**External Quantum Efficiency η_{EQE} (%)**
1.5	$(2.3 \pm 1.1) \times 10^{-15}$	$(4.3 \pm 2.1) \times 10^{6}$	$(1.1 \pm 0.5) \times 10^{9}$
Specific Detectivity D^* (Jones)	**Photo-conductive Gain G**	**External PGQE η_{PG} (%)**	**Internal PGQE η_{iPG} (%)**
$(9.2 \pm 4.5) \times 10^{11}$	$(2.6 \pm 0.3) \times 10^{9}$	$(0.42 \pm 0.25)\%$	$(2.3 \pm 1.4)\%$

Table 6.1: Compiled figures of merit for the rubrene-graphene phototransistor reported in this chapter. Power-dependent terms are stated at the device noise limit, where $P = NEP/WL$ and the noise bandwidth is $\Delta f = 1Hz$).

and has been known to change with incident optical power[43] and substrate material.[33] In the absence of this information we use responsivity, the most commonly reported figure of merit, to form a more substantive comparison between our device and a variety of other light-absorbing layers used in graphene-based phototransistors.

Figure 6.15a plots responsivity as a function of incident optical power for all relevant phototransistor studies with the excitation wavelength used indicated on a colour bar scale. Although we have recorded the highest responsivity for any organic semiconductor-graphene phototransistor, it is difficult to gain accurate insight as to the relative performance of each light-absorbing material. A very wide distribution of responsivity exists between studies which use the same material combinations,[29,35] or even between multiple devices measured in the same study.[33] The primary reason for this is the dependence of responsivity on extraneous parameters such as channel length, applied source-drain voltage and charge carrier mobility in graphene. All of these terms vary significantly amongst studies and influence the magnitude of photo-conductive gain rather than the intrinsic efficiency of each material interface. As a result, we have endeavoured to find a figure of merit that corrects for variations in these extraneous parameters amongst different devices and which may be calculated with variables that are provided in the majority of relevant studies. The term which we have come up with is a 'specific EQE', η^*_{EQE}.

$$\eta^*_{EQE} = \gamma \cdot \frac{hv}{e} \cdot \frac{L^2}{\mu V_{DS}} \tag{6.5}$$

Or, alternatively, $\eta^*_{EQE} = \eta_{PG}\tau_L$. This is simply the external quantum efficiency of a phototransistor normalized to the dependence of photo-conductive gain upon V_{DS}, L and μ. The specific EQE is independent of photo-active area, channel geometry and charge carrier

Ref	**Photo-active material**	λ_{ex} **(nm)**	f_{BW} **(Hz)**	D^* **(Jones)**	**P** (Wm^{-2})	**Evidence of NEP?**
[32]	Poly-crystalline pentacene	520	-	4.5×10^{10}	-	no
[42]	Methylammonium lead halide perovskite	532	$\sim 10^0$	1×10^9	20	no
[29]	Colloidal PbS quantum dots	532	$\sim 10^2$	7×10^{13}	1×10^{-6}	yes
[40]	GaSe nanosheets	532	$\sim 10^2$	1.1×10^{10}	57	yes
This work	Rubrene single crystal	500	$\sim 10^0$	9×10^{11}	5×10^{-6}	yes

Table 6.2: Specific Detectivity of graphene-based phototransistors. Values of D^* are compared for graphene-based phototransistors which use various light absorbing layers. The optical power density and operational bandwidth associated with each value is provided where possible.

lifetime. As a result, we propose that η^*_{EQE} can be used as a substitute for specific detectivity to indicate the optimum material combination amongst multiple phototransistors which meet the spectral range and operational speed required for a particular application.

Figure 6.15b displays the specific EQE of all reported graphene-based phototransistors as a function of incident photon flux. Clearly, the use of η^*_{EQE} rather than γ as a figure of merit significantly reduces the variation amongst different reported devices for a fixed light intensity. We find that phototransistors which exhibit record responsivity values in Figure 6.15a[29,38] have largely been influenced by the use of optimal channel geometries rather than the choice of photo-active material, with η^*_{EQE} of these devices well within the range of most other studies in Figure 6.15b. Similarly, a seven order of magnitude disparity in responsivity between P3HT-graphene phototransistors[33] which use exfoliated graphene flakes on hexagonal boron nitride and others which use CVD graphene on SiO_2 is found to originate almost entirely from extraneous variations in photo-conductive gain. Much of the variation between phototransistor devices that remains once η^*_{EQE} is used as a figure of merit is likely to derive from differences in the absorbance of each semiconductor layer. This is exemplified by the data relating to phototransistors which use chlorophyl-a[43] and C_8-BTBT[34] as light-absorbing materials. In these cases, an increase in the semiconductor layer thickness of just $10nm$ results in a $1-3$ order of magnitude enhancement in η^*_{EQE} with further increases in thickness producing diminishing returns. The thickness and absorption coefficient of the photo-active layer has not been quantified in most of

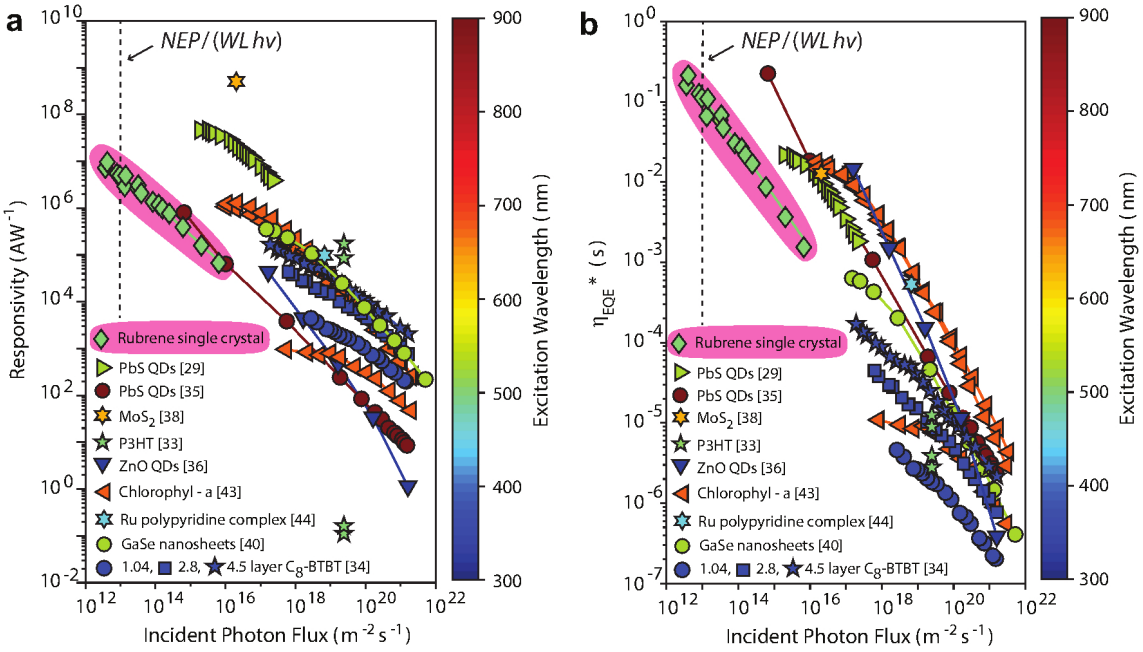

Figure 6.15: Comparative study of graphene-based phototransistors Plots of **a)** the responsivity and **b)** the 'specific EQE' of various graphene-semiconductor interfaces as a function of incident photon flux. Solid lines connect data taken from a single device, marker colours denote the excitation wavelength, pink regions highlight data from and the dashed line indicates the noise floor of the rubrene-graphene phototransistor at $f_{BW} = 1.5Hz$ and $\Delta f = 1Hz$. Legends list the light-absorbing material in each device (see Appendix B for supporting data.[34]

the studies in Figure 6.15b, so we are unable to further modify our figure of merit to account for these effects. Focusing once more on the rubrene-graphene phototransistor, the sub-linear power dependence of η^*_{EQE} extends to extremely low optical powers that are far beyond the limits at which other organic semiconductor-graphene phototransistors plateau at a maximum. The most common explanation for the sub-linear dynamic range of graphene-based phototransistors is that photo-excited free charge carriers localised to the semiconductor occupy the longest-lived deep level trap states in the semiconductor layer. At higher light intensities, all of the deep level trap states become filled and the remaining photo-excited charge carriers instead occupy shorter-lived shallow states leading to a reduction in the average carrier lifetime, τ_L. Hence, both γ and η^*_{EQE} decline with increasing optical power. Assuming this to be true in the case of rubrene-graphene interfaces, the density of long-lived trap states in rubrene available for photo-gating processes can be estimated as $N_t = \eta_{iPG}\tau_L P_0/h\nu \approx 5 \times 10^8 cm^{-2}$. Even if graphene screens an overwhelming proportion of the traps otherwise present at the rubrene-SiO_2 interface ($\sim 10^{12} cm^{-2}$),[151] we suspect that our estimate of N_t is too low to be physically plausible. Alternatively, we note that several a sub-linear dynamic range of photo-response at the surface of rubrene single crystals has previously been attributed to the onset of multi-particle recombination at increased photo-excited charge carrier densities.[83] In particular, a transition from $\gamma \propto P^0$ to $\gamma \propto P^{-2/3}$ due to triplet-charge quenching corresponds well with our fit to Equation (6.3). The onset of these interactions occurs at higher absorbed photon densities ($> 10^{15} cm^{-3} s^{-1}$) in isolated crystals but we suspect that a lower threshold in our device (see Figure 6.14a) could be explained by the additional population of free charge carriers at the crystal surface from physical contact with graphene.

Future research directions

Following on from the conclusions made in this investigation of rubrene single crystal-graphene interfaces and comparative study of graphene-based phototransistors, we have identified several promising directions for future research. Firstly, there is a clear need to eliminate sources of electrical noise in graphene. This can be achieved by integrating high quality single crystal CVD graphene films[153] and metallic electrodes that connect to graphene via one-dimensional side contacts[154] into existing device structures. Secondly, methods should be developed to tailor the density and type of charge traps at the interface between rubrene single crystals and graphene. A deeper understanding of existing surface trap states could be gained through temperature dependent measurement of photocurrent transients, similar to methods used on quantum dot photoconductors.[155] Once identified, procedures could then be developed to eliminate states which trap charge carriers for

longer than $1 - 100ms$, thereby allowing operational bandwidths more appropriate for video imaging applications to be accessed where the noise spectral density is also lower. We have already developed such a technique in a similar study[121] concerning few-layer WS_2-graphene phototransistors, where an inverted device structure and ionic polymer top gate were used to screen long lived traps and detect light at modulation frequencies up to $1.5kHz$. Finally, efforts should be made to minimise multi-particle recombination in rubrene at low absorbed photon densities in order to extend the high PGQE and specific detectivity we report to higher absorbed photon densities. If triplet-charge quenching and Forster resonance energy transfer are indeed enhanced by direct contact of graphene with the rubrene crystal surface, an interface buffer layer could be introduced in an attempt to prevent these effects.[156] If some of these efforts prove successful, it is reasonable to expect that the specific detectivity of rubrene single crystal-graphene phototransistors could be improved by 1-2 orders of magnitude ($D^* = 10^{13-14} AW^{-1}$), approaching that of single photon detectors.

6.4 Conclusions

In conclusion, interfaces of monolayer graphene and rubrene single crystals are promising systems for ultra-sensitive detection of visible light. Effective transfer of photo-generated charges to graphene with an external and internal efficiency of 1% and 5% respectively. Utilising these interfaces as phototransistors, responsivity as high as $10^7 AW^{-1}$ can be achieved for sub-femtowatt incident optical signals, comparable to the record performance of graphene-quantum dot detectors. Finally, we emphasise the importance of distinguishing between the contributions of internal gain, photo-gating quantum efficiency and carrier lifetime towards the responsivity of phototransistors. Following this procedure, accurate conclusions can be made as to which combination of materials warrant further research and how to continue improving the performance of this novel class of high-gain, micro-scale photodetectors.

7

Summary

The aim of this thesis was to investigate how the optical and electronic properties of graphene could be modified to enhance its use in optoelectronic devices. Throughout the previous three chapters, we have presented several examples which show that the electrical and optical properties of graphene can indeed be modified to suit specific device applications.

We demonstrated a first example of this in Chapter 4, where we developed the first method of intercalating large area few-layer graphene with $FeCl_3$. We then implemented these films as transparent electrodes in alternating current electroluminescent devices and polymer light emitting diodes. An analysis of the spatial variation in doping across these films has revealed that measures must be taken in future projects to control the density of grains across CVD few-layer graphene films and to initiate diffusion of $FeCl_3$ into the base bilayer film.

A second example of modifying graphene's properties was presented in Chapter 5. In this study, we found that photo-responsive p-p' junctions could be arbitrarily written into $FeCl_3$-intercalated few-layer graphene by means of optical lithography. These junctions were found to produce photocurrent signals which exhibited a linear dynamic range of $44dB$. This is well suited to radiometry applications in comparison to pristine graphene photodetectors. From theoretical estimates, we concluded that the cooling of hot charge carriers is accelerated in both the p and p' regions. As future work, an extended experiment to better understand the cooling of hot carriers was proposed, whereby an ionic polymer gate could be used to reversibly engineer the p-p' junctions.

In Chapter 6 we provided a third and final example of modifying graphene's optoelectronic properties, where the photo-response of a graphene transistor to weak light signals was enhanced by creating a charge transfer interface with a rubrene single crystal. We found that responsivity and detectivity as high as $10^7 AW^{-1}$ and $9 \times 10^{11} cmW^{-1}Hz^{-1/2}$ could be achieved at the limit of the noise-equivalent power. Important implications for future research of these devices came from a comparative study of graphene phototransis-

tors. This showed that the majority of variations in responsivity amongst reported devices stems from extraneous variations in channel geometry and measurement conditions. In future it is likely that a new consensus is needed as to how these amplified imaging detectors should be reported.

Bibliography

[1] S. Andrews, D. A. Ellis, H. Shaw, and L. Piwek. Beyond self-report: Tools to compare estimated and real-world smartphone use. *PLoS ONE*, 10(10):1–9, 2015.

[2] P. R. Wallace. The band theory of graphite. *Phys. Rev.*, 71(9):622–634, 1947.

[3] K. S. Novoselov, A. K. Geim, S. V. Morozov, D. Jiang, Y. Zhang, S. V. Dubonos, I. V. Grigorieva, and A. A. Firsov. Electric field effect in atomically thin carbon films. *Science*, 306:666–669, 2004.

[4] http://apps.webofknowledge.com.

[5] R. R. Nair, P. Blake, A. N. Grigorenko, K. S. Novoselov, T. J. Booth, T. Stauber, N. M. R. Peres, and A. K. Geim. Fine structure constant defines visual transparency of graphene. *Science*, 320(5881):1308–1308, 2008.

[6] L. Banszerus, M. Schmitz, S. Engels, J. Dauber, M. Oellers, F. Haupt, K. Watanabe, T. Taniguchi, B. Beschoten, and C. Stampfer. Ultrahigh-mobility graphene devices from chemical vapor deposition on reusable copper. *Sci. Adv.*, 1(6):1–6, 2015.

[7] D. R. Cairns, R. P. Witte, D. K. Sparacin, S. M. Sachsman, D. C. Paine, G. P. Crawford, and R. R. Newton. Strain-dependent electrical resistance of tin-doped indium oxide on polymer substrates. *App. Phys. Lett.*, 76(11):1425–1427, 2000.

[8] C. Lee, X. Wei, J. W. Kysar, and J. Hone. Measurement of the elastic properties and intrinsic strength of monolayer graphene. *Science*, 321:385–388, 2008.

[9] Y.-J. Yu, Y. Zhao, S. Ryu, L. E. Brus, K. S. Kim, and P. Kim. Tuning the graphene work function by electric field effect. *Nano Lett.*, 9(10):3430–3434, 2009.

[10] Rickard Arvidsson, Duncan Kushnir, Sverker Molander, and Björn A. Sandén. Energy and resource use assessment of graphene as a substitute for indium tin oxide in transparent electrodes. *Journal of Cleaner Production*, 132:289–297, 2016.

[11] T.-H. Han, Y. Lee, M.-R. Choi, S. H. Woo, S.-H. Bae, B. H. Hong, J.-H. Ahn, and T.-W. Lee. Extremely efficient flexible organic light-emitting diodes with modified graphene anode. *Nat. Photon.*, 6:105–110, 2012.

[12] M. Park, C. Chang, X. Zhou, J. Kong, T. Palacios, and Gradecak. S. Flexible graphene electrode-based organic photovoltaics with record-hih efficiency. *Nano Lett.*, 14:5148–5154, 2014.

[13] S. Bae, H. K. Kim, Y. Lee, X. Xu, J.-S. Park, Y. Zheng, J. Balakrishnan, D. Im, T. Lei, Y. I. Song, Y. J. Kim, K. S. Kim, B. Özyilmaz, J.-H. Ahn, B. H. Hong, and S. Iijima. 30 inch roll-based production of high-quality graphene films for flexible transparent electrodes. *Nat. Nanotechnol.*, 5:574–578, 2010.

[14] M. Mazur, D. Kaczmarek, J. Domaradzki, D. Wojcieszak, S. Song, and F. Placido. Influence of thickness on transparency and sheet resistance of ito thin films. In *IEEE, 8th International Conference ADSAM*, 2010.

[15] J.-Y. Lee, S. T. Connor, Y. Cui, and P. Peumanns. Solution-processed metal nanowire mesh transparent electrodes. *Nano Lett.*, 8(2):689–692, 2008.

[16] Y.-Y. Choi, S. J. Kang, H.-K. Kim, W. M. Choi, and S.-I. Na. Multilayer graphene films as transparent electrodes for organic photovoltaic devices. *Sol. Energy Mater Sol. Cells*, 96:281–285, 2012.

[17] M. F. Craciun, T. H. Bointon, and S. Russo. Is graphene a good transparent electrode for photovoltaics and display applications? *IET Circuits, Devices & Systems*, 9(6):403–412, 2015.

[18] I. Khrapach, F. Withers, T. H. Bointon, D. K. Polyushkin, W. L. Barnes, S. Russo, and M. F. Craciun. Novel highly conductive and transparent graphene-based conductors. *Adv. Mater.*, 24(21):2844–9, 2012.

[19] W. Bao, J. Wan, X. Han, X. Cai, H. Zhu, D. Kim, D. Ma, Y. Xu, J. N. Munday, H. D. Drew, M. S. Fuhrer, and L. Hu. Approaching the limits of transparency and conductivity in graphitic materials through lithium intercalation. *Nat. Commun.*, 5:4224, 2014.

[20] D. J. Wehenkel, T. H. Bointon, T. Booth, P. Bøggild, M. F. Craciun, and S. Russo. Unforeseen high temperature and humidity stability of FeCl3 intercalated few layer graphene. *Sci. Rep.*, 5:7609, 2015.

[21] F. H. L. Koppens, T. Mueller, P. Avouris, A. C. Ferrari, M. S. Vitiello, and M. Polini. Photodetectors based on graphene, other two-dimensional materials and hybrid systems. *Nat. Nanotechnol.*, 9:780–793, 2014.

[22] J. C. W. Song, M. S. Rudner, C. M. Marcus, and L. S. Levitov. Hot carrier transport and photocurrent response in graphene. *Nano Lett.*, 11(11):4688–4692, 2011.

[23] N. M. Gabor, J. C. W. Song, Q. Ma, L. N. Nair, T. Taychatanapat, K. Watanabe, T. Taniguchi, L. S. Levitov, and P. Jarillo-Herrero. Hot carrier-assited intrinsic photoresponse in graphene. 333:648–652, 2011.

[24] J. C W Song, M. Y. Reizer, and L. S. Levitov. Disorder-assisted electron-phonon scattering and cooling pathways in graphene. *Phys. Rev. Lett.*, 109(10):1–5, 2012.

[25] M. W. Graham, S.-F. Shi, D. C. Ralph, J. Park, and P. L. McEuen. Photocurrent measurements of supercollision cooling in graphene. *Nat. Phys.*, 9(2):103–108, 2013.

[26] M. C. Lemme, F. H L Koppens, A. L. Falk, M. S. Rudner, H. Park, L. S. Levitov, and C. M. Marcus. Gate-activated photoresponse in a graphene p-n junction. *Nano Lett.*, 11(10):4134–4137, 2011.

[27] N. Liu, H. Tian, G. Schwartz, J. B. H. Tok, T. L. Ren, and Z. Bao. Large-area, transparent, and flexible infrared photodetector fabricated using p-n junctions formed by n-doping chemical vapor deposition grown graphene. *Nano Lett.*, 14(7):3702–3708, 2014.

[28] S. Wang, Y. Sekine, S. Suzuki, F. Maeda, and H. Hibino. Photocurrent generation of a single-gate graphene p-n junction fabricated by interfacial modification. *Nanotechnology*, 26(38):385203, 2015.

[29] G. Konstantatos, M. Badioli, L. Gaudreau, J. Osmond, M. Bernechea, F. P. G. de Arquer, F. Gatti, and F. H. L. Koppens. Hybrid graphene-quantum dot phototransistors with ultrahigh gain. *Nat. Nanotechnol.*, 7(6):363–368, 2012.

[30] S. Goossens, G. Navickaite, C. Monasterio, S. Gupta, J. J. Piqueras, R. Pérez., G. Burwell, I. Nikitsky, T. Lasanta, T. Galán, E. Puma, A. Centeno, A. Pesquera, A. Zurutuza, G. Konstantatos, and F. H. L. Koppens. Broadband image sensor array based on graphene-CMOS integration. *Nat. Photon.*, 11:366–371, 2017.

[31] E.-K. Jeon, C.-S. Yang, Y. Shen, T. Nakanishi, D.-S. Jeong, J.-J. Kim, K.-S. Ahn, K-J. Kong, and J.-O. Lee. Photoconductivity and enhanced memory effects in hybrid C60-graphene transistors. *Nanotechnology*, 23(45):455202, 2012.

[32] S. Jang, E. Hwang, Y. Lee, S. Lee, and J. H. Cho. Multifunctional graphene optoelectronic devices capable of detecting and storing photonic signals. *Nano Lett.*, 15(4):2542–2547, 2015.

[33] E. H. Huisman, A. G. Shulga, P. J. Zomer, N. Tombros, D. Bartesaghi, S. Z. Bisri, M. A. Loi, L. J. A. Koster, and B. J. van Wees. High gain hybrid graphene-organic semiconductor phototransistors. *ACS Appl. Mater. Interfaces*, 7(21):11083–11088, 2015.

[34] X. Liu, X. Luo, H. Nan, H. Guo, P. Wang, L. Zhang, M. Zhou, Z. Yang, Y. Shi, W. Hu, Z. Ni, T. Qiu, Z. Yu, J. B. Xu, and X. Wang. Epitaxial ultrathin organic crystals on graphene for high-efficiency phototransistors. *Adv. Mater.*, 28(26):5200–5205, 2016.

[35] Z. Sun, Z. Liu, J. Li, G.-A. Tai, S.-P. Lau, and F. Yan. Infrared photodetectors based on CVD-grown graphene and PbS quantum dots with ultrahigh responsivity. *Adv. Mater.*, 24(43):5878–5883, 2012.

[36] W. Guo, S. Xu, Z. Wu, N. Wang, M. M. T. Loy, and S. Du. Oxygen-assisted charge transfer between ZnO quantum dots and graphene. *Small*, 9(18):3031–3036, 2013.

[37] S.-H. Cheng, T.-M. Weng, M.-L. Lu, W.-C. Tan, J.-Y. Chen, and Y.-F. Chen. All carbon-based photodetectors: an eminent integration of graphite quantum dots and two dimensional graphene. *Sci. Rep.*, 3:2694, 2013.

[38] K. Roy, M. Padmanabhan, S. Goswami, T. P. Sai, G. Ramalingam, S. Raghavan, and A. Ghosh. Graphene-mos2 hybrid structures for multifunctional photoresponsive memory devices. *Nat. Nanotechnol.*, 8(11):826–830, 2013.

[39] X. Li, J. Wu, N. Mao, J. Zhang, Z. Lei, Z. Liu, and H. Xu. A self-powered graphene-MoS2 hybrid phototransistor with fast response rate and high on-off ratio. *Carbon*, 92:126–132, 2015.

[40] R. Lu, J. Liu, H. Luo, V. Chikan, and J. Z. Wu. Graphene / GaSe-nanosheet hybrid : towards high gain and fast photoresponse. *Sci. Rep.*, page 19161, 2016.

[41] K. Zheng, F. Meng, L. Jiang, Q. Yan, H. H. Hng, and X. Chen. Visible photoresponse of single-layer graphene decorated with TiO2 nanoparticles. *Small*, 9(12):2076–2080, 2013.

[42] Y. Lee, J. Kwon, E. Hwang, C.-H. Ra, W. J. Yoo, J.-H. Ahn, J. H. Park, and J. H. Cho. High-performance perovskite-graphene hybrid photodetector. *Adv. Mater.*, 27(1):41–46, 2015.

[43] S. Y. Chen, Y. Y. Lu, F. Y. Shih, P. H. Ho, Y. F. Chen, C. W. Chen, Y. T. Chen, and W. H. Wang. Biologically inspired graphene-chlorophyll phototransistors with high gain. *Carbon*, 63(1):23–29, 2013.

[44] X. Liu, E. K. Lee, and J. H. Oh. Graphene-ruthenium complex hybrid photodetectors with ultrahigh photoresponsivity. *Small*, 10(18):1–7, 2014.

[45] A. H. Castro Neto, N. M. R. Peres, K. S. Novoselov, A. K. Geim, and F. Guinea. The electronic properties of graphene. *Rev. Mod. Phys.*, 81:109–162, 2009.

[46] K. S. Novoselov, A. K. Geim, S. V. Morozov, D. Jiang, M. I. Katsnelson, I. V. Grigorieva, S. V. Dubonos, and A. A. Firsov. Two-dimensional gas of massless Dirac fermions in graphene. *Nature*, 438(7065):197–200, 2005.

[47] Z. H. Ni, H. M. Wang, J. Kasim, H. M. Fan, T. Yu, Y. H. Wu, Y. P. Feng, and Z. X. Shen. Graphene thickness determination using reflection and contrast spectroscopy. *Nano Lett.*, 7(9):2758–2763, 2007.

[48] M. I. Katsnelson. Zitterbewegung, chirality, and minimal conductivity in graphene. *Eur. Phys. J. B*, 51:157–160, 2006.

[49] N. W Ashcroft and N D. Mermin. *Solid State Physics*. Number ISBN 0-471-92805-4. Holt McDougal, 2nd edition, 1976.

[50] M. Fuhrer. Textbook physics from a cutting-edge material. *Physics*, 3:16–18, 2010.

[51] D. K. Efetov and P. Kim. Controlling electron-phonon interactions in graphene at ultrahigh carrier densities. *Phys. Rev. Lett.*, 105(25):2–5, 2010.

[52] J. K. Viljas and T. T. Heikkilä. Electron-phonon heat transfer in monolayer and bilayer graphene. *Phys. Rev. B*, 81(24):1–9, 2010.

[53] M. I. Katsnelson. Graphene: Carbon In Two Dimensions, 2007.

[54] R. C. Jones. A method of describing the detectivity of photoconductive cells. *Rev. Sci. Instrum.*, 24(11):1035–1040, 1953.

[55] A. A. Balandin. Low-frequency 1/f noise in graphene devices. *Nat. Nanotech.*, 8(8):549–55, 2013.

[56] S. R. Forrest, D. D. C. Bradley, and M. E. Thompson. Measuring the efficiency of organic light-emitting devices. *Adv. Mater.*, 15(13):1043–1048, 2003.

[57] J. H. Strait, H. Wang, S. Shivaraman, V. Shields, M. Spencer, and F. Rana. Very slow cooling dynamics of photoexcited carriers in graphene observed by optical-pump terahertz-probe spectroscopy. *Nano Lett.*, 11(11):4902–4906, 2011.

[58] K. J. Tielrooij, J. C W Song, S. A. Jensen, A. Centeno, A. Pesquera, A. Z. Elorza, M. Bonn, L. S. Levitov, and F. H L Koppens. Photoexcitation cascade and multiple hot carrier generation in graphene. *Nat. Phys.*, 9(4):248–252, 2013.

[59] E. H. Hwang and S. Das Sarma. Acoustic phonon scattering limited carrier mobility in two-dimensional extrinsic graphene. *Physical Review B - Condensed Matter and Materials Physics*, 77(11):1–6, 2008.

[60] J. C. W. Song, M. S. Rudner, C. M. Marcus, and L. S. Levitov. Hot carrier transport and photocurrent response in graphene. *Nano Lett.*, 11(11):4688–4692, 2011.

[61] D. Sun, G. Aivazian, A. M. Jones, J. S. Ross, W. Yao, D. Cobden, and X. Xu. Ultrafast hot-carrier-dominated photocurrent in graphene. *Nat. Nanotech.*, 7(2):114–8, 2012.

[62] T. Lohmann, K. Von Klitzing, and J. H. Smet. Four-terminal magneto-transport in graphene p-n junctions created by spatially selective doping. *Nano Lett.*, 9(5):1973–1979, 2009.

[63] D. B. Farmer, Y. M. Lin, A. Afzali-Ardakani, and P. Avouris. Behavior of a chemically doped graphene junction. *App. Phys. Lett.*, 94(21):21–24, 2009.

[64] B. H. Seo, J. Youn, and M. Shim. Direct laser writing of air-stable p-n junctions in graphene. *ACS Nano*, 8(9):8831–8836, 2014.

[65] V. Panchal, R. Pearce, R. Yakimova, A. Tzalenchuk, and O. Kazakova. Standardization of surface potential measurements of graphene domains. *Sci. Rep.*, 3:2597, 2013.

[66] C. Kittel. *Introduction to Solid State Physics*. Wiley, 8th edition, 2004.

[67] M. Cutler and N. F. Mott. Observation of anderson localization in an electron gas. *Phys. Rev.*, 181(3):1336–1340, 1969.

[68] E. H. Hwang, E. Rossi, and S. Das Sarma. Theory of thermopower in two-dimensional graphene. *Phys. Rev. B*, 80(23):1–5, 2009.

[69] M Buscema, J O Island, D J Groenendijk, S I Blanter, G A Steele, H S van der Zant, and A Castellanos-Gomez. Photocurrent generation with two-dimensional van der Waals semiconductors. *Chem. Soc. Rev.*, 44(11):3691–3718, 2015.

[70] R. Bistritzer and A. H. MacDonald. Electronic cooling in graphene. *Phys. Rev. Lett.*, 102(20):13–16, 2009.

[71] M. Freitag, T. Low, F. N. Xia, and P. Avouris. Photoconductivity of biased graphene. *Nat. Photon.*, 7(1):53–59, 2013.

[72] S. M. Sze and K. K. Ng. *Physics of Semiconductor Devices.* Wiley, 3rd edition, 2007.

[73] F. Xia, T. Mueller, Y.-M. Lin, A. Valdes-Garcia, and P. Avouris. Ultrafast graphene photodetector. *Nat. Nanotech.*, 4(12):839–43, 2009.

[74] X. Yu, V. Kalihari, C. D. Frisbie, N. K. Oh, and J. A. Rogers. Tetracene air-gap single-crystal field-effect transistors. *App. Phys. Lett.*, 90(16), 2007.

[75] D. A. da Silva Filho, E.-G. Kim, and J.-L. Brédas. Transport properties in the rubrene crystal: electronic coupling and vibrational reorganization energy. *Adv. Mater.*, 17(8):1072–1076, 2005.

[76] O. D. Jurchescu, A. Meetsma, and T. T. M. Palstra. Low-temperature structure of rubrene single crystals grown by vapor transport. *?Electrochem. Solid State Lett.*, 9(5):330–334, 2006.

[77] H. Najafov, B. Lee, Q. Zhou, L. C. Feldman, and V. Podzorov. Observation of long-range exciton diffusion in highly ordered organic semiconductors. *Nat. Mater.*, 9(11):938–943, 2010.

[78] H. Najafov, B. Lyu, I. Biaggio, and V. Podzorov. Two mechanisms of exciton dissociation in rubrene single crystals. *App. Phys. Lett.*, 96(18), 2010.

[79] M. Fox. *Optical Properties of Solids.* Oxford University Press, 2nd edition, 2002.

[80] A. I. M. Rae. *Quantum Mechanics.* Taylor & Francis, 5th edition, 2008.

[81] L. Gaudreau, K. J. Tielrooij, G. E. D. K. Prawiroatmodjo, J. Osmond, F. J. G. de Abajo, and F. H. L. Koppens. Universal distance-scaling of nonradiative energy transfer to graphene. *Nano. Lett.*, 13(5):2030–2035, 2013.

[82] G. L. Closs, M. D. Johnson, J. R. Miller, and P. Piotrowiak. A connection between intramolecular long-range electron, hole, and triplet energy transfers. *J. Am. Chem. Soc.*, 111(10):3751–3753, 1989.

[83] P. Irkhin, H. Najafov, and V. Podzorov. Steady-state photoconductivity and multi-particle interactions in high-mobility organic semiconductors. *Sci. Rep.*, pages 1–9, 2015.

[84] T. H. Bointon, M. D. Barnes, S. Russo, and M. F. Craciun. High quality monolayer graphene synthesized by resistive heating cold wall chemical vapor deposition. *Adv. Mater.*, 27(28):4200–4206, 2015.

[85] M. S. Dresselhaus and G. Dresselhaus. Intercalation compounds of graphite. *Adv. Phys.*, 30(2):139–326, 1981.

[86] D. Zhan, L. Sun, Z. H. Ni, L. Liu, X. F. Fan, Y. Wang, T. Yu, Y. M. Lam, W. Huang, and Z. X. Shen. FeCl3-based few-layer graphene intercalation compounds: single linear dispersion electronic band structure and strong charge transfer doping. *Adv. Funct. Mater.*, 20(20):3504–3509, 2010.

[87] R. A. Laudise, C. Kloc, P. G. Simpkins, and T. Siegrist. Physical vapor growth of organic semiconductors. *J. Cryst. Growth*, 187(3-4):449–454, 1998.

[88] X. Li, Y. Zhu, W. Cai, M. Borysiak, B. Han, D. Chen, R. D. Piner, L. Colomba, and R. S. Ruoff. Transfer of large-area graphene films for high-performance transparent conductive electrodes. *Nano Lett.*, 9(12):4359–4363, 2009.

[89] X. Liang, B. A. Sperling, I. Calizo, G. Cheng, C. A. Hacker, Q. Zhang, Y. Obeng, K. Yan, H. Peng, Q. Li, X. Zhu, H. Yuan, A. R. Hight Walker, Z. Liu, L. M. Peng, and C. A. Richter. Toward clean and crackless transfer of graphene. *ACS Nano*, 5(11):9144–9153, 2011.

[90] K. Nagashio, T. Yamashita, T. Nishimura, K. Kita, and A. Toriumi. Electrical transport properties of graphene on SiO2 with specific surface structures. *J. Appl. Phys.*, 110(2), 2011.

[91] J. R. Ferraro, K. Nakamoto, and C. W. Brown. *Introductory Raman Spectroscopy.* 2nd edition, 2003.

[92] Andrea C Ferrari and Denis M Basko. Raman spectroscopy as a versatile tool for studying the properties of graphene. *Nature nanotechnology*, 8:235–46, 2013.

[93] C. Neumann, S. Reichardt, P. Venezuela, M. Drögeler, L. Banszerus, M. Schmitz, K. Watanabe, T. Taniguchi, F. Mauri, B. Beschoten, S. V. Rotkin, and C. Stampfer. Raman spectroscopy as probe of nanometre-scale strain variations in graphene. *Nat. Commun.*, 6:8429, 2015.

[94] M. Lazzeri and F. Mauri. Nonadiabatic Kohn anomaly in a doped graphene monolayer. *Phys. Rev. Lett.*, 97(26):266407, 2006.

[95] A. Das, S. Pisana, B. Chakraborty, S. Piscanec, S. K. Saha, U. V. Waghmare, K. S. Novoselov, H. R. Krishnamurthy, A. K. Geim, A. C. Ferrari, and A. K. Sood. Monitoring dopants by Raman scattering in an electrochemically top-gated graphene transistor. *Nat. Nanotechnol.*, 3(4):210–215, 2008.

[96] L. G. Cançado, A. Jorio, E. H. M. Ferreira, F. Stavale, C. A. Achete, R. B. Capaz, M. V. O. Moutinho, A. Lombardo, T. S. Kulmala, and A. C. Ferrari. Quantifying defects in graphene via Raman spectroscopy at different excitation energies. *Nano Lett.*, 11(8):3190–3196, 2011.

[97] A. C. Ferrari, J. C. Meyer, V. Scardaci, C. Casiraghi, M. Lazzeri, F. Mauri, S. Piscanec, D. Jiang, K. S. Novoselov, S. Roth, and A. K. Geim. Raman spectrum of graphene and graphene layers. *Phys. Rev. Lett.*, 97(18):1–4, 2006.

[98] S. Pisana, M. Lazzeri, C. Casiraghi, K. S. Novoselov, A. K. Geim, A. C. Ferrari, and F. Mauri. Breakdown of the adiabatic Born-Oppenheimer approximation in graphene. *Nat. Mater.*, 6(3):198–201, 2007.

[99] W. J. Zhao, P. H. Tan, J. Liu, and A. C. Ferrari. Intercalation of few-layer graphite flakes with FeCl3: Raman determination of Fermi level, layer decoupling and stability. *J. Am. Chem. Soc.*, 133(15):1–5, 2010.

[100] J. M. Cowley and J. A. Ibers. The structures of some ferric chloride-graphite compounds. *Acta Crystallogr.*, 9:421–431, 1956.

[101] N. Espinosa, R. García-Valverde, A. Urbina, and F. C. Krebs. A life cycle analysis of polymer solar cell modules prepared using roll-to-roll methods under ambient conditions. *Sol. Energy Mater Sol. Cells*, 95(5):1293–1302, 2011.

[102] T. H. Bointon, G. F. Jones, A. De Sanctis, R. Hill-Pearce, M. F. Craciun, and S. Russo. Large-area functionalized CVD graphene for work function matched transparent electrodes. *Sci. Rep.*, 5:16464, 2015.

[103] C.-F. Chen, C.-H. Park, B. W. Boudouris, J. Horng, B. Geng, C. Girit, A. Zettl, M. F. Crommie, R. A. Segalman, S. G. Louie, and F. Wang. Controlling inelastic light scattering quantum pathways in graphene. *Nature*, 471(7340):617–620, 2011.

[104] E. Torres Alonso, G. Karkera, G. F. Jones, M. F. Craciun, and S. Russo. Homogeneously bright, flexible, and foldable lighting devices with functionalized graphene electrodes. *ACS Appl. Mater. Interfaces*, 8(26):16541–16545, 2016.

[105] C. Farrow. *Characterisation and optimisation of alternating current thin film electroluminescent displays*. PhD thesis, Nottingham Trent University, 2014.

[106] M. Bredol and H. S. Dieckhoff. Materials for powder-based AC-electroluminescence. *Materials*, 3(2):1353–1374, 2010.

[107] J. G. Hooley and M. Bartlett. The intercalation isotherm of ferric chloride vapor on graphite from 300 to $350^oC. Carbon, 5 : 417 - -422, 1967$.

[108] J. Meyer, P. R. Kidambi, B. C. Bayer, C. Weijtens, A. Kuhn, A. Centeno, A. Pesquera, A. Zurutuza, J. Robertson, and S. Hofmann. Metal oxide induced charge transfer doping and band alignment of graphene electrodes for efficient organic light emitting diodes. *Sci. Rep.*, 4(1):5380, 2015.

[109] X. Xu, N. M. Gabor, J. S. Alden, A. M. Van Der Zande, and P. L. McEuen. Photothermoelectric effect at a graphene interface junction. *Nano Lett.*, 10(2):562–566, 2010.

[110] J. Nelson. *The Physics of Solar Cells*. Imperial College Press, 1st edition, 2003.

[111] T. Mueller, F. Xia, and P. Avouris. Graphene photodetectors for high-speed optical communications. *Nat. Photon.*, 4(5):297–301, 2010.

[112] J. S. Bunch, S. S. Verbridge, J. S. Alden, A. M. V. Der, J. M. Parpia, H. G. Craighead, P. L. Mceuen, J. S. Bunch, S. S. Verbridge, J. S. Alden, A. M. V. D. Zande, J. M. Parpia, H. G. Craighead, and P. L. Mceuen. Impermeable atomic membranes from graphene sheets. *Nano Lett.*, 8(8):3–7, 2008.

[113] T. Mueller, F. Xia, M. Freitag, J. Tsang, and P. Avouris. Role of contacts in graphene transistors: a scanning photocurrent study. *Phys. Rev. B*, 79(24):1–6, 2009.

[114] K. J. Tielrooij, L. Piatkowski, M. Massicotte, A. Woessner, Q. Ma, Y. Lee, K. S. Myhro, C. N. Lau, P. Jarillo-Herrero, N. F. van Hulst, and F. H. L. Koppens. Generation of photovoltage in graphene on a femtosecond timescale through efficient carrier heating. *Nat. Nanotechnol.*, 10(5):437–443, 2015.

[115] V. Patil, A. Capone, S. Strauf, and E.-H. Yang. Improved photoresponse with enhanced photoelectric contribution in fully suspended graphene photodetectors. *Sci. Rep.*, 3:2791, 2013.

[116] C. O. Kim, S. Kim, D. H. Shin, S. S. Kang, J. M. Kim, C. W. Jang, S. S. Joo, J. S. Lee, J. H. Kim, S.-H. Choi, and E. Hwang. High photoresponsivity in an all-graphene p-n vertical junction photodetector. *Nat. Commun.*, 5:1–7, 2014.

[117] C.-H. Liu, Y.-C. Chang, T. B. Norris, and Z. Zhong. Graphene photodetectors with ultra-broadband and high responsivity at room temperature. *Nat. Nanotechnol.*, 9:273–278, 2014.

[118] X. Zou, D. Zhan, X. Fan, D. Lee, S. K. Nair, L. Sun, Z. Ni, Z. Luo, L. Liu, T. Yu, Z. Shen, and E. E. M. Chia. Ultrafast carrier dynamics in pristine and FeCl3-intercalated bilayer graphene. *App. Phys. Lett.*, 97(14):2014–2017, 2010.

[119] J. Huang, J. A. Alexander-Webber, T. J. B. M. Janssen, A. Tzalenchuk, T. Yager, S. Lara-Avila, S. Kubatkin, R. L. Myers-Ward, V. D. Wheeler, D. K. Gaskill, and R. J. Nicholas. Hot carrier relaxation of Dirac fermions in bilayer epitaxial graphene. *J. Phys. Condens. Matter*, 27(16):164202, 2015.

[120] A. V. Klekachev, M. Cantoro, M. H. van der Veen, A. L. Stesmans, M. M. Heyns, and S. De Gendt. Electron accumulation in graphene by interaction with optically excited quantum dots. *Physica E*, 43(5):1046–1049, 2011.

[121] J. D. Mehew, S. Unal, E. Torres Alonso, G. F. Jones, S. Fadhil Ramadhan, M. F. Craciun, and S. Russo. Fast and highly sensitive ionic-polymer-gated WS2-graphene photodetectors. *Adv. Mater.*, 29:1700222, 2017.

[122] M. Sim, J. Shin, C. Shim, M. Kim, S. B. Jo, J. H. Kim, and K. Cho. Dependence of exciton diffusion length on crystalline order in conjugated polymers. *J. Phys. Chem. C*, 118(2):760–766, 2014.

[123] W. L. Kalb, S. Haas, C. Krellner, T. Mathis, and B. Batlogg. Trap density of states in small-molecule organic semiconductors: A quantitative comparison of thin-film transistors with single crystals. *Phys. Rev. B*, 81(15):1–13, 2010.

[124] A. Pirkle, J. Chan, A. Venugopal, D. Hinojos, C. W. Magnuson, S. McDonnell, L. Colombo, E. M. Vogel, R. S. Ruoff, and R. M. Wallace. The effect of chemical residues on the physical and electrical properties of chemical vapor deposited graphene transferred to SiO2. *App. Phys. Lett.*, 99(12):3–5, 2011.

[125] P. H. Tan, W. P. Han, W. J. Zhao, Z. H. Wu, K. Chang, H. Wang, Y. F. Wang, N. Bonini, N. Marzari, N. Pugno, G. Savini, A. Lombardo, and A. C. Ferrari. The shear mode of multilayer graphene. *Nat. Mater.*, 11(4):294–300, 2012.

[126] D. Graf, F. Molitor, K. Ensslin, C. Stampfer, A. Jungen, C. Hierold, and L. Wirtz. Spatially resolved raman spectroscopy of single- and few-layer graphene. *Nano Lett.*, 7(2):238–242, 2007.

[127] D. M. Basko, S. Piscanec, and A. C. Ferrari. Electron-electron interactions and doping dependence of the two-phonon Raman intensity in graphene. *Phys. Rev. B*, 80(16):165413, 2009.

[128] Y. Hao, Y. Wang, L. Wang, Z. Ni, Z. Wang, R. Wang, C. K. Koo, Z. Shen, and J. T. L. Thong. Probing layer number and stacking order of few-layer graphene by Raman spectroscopy. *Small*, 6(2):195–200, 2010.

[129] J. Wilson and J. F. B. Hawkes. *Optoelectronics: An Introduction.* Prentice-Hall International Series in Optoelectronics, New York, 1st edition, 1983.

[130] J. Vrijmoeth, R. W. Stok, R. Veldman, W. A. Schoonveld, and T. M. Klapwijk. Single crystallites in "planar polycrystalline" oligothiophene films: determination of orientation and thickness by polarization microscopy. *J. Appl. Phys.*, 83(7):3816–3824, 1998.

[131] R. W. I. de Boer, M. E. Gerhenson, A. F. Morpurgo, and V. Podzorov. Organic single-crystal field-effect transistors. *Phys. Stat. Sol. (a)*, 10(6):1302–1331, 2007.

[132] V. C. Sundar, J. Zaumseil, V. Podzorov, E. Menard, R. L. Willett, T. Someya, M. E. Gershenson, and J. A. Rogers. Elastomeric transistor stamps: transport in organic crystals. *Science*, 303:1644–1646, 2004.

[133] V. Podzorov, S. E. Sysoev, E. Loginova, V. M. Pudalov, and M. E. Gershenson. Single-crystal organic field effect transistors with the hole mobility $\sim 8\mathrm{cm}^2/Vs. App. Phys. Lett., 83(17) : 3504 - -3506, 2003.$

[134] P. Irkhin, A. Ryasnyanskiy, M. Koehler, and I. Biaggio. Absorption and photoluminescence spectroscopy of rubrene singlecrystals. *Phys. Rev. B*, 86(8):085143, 2012.

[135] X. Song, L. Wang, Q. Fan, Y. Wu, H. Wang, C. Liu, N. Liu, J. Zhu, D. Qi, X. Gao, and A. T. S. Wee. Role of oxygen incorporation in electronic properties of rubrene films. *App. Phys. Lett.*, 97:032106, 2010.

[136] M. Fox. *Optical Properties of Solids.* Oxford University Press, Oxford, 2nd edition, 2010.

[137] N. Sai, M. L. Tiago, J. R. Chelikowsky, and F. A. Reboredo. Optical spectra and exchange-correlation effects in molecular crystals. *Phys. Rev. B*, 77:161306, 2008.

[138] J. R. Weinberg-Wolf, L. E. McNeil, S. Liu, and C. Kloc. Evidence of low intermolecular coupling in rubrene single crystals by Raman scattering. *J. Phys. Condens. Matter*, 19:276204, 2007.

[139] E. Venuti, I. Bilotti, R. Guido, D. Valle, A. Brillante, P. Ranzieri, M. Masino, and A. Girlando. Polarized Raman spectra of a rubrene single crystal. *J. Phys. Chem. C*, 112(44):17416–17422, 2008.

[140] A. Girlando, L. Grisanti, M. Masino, I. Bilotti, A. Brillante, R. G. Della Valle, and E. Venuti. Peierls and Holstein carrier-phonon coupling in crystalline rubrene. *Phys. Rev. B*, 82(035208), 2010.

[141] D. D. T. Mastrogiovanni, J. Mayer, A. S. Wan, A. Vishnyakov, A. V. Neimark, V. Podzorov, L. C. Feldman, and E. Garfunkel. Oxygen incorporation in rubrene single crystals. *Sci. Rep.*, 4:4753, 2014.

[142] R. S. Swathi and K. L. Sebastian. Long range resonance energy transfer from a dye molecule to graphene has (distance)$^{-4}$*dependence*. *J.Chem.Phys.*, 130 : 086101, 2009.

[143] C. Petit, D. Zander, K. Lmimouni, M. Ternisien, D. Tondelier, S. Lenfant, and D. Vuillaume. Gate pulse electrical method to characterize hysteresis phenomena in organic field effect transistor. *Organic Electronics*, 9(6):979–984, 2008.

[144] M. Egginger, S. Bauer, R. Schwödiauer, H. Neugebauer, and N. S. Sariciftci. Current versus gate voltage hysteresis in organic field effect transistors. *Monatshefte für Chemie*, 140(7):735–750, 2009.

[145] J. W. Weber, V. E. Calado, and M. C. M. Van De Sanden. Optical constants of graphene measured by spectroscopic ellipsometry. *App. Phys. Lett.*, 97(9), 2010.

[146] L. Gao, R. Lemarchand, and M. Lequime. Refractive index determination of SiO2 layer in the UV/Vis/NIR range: spectrophotometric reverse engineering on single and bi-layer designs. *J. Eur. Opt. Soc.*, 8:13010, 2013.

[147] M. A. Green and M. J Keevers. Optical properties of intrinsic silicon at 300K. *Prog. Photovoltaics Res. Appl.*, 3(3):189–192, 1995.

[148] Steven J. Byrnes. Multilayer optical calculations. *arXiv*, 1603.02720:1–20, 2016.

[149] B. Harbecke. Coherent and Incoherent Reflection and Transmission of Multilayer Structures. *Appl. Phys. B*, 39(3):165–170, 1986.

[150] S.M. Sze and K. K. Ng. Metal-Semiconductor Contacts. In *Physics of Semiconductor Devices*, chapter 3, pages 134–196. John Wiley & Sons, 3rd edition, 2006.

[151] C. Goldmann, C. Krellner, K. P. Pernstich, S. Haas, D. J. Gundlach, and B. Batlogg. Determination of the interface trap density of rubrene single-crystal field-effect transistors and comparison to the bulk trap density. *J. Appl. Phys.*, 99(3):034507, 2006.

[152] P. Irkhin and I. Biaggio. Direct imaging of anisotropic exciton diffusion and triplet diffusion length in rubrene single crystals. *Phys. Rev. Lett.*, 107(1):1–4, 2011.

[153] V. Kochat, C. S. Tiwary, T. Biswas, G. Ramalingam, K. Hsieh, K. Chattopadhyay, S. Raghavan, M. Jain, and A. Ghosh. Magnitude and origin of electrical noise at individual grain boundaries in graphene. *Nano Lett.*, 16(1):562–567, 2016.

[154] M. A. Stolyarov, G. Liu, S. L. Rumyantsev, M. Shur, and A. A. Balandin. Suppression of 1/f noise in near-ballistic hBN-graphene-hBN heterostructure field-effect transistors. *App. Phys. Lett.*, 107(2), 2015.

[155] G. Konstantatos, L. Levina, A. Fischer, and E. H. Sargent. Engineering the temporal response of photoconductive photodetectors via selective introduction of surface trap states. *Nano Lett.*, 8(5):1446–1450, 2008.

[156] D. Kufer, T. Lasanta, M. Bernechea, F. H. L. Koppens, and G. Konstantatos. Interface engineering in hybrid quantum dot-2D phototransistors. *ACS Photonics*, 3(7):1324–1330, 2016.

[157] O.S. Heavens. *Optical properties of thin solid films.* Dover Publications Inc, New York, 1st edition, 1991.

Appendices

A

Reflectance simulations of multilayer thin film substrates

The Fresnel equations for light at normal incidence ($\theta = 0°$) to a sharp material interface describe the reflectance ($R_{1,2}$) and transmittance ($T_{1,2}$) of light propagating from medium 1 into medium 2 as a function of the complex refractive index, $\tilde{n} = n_{Re} + i\kappa$ of each material.[157]

$$R_{1,2} = \left[\frac{\tilde{n}_1 - \tilde{n}_2}{\tilde{n}_1 + \tilde{n}_2}\right]^2 = |r_{1,2}|^2 \tag{A.1}$$

$$T_{1,2} = \frac{4\tilde{n}_1\tilde{n}_2}{\tilde{n}_1 + \tilde{n}_2} = \frac{\tilde{n}_2}{\tilde{n}_1}|t_{1,2}|^2 \tag{A.2}$$

Where $r_{1,2}/t_{1,2}$ are the ratios between the complex electric field amplitudes of reflected/-transmitted waves and that of the incident wave. If we consider light rays directed upon both sides of a sharp interface, the following relations can be deduced from conservation of energy:[148,149]

$$v_{n+1} = v_n e^{i\delta_n} t_{n,n+1} + w_{n+1} r_{n+1,n} \tag{A.3}$$

$$w_n e^{-i\delta_n} = w_{n+1} t_{n+1,n} + v_n e^{i\delta_n} r_{n,n+1} \tag{A.4}$$

where $\delta = k_n z_n$, z_n is the thickness of layer n and the wavevector of light propagating in medium n relates to the complex refractive index by $k_n = 2\pi\tilde{n}/\lambda_{vac}$. λ_{vac} is the light source wavelength in vacuum. The amplitude of forward rays are denoted as v, whereas the amplitude of backward propagating waves are denoted as w (see Figure A.1). From equations (A.1) and (A.2), $r_{n,n+1} = -r_{n+1,n}$ and $t_{n,n+1}/r_{n,n+1} = t_{n+1,n}/r_{n+1,n}$. Re-arranging equations (A.3) and (A.4), a matrix formalism can be constructed to express the amplitude of forward propagating (v_n)/backward propagating (w_n) rays immediately after/before crossing the interface between layers n and $n-1$ with respect to equivalent terms (v_{n+1} and w_{n+1}) concerning the neighbouring interface between layers n and $n+1$:

$$\begin{pmatrix} v_n \\ w_n \end{pmatrix} = M_n \begin{pmatrix} v_{n+1} \\ w_{n+1} \end{pmatrix} \tag{A.5}$$

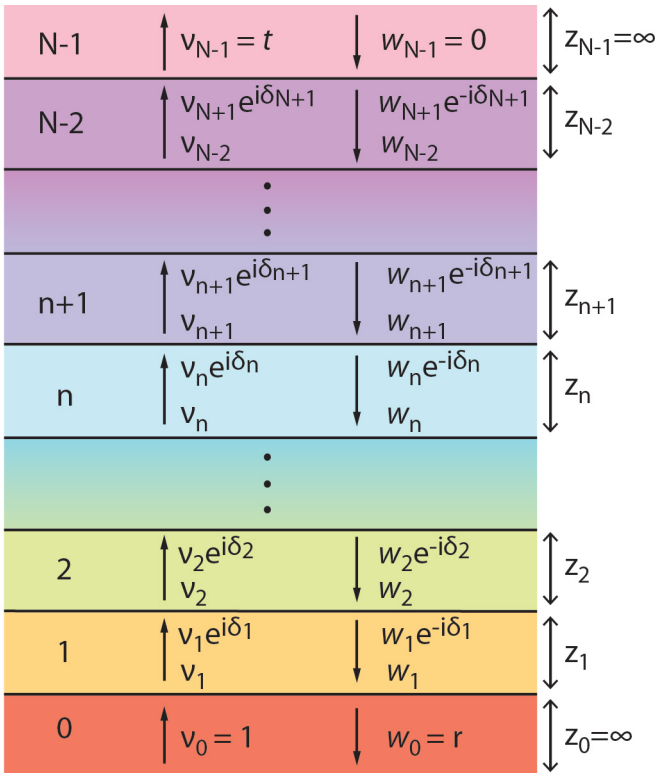

Figure A.1: [**Calculating multiple reflections from a thin-film stack**A diagram of the amplitude of forwards v and backwards w propagating light rays in a multi-layer thin film system consisting of $N-1$ layers.

where

$$M_n = \begin{pmatrix} e^{-i\delta_n} & 0 \\ 0 & e^{i\delta_n} \end{pmatrix} \begin{pmatrix} 1 & r_{n,n+1} \\ r_{n,n+1} & 1 \end{pmatrix} \frac{1}{t_{n,n+1}} \tag{A.6}$$

Hence, by applying Equation (A.5) to every interface in a multilayer stack of $N-2$ layers sandwiched between two semi-infinite media (see Figure A.1), relations describing the total reflected (r) and transmitted (t) fractions of the incident electric field amplitude.

$$\begin{pmatrix} v_0 \\ w_0 \end{pmatrix} = \begin{pmatrix} e^{-i\delta_0} & 0 \\ 0 & e^{i\delta_0} \end{pmatrix} \begin{pmatrix} 1 & r_{0,1} \\ r_{0,1} & 1 \end{pmatrix} \frac{1}{t_{0,1}} \prod_{n=1}^{N-2} M_n \begin{pmatrix} v_{N-1} \\ w_{N-1} \end{pmatrix} \tag{A.7}$$

$$\therefore \begin{pmatrix} 1 \\ r \end{pmatrix} = \tilde{M} \begin{pmatrix} t \\ 0 \end{pmatrix} \tag{A.8}$$

where

$$\tilde{M} = \begin{pmatrix} \tilde{M}_{00} & \tilde{M}_{01} \\ \tilde{M}_{10} & \tilde{M}_{11} \end{pmatrix} = \begin{pmatrix} 1 & r_{0,1} \\ r_{0,1} & 1 \end{pmatrix} \frac{1}{t_{0,1}} \prod_{n=1}^{N-2} M_n \tag{A.9}$$

Finally, the electric field amplitudes of light waves reflected from and transmitted through the multilayer thin film structure are found from Equations (A.8) and (A.9).

$$t = \frac{1}{\tilde{M}_{00}} \tag{A.10}$$

$$r = \frac{\tilde{M}_{00}}{\tilde{M}_{10}} \tag{A.11}$$

Using thin film analysis software (TFCalc, Software Spectra Inc) we used Equations (A.11) and (A.1) to simulate the reflectance of multilayer thin film stacks in the substrates of rubrene and rubrene-graphene transistors.

B

Supporting data for comparative plots of phototransitors

Chap 6 Ref [29]	**Photo-active material**	**Type of graphene**					
[Konstantatos et al, Nat. Nano, 7 (2012)]	Colloidal PbS QDs	Mechanically exfoliated monolayer flake					
Sample Name	**Responsivity (A/W)**	**Power (Wm-2)**	**Vs (V)**	**L (m)**	**Mobility (cm2V-1s-1)**	**Photon Energy (eV)**	$\eta_{PG7L}(s)$
Main text device	5.00E+07	8.00E-04	5	1.00E-05	1.00E+03	2.33053	2.33E-02
[info source]	Fig. 3c	Fig. 3c & Fig. 1b	Fig. 3 caption	main text, page 5	main text, page 5	Fig. 3 caption	
Chap 6 Ref [35]	**Photo-active material**	**Type of graphene**					
[Sun et. al, Adv. Mat. 24 (2012)]	PbS QDs	CVD-grown monolayer film					
Sample Name	**Responsivity (A/W)**	**Power (Wm-2)**	**Vs (V)**	**L (m)**	**Mobility ($cm^2V^{-1}s^{-1}$)**	**Photon Energy (eV)**	$\eta_{PG7L}(s)$
Main text device	1.00E+06	1.00E-04	0.5	1.00E-04	1.00E+03	1.3853	2.77E-01
[info source]	[Fig. 2c]	[Fig. 2c]	[Fig. 2c]	[methods]	main text, page 2	[Fig. 2 caption]	
Chap 6 Ref [36]	**Photo-active material**	**Type of graphene**					
[Guo et al, Small, 9 (2012)]	ZnO QDs	Mechanically exfoliated monolayer flake					
Sample Name	**Responsivity (A/W)**	**Power (Wm-2)**	**Vs (V)**	**L (m)**	**Mobility ($cm^2V^{-1}s^{-1}$)**	**Photon Energy (eV)**	$\eta_{PG7L}(s)$
Main text device	1.20E+04	1.00E-01	1.00E-03	1.00E-05	3.00E+03	3.8149	1.53E-02
[info source]	[Fig. 4]	[Fig. 4]	[main text, page 4]	[main text, page 4]	[main text, page 4]	[Fig. 2d & methods]	
Chap 6 Ref [37]	**Photo-active material**	**Type of graphene**					
[Cheng et. Al. Sci. Rep, 3 (2013)]	Graphite QDs	CVD-grown monolayer film					
Sample Name	**Responsivity(A/W)**	**Power (Wm-2)**	**Vs (V)**	**L (m)**	**Mobility ($cm^2V^{-1}s^{-1}$)**	**Photon Energy (eV)**	$\eta_{PG7L}(s)$
Main text device	1.60E+07	1.03E+04	1.00E+00	8.00E-06	1.20E+03	3.8149	3.26E-02
[info source]	[Fig. 3b]	[Fig. 3b], main text p4	[Fig. 3b]	[methods]	[main text, page 4]	[methods]	
Chap 6 Ref [38]	**Photo-active material**	**Type of graphene**					
[Roy et al, Nat. Nano, 8 (2013)]	Mechanically exfoliated 5 layer MoS2	Mechanically exfoliated monolayer flake					
Sample Name	**Responsivity(A/W)**	**Power (Wm-2)**	**Vs (V)**	**L (m)**	**Mobility ($cm^2V^{-1}s^{-1}$)**	**Photon Energy (eV)**	$\eta_{PG7L}(s)$
Main text device	5.00E+08	6.40E-03	0.1	1.15E-06	1.00E+04	1.95251	1.29E-02
[info source]	[Fig. 2c inset (T=300K)]	[main text, page 2]	[main text, page 2]	[gain calc in main text]	[main text, page 3]	[Fig. 2c caption]	
Chap 6 Ref [40]	**Photo-active material**	**Type of graphene**					
[Lu et al, Sci. Rep, 6 (2016)]	GaSe Nanosheets	CVD-grown monolayer film					
Sample Name	**Responsivity(A/W)**	**Power (Wm-2)**	**Vs (V)**	**L (m)**	**Mobility ($cm^2V^{-1}s^{-1}$)**	**Photon Energy (eV)**	$\eta_{PG7L}(s)$
Main text device	3.50E+05	5.70E-02	1.0	5.00E-06	3.20E+02	2.33	6.37E-04
[info source]	[Fig. 5b, main text p5]	[Fig. 5b, main text p5]	[Fig. 3b caption]	[methods]	[main text, page 4]	[methods]	
Chap 6 Ref [43]	**Photo-active material**	**Type of graphene**					
Chen et. al.,Carbon 63 (2013)	Chlorophyl-a	Mech. exf monolayer					
Sample Name	**Responsivity (A/W)**	**Power (Wm^{-2})**	**Vs (V)**	**L (m)**	**Mobility ($cm^2V^{-1}s^{-1}$)**	**Photon Energy (eV)**	$\eta_{PG7L}(s)$
Sample A	1.10E+06	4.40E-03	0.1	1.20E-05	1.58E+03	1.82E+00	1.82E-02
[Information source]	[Fig.3e]	[Fig. 3e]	[Supp. Info. S1]	[Supp. Info. S1]	[Supp. Info. Fig. S3]	[Fig. 2 caption]	
Sample C	1.30E+06	4.00E-03	0.1	1.20E-05	2.25E+03	1.82E+00	1.51E-02
[Information source]	[Fig. 4b]	[Fig. 4b]	[Supp. Info. S1]	[Supp. Info. S1]	[Supp. Info. Fig. S3]	[Fig. 2 caption]	
Sample D	1.00E+03	0.2	0.1	1.20E-05	2.30E+03	1.82E+00	1.14E-05
[Information source]	Fig. 4b]	[Fig. 4b]	[Supp. Info. S1]	[Supp. Info. S1]	[Supp. Info. Fig. S3]	[Fig. 2 caption]	
Chap 6 Ref [44]	**Photo-active material**	**Type of graphene**					
[Lui et. al. Small 18 (2014)]	Ruthenium Organo-mettalic Complex	CVD-grown monolayer film					
Sample Name	**Responsivity (A/W)**	**Power (Wm^{-2})**	**Vs (V)**	**L (m)**	**Mobility ($cm^2V^{-1}s^{-1}$)**	**Photon Energy (eV)**	$\eta_{PG7L}(s)$
Main text device	1.00E+05	3.00E+00	1	2.50E-05	3.20E+03	2.76E+00	5.38E-04
[info source]	[Fig. 4b]	[Fig. 4b]	[Fig. 4 caption]	[Main text, page 4]	[Main text, p4]	[Fig. 4 caption]	
Chap 6 Ref [33]	**Photo-active material**	**Type of graphene**					
Huisman et. al. ACS App. Mat. & Int, 7 (2015)	Amorphous P3HT	Monolayer CVD films (I & II) & mech. Exf. flakes on hBN (BN12 & BN23)					
Sample Name	**Responsivity (A/W)**	**Power (Wm^{-2})**	**Vs (V)**	**L (m)**	**Mobility ($cm^2V^{-1}s^{-1}$)**	**PhotonEnergy (eV)**	$\eta_{PG7L}(s)$
Device I	1.10E-01	9.70E+00	0.2	1.00E-03	1.54E+03	2.47968	8.86E-06
[info source]	[Table 1]	[Table 1]	[Table 1]	[Table 1]	[Table 1]	[Table 1]	
Device II	0.16	9.70E+00	0.2	1.00E-03	1.59E+03	2.47968	1.25E-05
[info source]	[Table 1]	[Table 1]	[Table 1]	[Table 1]	[Table 1]	[Table 1]	
BN12	8.40E+04	9.7	0.2	3.09E-06	2.56E+04	2.47968	3.88E-06
[info source]	[Table 2]	[Table 2]	[Table 2]	[Table 2]	[Table 2]	[Table 2]	
BN23	1.74E+05	9.7	0.2	1.46E-06	1.65E+04	2.47968	2.79E-06
[info source]	[Table 2]	[Table 2]	[Table 2]	[Table 2]	[Table 2]	[Table 2]	
Chap 6 Ref [34]	**Photo-active material**	**Type of graphene**					
Lui et. al. Adv. Mater. 28 (2015)	Epiataxially grown C8-BTBT	Mechanically exfoliated monolayer flake					
Sample Name	**Responsivity (A/W)**	**Power (Wm^{-2})**	**Vs (V)**	**L (m)**	**Mobility ($cm^2V^{-1}s^{-1}$)**	**PhotonEnergy (eV)**	$\eta_{PG7L}(s)$
1.04 Layers	4.43E+03	1.5069	0.1	7.2E-06	5.00E+03	3.49	1.60E-05
[info source]	[Table 1]	[Table 1]	[Table 1]	[Table 1]	[Table 1]	[Table 1]	
2.8 Layers	4.35E+04	3.48E-01	0.1	7.20E-06	5.00E+03	3.49	1.57E-04
[info source]	[Table 1]	[Table 1]	[Table 1]	[Table 1]	[Table 1]	[Table 1]	
4.5 Layers	1.65E+05	1.07E-01	0.1	7.20E-06	5.00E+03	3.49	5.98E-04
[info source]	[Table 2]	[Table 2]	[Table 2]	[Table 2]	[Table 2]	[Table 2]	

Table B.1: Compiled data from a comparative study of graphene phototransistors. This data was compiled in order to compare the specific EQE of each device in chapter 6. To the best of our knowledge, we have included every scientific report which clearly specifies all parameters required to calculate η^*_{EQE}.